Development of Mathematical Models of a Human Virtual Ear

Thesis
Ph.D Course on:
Mechanical Engineering
Cycle XXIV(X) (2009)

Tutors:
Prof. Costantino Carmignani
Prof. Paola Forte
Eng. Francesca Di Puccio
Student:
Gaia Volandri

UNIVERSITÀ DI PISA

University of Pisa
Department of Mechanical, Nuclear and Production Engineering
SSD ING-IND/13

Acknowledgments

I am thankful to my supervisors, Prof. Costantino Carmignani, Prof. Paola Forte and Eng. Francesca Di Puccio whose encouragement, guidance, participation and support enabled me to develop this thesis.

I am grateful to Prof. Berrettini and Dr. Bruschini of the U.O. Otorinolaringoiatria 2° of the S. Chiara/Cisanello hospital in Pisa, Prof. Carlo Bartoli, Prof. Luigi Lazzeri, Eng. Armando Razionale, Eng. Luca Nardini, Stefania Manetti and Thomas Wright. The engineers and technicians of MAGNA Closures S.p.A., Eng. Isidoro Mazzitelli and AM Testing s.r.l are gratefully acknowledged for their collaboration.

I would like to show my gratitude to all of those who supported me during the completion of the thesis.

Contents

Introduction

The human ear is a complex biomechanical system, devoted to sound reception and perception. However, some of the hearing function is accomplished by the central nervous system.

Sound consists in a traveling wave propagating in a medium as a mechanical wave of compression and rarefaction. Focusing on the air medium, mammals developed a tuned system to catch (outer ear) and transfer (middle ear) sound waves to the inner part of the ear, where the received input is converted to electric signals and sent to the auditory cortex. The outer ear consists of the auricle and the auditory canal. The middle ear mainly consists in the tympanic membrane and ossicular chain. The inner ear includes the cochlea. The present thesis mainly focuses on the outer and middle ear.

Since the peripheral parts of the ear consists in a mechanical system, distributed and lumped parameter models are proposed in the literature for simulating and predicting their behavior. During the PhD course, outer and middle ear models were developed as first stages to build a ”virtual” ear, with the aim of understanding and predicting the human perception of sound. The anatomy in brief and a model-oriented review of outer and middle ear are introduced in §1 and §2. In details, a finite element (FE) model of the tympanic membrane is presented in §4. A model including the auditory canal and the tympanic membrane was developed applying standard and generalized FE methods (§3). The multi-body (MB) approach was adopted for the ossicular chain and supporting structures (joints, ligaments and muscle tendons), as described in §5. The tympanic membrane FE model and the ossicular chain MB model were combined in a hybrid FE-MB model of the middle ear (§6).

The information processing in the auditory system, in terms of preprocessing in the peripheral system (outer, middle and inner ear) and neural processing, both including non-linearities, is a central issue of the psychoacoustics, a branch of acoustics concerning the quantitative correlation between the physical characteristics of sounds and their perceptual attributes. Psychoacoustic models consider the hearing function as a whole. The relationship between physical magnitudes of the stimulus and magnitudes of the correlated hearing sensations can be given either by equations or curves of a psychoacoustic model, based on experimental evidences or jury tests of perception.

As an application of the psychoacoustic approach, an experimental and theoretical activity on power window noise was conducted (§7) during the last year of the PhD course within a project in collaboration with MAGNA Closures S.p.A.

Chapter 1

Anatomy of the human ear

Sound consists in a traveling wave (transmitted through a solid, liquid, or gas) which could be easily described by means of the time-varying sound pressure [1].

The human auditory system responds in the 20 Hz−20 kHz frequency range (conventionally assumed audible frequencies [2]) and in the 10^{-5} (threshold in quiet)−10^{2} Pa (threshold of pain) values of sound pressure, identifying also pitch, timbre, and direction of a sound [1].

Focusing on the air medium (343 m/s speed of sound at 20°C and 1 atm), mammals developed a tuned system to catch (pinna/auricle) and transfer sound waves to the proper auditory organ (cochlea), where the received input is sent to the auditory cortex, passing through the acoustic ways.

Three parts are conventionally identified in the terrestrial mammalian ear: outer, middle, and inner ear (Fig. 1.1a).

The first portion conveys sound waves towards the eardrum (or

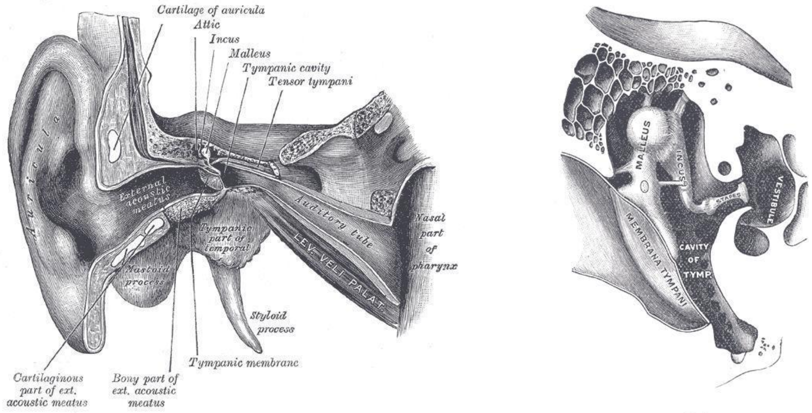

a) b)

Figure 1.1: A schematic representation of human a) outer and middle ear, b) middle and inner ear (Gray's anatomy table [3]).

tympanic membrane, TM), amplifying sound pressure in the frequency range 20 Hz - 20 kHz. The middle ear transfers the vibrations from the TM to the cochlea in the inner ear, a spiral-shaped organ responsible for the transduction of acoustic signals into neurological signals [4, 5]. Each part of the auditory apparatus has a very peculiar behavior, involving mainly fluid-structure interaction, mechanical vibrations, neurosignal generation and transmission. Some features of this complex biomechanical system have still to be completely understood and are investigated by experimental and numerical simulation. However both approaches share difficulties mainly due to the reduced size of the elements and the differences between animal and human apparatus that make extrapolation of results unfeasible.

The present thesis mainly focuses on the outer and middle ear.

The investigation of inner ear currently constitutes a future development of our study.

1.1 Outer ear

The outer ear consists of the auricle and the auditory canal (AC). The auricle picks up airborne vibratory waves. The AC channels them to the middle ear. It is closed at the medial end by the TM, which can be considered either part of the outer or the middle ear. Its "S-shaped" morphology, facilitates the sound wave channeling and amplifies some resonance frequencies.

1.2 Middle ear

The middle ear is an 1-2 cm^3 air-filled space in the temporal bone, which is normally sealed laterally by the TM or eardrum, including three small bones (the ossicles: malleus, incus and stapes), which constitute the ossicular chain (OC) and related structures, ligaments, muscles, joints and nerves, involved in sound conduction[3, 6], Fig. 1.2.

The OC builds a mechanical lever-action connection between the air-actuated TM and the fluid-filled cochlea. As the direct contact between air and cochlear fluids of the inner ear would not succeed in stimulating the perilymph of the inner ear to any significant extent, the middle ear primary function is to act as an impedance matching system between the low/high impedance media, air and cochlear fluids respectively. This function is achieved in two ways: the lever

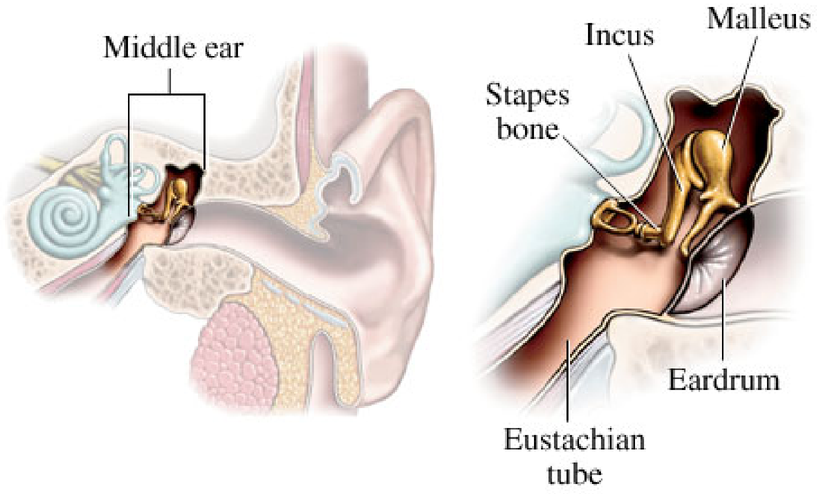

Figure 1.2: Middle ear schemes. (Reprinted with permission from `http://hearingaidscentral.com/howtheearworks.asp`)

action of the OC, reducing the displacement at the oval window (OW), with respect to the one at the apex of the TM (*umbo*, of about 1:1.3 - 1:3.1, and the ratio of the areas of the TM and the stapes footplate (SFP) which is about 27 [4].

1.2.1 Tympanic membrane

In the literature detailed descriptions of the human and animal TM from different laboratories and investigators are available; the great variations of the TM among different species elucidate the structure-function relationship of the morphological and physical features of the TM, which are differently tuned for the sound transmission in varying frequency ranges and environments for different species, e.g. [7, 8, 9].

The TM is placed in the ear canal with a particular orientation, which allows it to have a larger surface than the ear canal section itself. A typical angle between the human TM and the superior and posterior wall of the ear canal is 140 deg, while between the TM and the inferior and anterior wall is 30 deg [10].

The periphery of the TM is firmly anchored to the wall of the tympanic cavity, around most of its circumference, by a fibro - cartilaginous ring called the annular ligament (AL) or tympanic annulus (TA)[11] (Fig. 1.3a-b). This ligament is a fibrous thickening firmly attached to a sulcus in the bony tympanic ring, except superiorly where it separates the two main regions (or submembranes [12]) of the TM called the "pars tensa" (PT) and the "pars flaccida" (PF). The PT is a multi-laminar membrane which covers almost the whole extension of the TM with an outline varying from approximately circular to a more or less elongated ellipse across species. The PF lies in the superior region and its size is variable in mammals; the human PF is moderately small and it differs in anatomy and function from the PT since it is thicker and much more compliant than the rest of the membrane [9]. In the superior part of the tympanic ring, a deficiency in the temporal bone sulcus, called the *notch of Rivinus*, forms an attachment for the PF.

The TM is attached to the manubrium of the malleus, which stretches from a point on the superior edge of the TM to its center, the umbo (Fig. 1.3a-b). The umbo is considered a fundamental reference point, frequently mentioned in model result presentation. The manubrium of the malleus may be placed symmetrically, or closer to the antero-superior edge of the TM. The attachment of the manubrium to the TM varies along its length: the lateral process of the malleus and the umbo are firmly attached, while in the midway region, between the lateral process and the umbo, the manubrium separates slightly from the TM [10].

The TM (Fig. 1.3a-b) is almost oval in shape and conical in cross section, with the apex pointing medially towards the middle ear. Its vertical axis ranges from 8.5 to 10 mm while the horizontal axis ranges from 8 to 9 mm with a mean total area of 85 mm^2 [10]. In physiological conditions, its curved conical shape has a cone angle of 132−137 deg [13] with a cone depth included in the range 1.42 – 2 mm [14, 15].

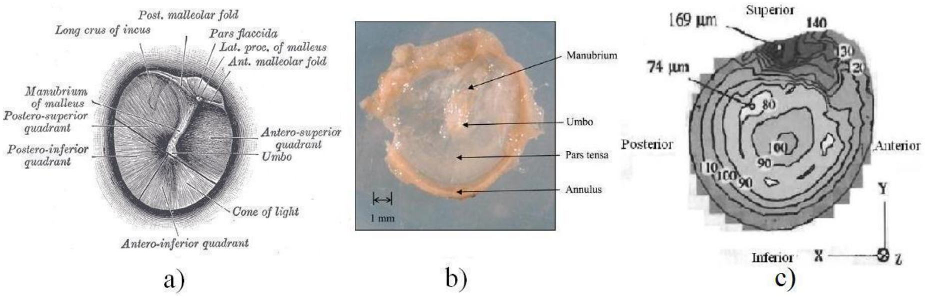

Figure 1.3: a) A schematic representation (Gray's anatomy table [3]), b) a medial view of the TM (reprinted from [13] with permission from Elsevier). c) Contour plot of the thickness distribution of an entire human TM (reprinted from [16] with permission from Elsevier).

A critical feature for vibratory behavior is the TM thickness as it describes the mass distribution in the rapidly vibrating TM and also influences the effective TM stiffness. An example of thickness distribution map is shown in Fig. 1.3c. At present, accurate and detailed data available concerning the thickness of the human TM are still few [17]. The first measurements are due to [18], who observed a non-uniform thickness ranging from 30 to 120 μm. Lately, until the 90's other thickness measurements on human TM were performed [19, 20, 21, 22, 23, 24], typically based on conventional light or electron microscopy on a few points of histological sections of non-fresh material. However, these data show large differences, probably due to pre-treatment effects in the sample preparation. Only recently a new method to draw a thickness distribution map of an untreated TM, based on confocal laser microscopy, was introduced for the cat in [17]. This method was applied in [25] to three fresh human samples obtaining a great inter-individual variability in mean thickness values (40, 50 and 120 μm), thus stressing that there is no typical human TM thickness. However the authors identified similar features in terms of relative thickness variations in all samples: a large thin portion in the infero-posterior quadrant, with a gradual thickening towards the superior portion, and an anterior part thicker than the posterior one.

In the through-thickness section of the TM, a multi-layer fiber structure consisting of distinct layers, varying in density, thickness, composition and arrangement in different regions, can be identified. In details, the TM is a tri-laminar membrane (Fig. 1.4a) with an inner mucosal epithelial layer (on the medial side), an outer epidermal layer (on the lateral side) and an intermediate fibrous layer (middle connective lamina propria) [26, 9]. The thin epidermal layer is continuous with the epidermis of the external canal and it is a typical keratinizing epithelium composed of four strata, made of different

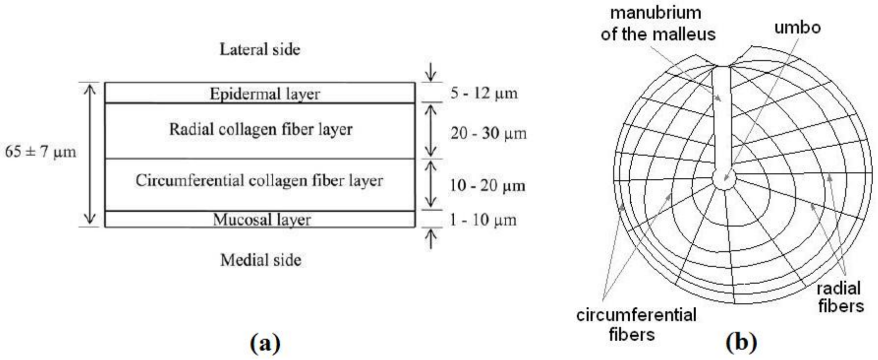

Figure 1.4: a) A schematic diagram of a typical TM cross-section through PT showing the arrangement and thickness of different layers (reprinted from [13] with permission from Elsevier). b) Schematic of the fiber orientation of human TM.

cell types [7]. The mucosal layer is a very thin layer of cells. The differences in the PT and PF lie in the structure of their lamina propria [10], whose cell and biological molecular aspects, vascular and nerve supply are deeply described in [7]. The lamina propria of the PT consists of two subepidermal connective tissue layers, between which there are two collagenous layers with radial and circular fiber orientation (Fig. 1.4b). The radial fibers become more packed as they converge on the manubrium, while the circular fiber layer grows thicker towards the periphery. These collagen fibers exhibit a viscoelastic and orthotropic behavior with membrane (or in-plane) properties different from through-thickness (or out-of-plane) properties [13]. Parabolic and transversal fibers have been identified in the PT, too. The parabolic fibers arise from near the lateral process of the malleus and extend downwards in a parabolic course to the anterior or posterior quadrant. The transversal fibers are short fibers running horizontally in the inferior quadrant. The lamina propria of the PF is made up with loose connective tissue containing collagen and elastic fibers [10].

In Fig. 1.4a ranges of thicknesses values for the entire membrane as well as for the layers in the PT portion are shown. It is worth noting that the overall membrane thickness is non-uniform but tapered from the periphery to the umbo; fiber layers follow the same trend but, whereas the circumferential fiber layer is tapered to nearly-zero thickness at the umbo, the radial fiber layer thickness decreases slightly.

As described in [8], the fibers of the human TM extend in a continuous manner towards the periphery forming the AL.

Experimental activity from the literature

Many experimental data on the mechanical characterization and vibration response of the TM can be found in the literature since the 40's, e.g. [27, 28, 19]. The availability of these data is crucial for model parameter identification and result validation. However it is worth noting that the complex structure and the small dimensions of the TM (around 10 mm in diameter and 0.08 mm in thickness) hinder the assessment of its mechanical and material properties as well as its constraints, morphological characteristics, static displacement under load and sound-induced motion. Despite the fact that mammalian TM's differ in some morphologic and material properties, animal TM have been widely investigated with the aim of generalizing the analysis results to the human case. In particular the most common animals in hearing research are gerbils and cats, although also rabbits, guinea pigs and mouses are commonly investigated [9].

In this paragraph a brief outline of published experimental results is reported. Further details on experimental data can be found in [8, 9].

Material characterization

Material characterization of the TM tissues still represents a debated issue, due to the variety of tests, typically *in vitro*, but also *in vivo*. Mechanical properties of the human TM were first measured by [27, 28] since the 40's and by [19]. They obtained very different Young's moduli (20 vs. 40 MPa) because values are strongly dependent on the precision of thickness measurements which are very critical. [29] conducted uniaxial tension tests of human TM samples obtaining a nonlinear stress-strain curve with a tangent modulus similar to v. Békésy at about ±8% of strain. Their results were re-interpreted by [30]. Other uniaxial tensile, stress relaxation, and failure tests on fresh human cadaver TM specimens were published only recently by [26] obtaining a Young's modulus varying from 0.4 to 22 MPa over the stress range from 0 to 1 MPa, in good agreement with [29]. All previously mentioned works employed rectangular strip samples from human TM deducing elasticity parameters under the hypotheses of isotropy, homogeneity and uniform thickness, although extracted taking into account the circumferential and radial directions. An example of a typical strip sample is indicated in Fig. 1.5 on an image from [13].

To the best of the authors' knowledge, the only works performing orthotropic characterization by means of tensile tests are [31, 32] that propose high strain rates tests obtaining Young's moduli of approximately 45, 51 and 59 MPa in the radial and 34, 41 and 57 MPa in the circumferential directions at three frequencies levels of about 320, 750 and 1500 s^{-1}.

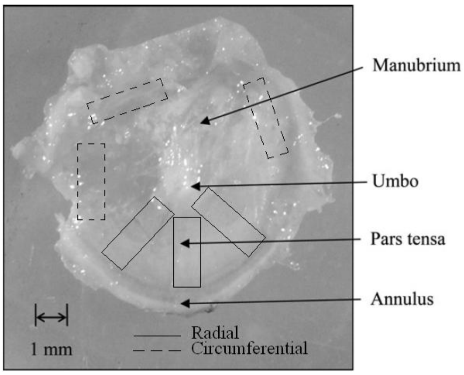

Figure 1.5: Schematic of the TM strip specimens cut from TM samples in the radial and circumferential directions (reprinted and modified from [13] with permission from Elsevier.)

For biomedical specimens, however, it is not always possible to obtain strips of uniform and manageable geometry and well-defined size suitable to be used in a pulling apparatus for tensile tests. Moreover for orthotropic characterization nine independent tests are required which can hardly be performed.

Point indentation techniques allow to leave the TM in its natural support, measuring the point displacement, the reaction force on the indentation needle and the deformation of the TM over a large area; elasticity parameters can be calculated from this measurements in a backward engineering process [33]. A Moiré interferometric technique in combination with point micro-indentation were used in [33, 34]. A few years after [26], the same research group

[35, 13] characterized the viscoelastic behavior of the TM by nanoindentations, measuring in-plane (clamping the sample on a circular hole) and through-thickness (placing the sample on a relatively rigid solid substrate) Young's relaxation moduli; [35] obtained steady-state values for the in-plane moduli of 17.4 MPa and 19 MPa for posterior and anterior TM samples, respectively (comparable with those obtained by [28]) and a value of through-thickness modulus of 6 MPa. In [13] nanoindentation was applied to sections cut from fresh-frozen human cadaveric TMs obtaining Young's relaxation modulus values ranging in approximately 25.7-37.8 MPa, close to values obtained by [19] and [28]. On the contrary, in [36] the nanoindentation technique is applied to the intact TM (i.e. without sectioning) and, using a 12 μm thickness, an effective $\sim$ 21 MPa average Young's modulus of the PT was found, with the assumptions of isotropy and homogeneity.

In [13, 37, 36, 34, 12] an inverse problem solving methodology was employed using the FE method to determine material parameters; in this approach material models are assumed in advance (e.g. linear elastic isotropic/orthotropic or hyperelastic material) and material parameters determined by inverse/optimisation procedures. In particular, the recent work of [12] presents an elastic characterization of the gerbil PF via inverse analysis of in situ static pressure inflation experiments assuming the Veronda-Westmann hyperelastic model.

The elasticity of human TM has been experimentally investigated *in vitro* by many authors. However, methods for in vivo clinical experiments investigating these elastic properties are relatively few and not readily comparable. Different measurements of elasticity have been reported by [38] who investigated the pressure-volume relationship of the middle ear system applying pressure changes in the ear canal; however, no single measure of elasticity was extracted from their experiments. Based on [38], a more recent pressure-volume method has been developed and improved by [39]. As a noteworthy example of a recent *in vivo* material characterization, [40] should be mentioned; in this study the areal modulus (i.e. the relationship between membrane tension and change of the surface area relative to the undeformed surface area, measured by means of an hydraulic system including pumps and tubes) is estimated in a group of 20 normal subjects, based on response of the human TM to quasi-static pressure changes; the Young’s modulus values, calculated dividing the areal moduli (derived from linear conditions) by the membrane thickness, result a factor 2-3 smaller than previously found *in vitro* by [27, 29].

For completeness, it is worth noting that the presence of prestrain might have an influence on the mechanical behavior of the TM as described by [28, 19].

Vibration response and displacement measurements

Several experimental investigations focus on measuring of TM static displacement and sound-induced vibrations with various (mostly interferometric) techniques. Tympanometry is a clinical *in vivo* measure of the average motion of the entire TM and does not distinguish the motion of different locations, although useful for aiding in the differential diagnosis of hearing diseases.

By contrast, interferometric techniques and, in particular, a commercially available laser Doppler vibrometer (LDV) (or interferometer, or velocimeter) is a non-contacting device capable of measuring the displacement amplitude of TM vibrations down to 1 nm.

Sound-induced motion of the umbo has often been studied through measurements of umbo displacement by LDV in the “piston-like” direction. LDV techniques are employed in recent literature *in vivo* [41, 42, 43, 44, 45] and *in vitro* [46, 47, 48, 49, 50]. The umbo velocity transfer function (magnitude and phase angle) is the most common output [41, 42, 43, 46, 47]; [41] estimated, by means of LDV measurements in 80 normal hearing ears of 56 subjects, a magnitude ranging over a little more than a factor of 10 (±10 dB) and a range of angles varying from about 45 deg at 250 Hz to more than 400 deg at the highest frequencies. The authors also describe a complex behavior similar to previously published measurements of umbo velocity in live ears: at frequencies below 0.7 kHz, the umbo velocity transfer function has a magnitude proportional to frequency and an angle between 45 and 90 deg; in the 1-2 kHz range, the transfer functions have a nearly constant magnitude and an angle near 0 deg; above 3 kHz, the increase in magnitude and the increasing phase lag between velocity and pressure suggest a complex relationship between the ear canal sound pressure and the velocity measured near the umbo. In [43] the LDV determined umbo-velocity transfer functions of ears with sensorineural hearing loss are compared with the same measurements on 56 ears from 56 normal-hearing subjects taken from [41]; their results show a wide range of variability with a magnitude range at any one frequency of a little larger than an order of magnitude (20 dB), and an angle range that increases with stimulus frequency, from ±10 deg at 0.3 kHz to ±180 deg at 6 kHz.

Although the umbo motion is a crucial input to the ossicular sound-conduction system, it is worth noting that vibrations of the entire TM surface contribute to vibration of the manubrium and ossicular sound conduction. For these reasons most detailed descriptions of the motion of the mammalian TM were obtained by means of time-averaged holograms [51, 52, 53, 54]. Time-averaged holography and holographic interferometry enable to record the complete vibration pattern of a surface within several seconds [55, 51, 52, 56].

Only few authors report the mode shapes (e.g. [16, 10]); [10], on the basis of a scanning LDV (SLDV), concludes that at low frequencies the TM assumes simple mode shapes without nodes, showing a piston-like movement of the umbo, while at higher frequencies the deformation pattern becomes more and more complex showing lots of peaks and valleys above 4 kHz; due to this highly fragmented movement pattern the movement of the umbo results drastically reduced.

Over the last years several research groups [57, 58] have worked to apply modern computer-assisted high-speed opto-electronic holography (OEH) to the study of the vibration of the TM, very suitable for *in vivo* investigations. In [58] OEH is employed to produce time-averaged holograms that describe the magnitude of the sound-induced motion of the surface of the TM. After using time-averaged holography, that is insensitive to the phase of motion relative to the sound stimulus phase, the same authors in [59] describe results using stroboscopic holography [57, 60, 61] to study sound-induced motion of the TM. With stroboscopic holography both the amplitude and phase of the dynamic deformations of the TM over the full field of view can be quantified.

Although the frequency response function varies across the TM surface, a reference point is commonly selected (usually the umbo or a point lying midway between the tip of the malleus and the annulus)

[62]. In [63] the TM displacement distribution, the maximum value, and the displacement value at the umbo are reported: ranging from 0.2 to 0.4 μm and equal to about 0.050 μm at approximately 120 dB and 80 dB, respectively. Most authors [15, 62, 64, 10, 65, 66, 67] report experimental and model-derived frequency response curves (umbo displacement or velocity vs. frequency, sometimes normalized by the input sound pressure value) as a crucial output of analysis. Concerning undamped modal frequencies, several authors observe a first resonance frequency in the umbo displacement frequency response typically ranging from 0.9 kHz to 1.4 kHz [10, 15, 16] or at about 1.5 kHz [62] in experimental (but also in numerical) investigations. In [16] a peak around 1 kHz is clearly identified in the numerical curves while it is less evident in the experimental ones. [10] concludes that the results of many experimental modal analyses performed on the TM (with different intact/removed structures of the middle and inner ear) show great variability from specimen to specimen, particularly in the position of the main poles (e.g. the first resonance frequency ranges from about 344 to 1385 Hz).

Many authors agree on considering the TM frequency response below 1 kHz reasonably flat [62], exhibiting a resonance at about 1-1.5 kHz; above this peak the response decreases with frequency, showing other resonances at higher frequencies [10]. Some authors identify a significant resonance at about 3-4 kHz, due to the presence of the ear canal, which is evident in some experimental data and not in others, since this resonance peak will depend on the length and shape of the ear canal and also on the location of the sound delivery system [11, 65].

Several experimental curves of the umbo peak-to-peak displacement frequency response, deduced from the literature, are overlapped in Fig. 1.6. A wide spread of data is evident.

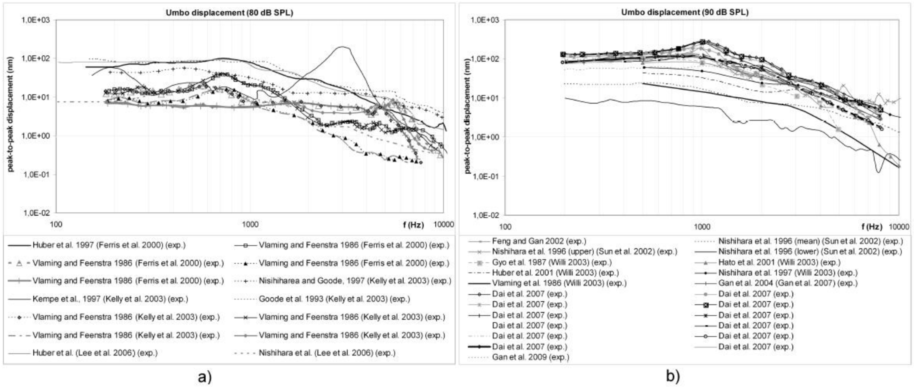

Figure 1.6: Umbo peak-to-peak displacement frequency response curves, deduced from the literature, for an 80 (a) and 90 (b) dB SPL value of input pressure. In the legend the source of data is reported in parentheses.

1.2.2 Ossicular chain

The ossicles

The ossicles (namely the malleus or hammer, the incus or anvil, and the stapes or stirrup, named according to their shapes) represent the smallest group of bones in the human body.

The malleus is the longest of the three ossicles, measuring about 8-9 mm; as shown in Fig. 1.7, it has a long portion named manubrium and an enlarged head. The manubrium is firmly embedded between the layers of the TM, up to the umbo, a reference point that builds the tightest connection between the OC and the TM. The head of the malleus is connected to the body of the incus through the incudo-malleolar joint (IMJ), which plays a key role in the dynamic behavior of the OC.

The incus projects posteriorly by a short process and inferiorly by a long process which terminates in the lenticular process, the lateral aspect of the incudo-stapedial joint (ISJ) while the medial aspect is provided by the head of the stapes.

The neck of the stapes splits medially into two crura attached to the SFP, which has the form of a slightly irregular oval. The SFP is circumferentially connected to the cochlear wall by fibrous connective tissue known as the annular ligament or stapedio-vestibular joint (SVJ) that constitutes a peripheral suspension of the whole OC. The SFP occupies the oval window (OW), an opening between the tympanic cavity and the inner ear. Closed by a membrane, the round window is situated below and behind the OW and vibrates with opposite phase, allowing the movement of the cochlear fluids [3].

Joints

The OC is connected to the TM on the lateral side and to the OW on the medial side and is bound together by two synovial joints, the IMJ and the ISJ, Fig. 1.7.

The IMJ may be classified as a saddle-type joint with curved reciprocal concave-convex surfaces. As nicely reported by Willi in its comprehensive reviews on the IMJ functionality [68, 69], in its comprehensive review on the IMJ functionality, the function of this

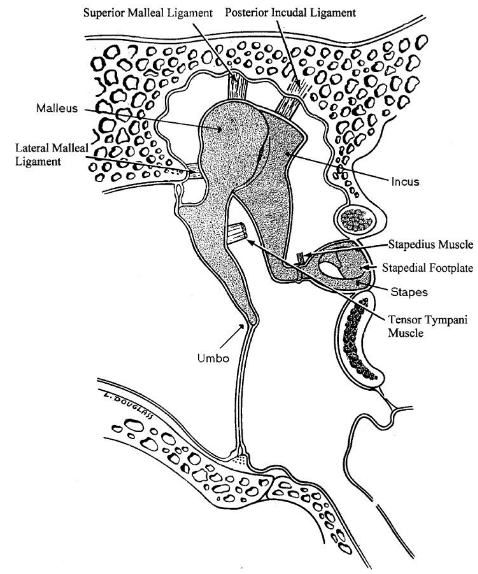

Figure 1.7: Middle ear structure scheme: ligaments, tendons and muscles. (Reprinted from [64] with permission from Elsevier.)

joint gave reason to many discussions and arguing in the literature since the 19^{th} century.

Helmholtz [70] was the first to investigate the anatomy of the IMJ in detail with respect to its function. He proposed a common rotational axis for the motion of the incudo-malleolar complex and a relatively loose union provided by the articular capsule allowing additional degrees of freedom (DoFs). He also suggested a protective mechanism for the delicate incudo-stapedial (ISJ) and the stapedio-vestibular (SVJ) connections.

Later on, other researchers [19, 71, 72] observed, through experimental tests, that no articulation at the IMJ occurs at physiological sound pressure levels (belonging to the 0 120 dB, more typically 80 90 dB, Sound Pressure Level (SPL) range) and at low frequency ($<$ 0.3 kHz), leading to the conclusion that the malleus and the incus vibrate as a single rigid body [11]. Only at extremely high sound pressure levels or high frequencies, above 0.3 kHz and particularly above 10 kHz [72], was any articulation observed, probably to protect the inner ear [73]. In this sense, in [74] Hüttenbrink illustrated the gliding motion between the malleus and the incus when exposed to changes in static air pressure, which can cause displacements of up to 1 mm in the OC, as opposed to the physiologic microscopic acoustic vibrations.

Other indications against the fixed IMJ assumption were presented in the last decade by two research groups [69, 68, 75, 10]. Experimental evidences reported in [69, 68, 10] elucidate a relative motion at the IMJ with three main contributions: the translation in the "piston-like" direction (from the umbo to the stapes, orthogonal to the plane of the OW membrane) and the two rotations around the other orthogonal axes. A mobility of the IMJ in the 75-90 dB SPL range, affecting the middle ear transfer function, was assessed in [69]. Moreover, Ferrazzini [10] showed a slippage of about 20 nm between the malleus and incus even at low or moderate frequencies (75-90 dB SPL).

The malleus and the incus have been long believed to rotate as a single rigid body about a fixed axis at least at low frequencies [28, 76] while a highly frequency dependent rotation axis has been identified above 1 kHz [71, 11, 77].

The ISJ is a synovial shallow ball-and-socket type or enarthrodial joint [6, 74]. There is a general agreement on the anatomy of this joint, which represents the weakest point of the chain and, therefore, is the most subjected to dislocations and fractures [78].

1.2.3 Other middle ear structures

The human middle ear includes also various ligaments, muscles, tendons, nerves and folds of mucous membrane (Fig. 1.7) which surround and support the ossicles restraining their vibratory movements [6, 3, 19].

The malleus is held in place by the TM and also by four ligaments: the superior ligament (SML), the anterior ligament (AML), the posterior ligament (PML) and the lateral ligament (LML), named after their relative position with respect to the malleus itself. The SML suspends the malleus from the superior wall of the tympanic cavity. The AML connects the neck of the malleus to the anterior wall of the tympanic cavity, while the LML connects the lateral side of the TM. The incus is suspended and connected to the cavity wall by its superior ligament and its posterior ligament (PIL), respectively. The base of the stapes (SFP) is connected around its rim to the OW by the stapedial annular ligament (SAL).

Besides, the middle ear contains two muscles, the tensor tympani (TT) (whose tendon is attached to the manubrium of the malleus) and the stapedius muscle (whose tendon (ST) is attached to the neck of the stapes). As reviewed in [6], these muscles were long believed to have a protective role, contracting when the middle ear is exposed to high sound intensities. This "protection theory" has been widely criticized because of an observed noticeable time gap between acoustic stimulation and contraction of the muscles [19]. Alternative theories have been proposed for the reflexive middle ear muscle contraction (acoustic reflex), as the "fixation theory", suggesting that muscles maintain the appropriate positioning and rigidity of the OC, and the "accommodation theory", stating that the muscle action maximizes the absorption of sound energy. Another theory proposes that the reflex function consists in improving the dynamic range by attenuating low-frequency sounds. Hüttenbrink [79] stated that the "fixation theory" is not verified and suggested a protective role in terms of maintenance of the circulation of the synovial fluid in the OC joints.

The TT and the ST muscles are innervated by the trigeminal and facial nerves, respectively. The chorda tympani nerve branches from the facial nerve and crosses the tympanic cavity between the malleus and the incus without actually attaching to the ossicles [80].

The mechanical properties of these soft tissue structures have been investigated and debated in the last years [81, 82, 83], due to the fact that soft tissues usually show viscoelastic behavior in their physiological operating range.

1.3 Inner ear

The inner ear consists of the bony labyrinth, a system of passages mainly comprising two functional parts: the cochlea (a spiral-shaped organ responsible for the transduction of acoustic signals into neurological signals) and the vestibular system, devoted to balance.

The inner ear is mentioned for completeness as it constitutes a fundamental stage in the hearing function. It will not be referenced in the following since the present thesis focuses on outer and middle ear.

Chapter 2

State of the Art

The following literature survey concerns the outer and middle ear. An extensive model-oriented review was conducted focusing on the AC, the TM and the OC.

2.1 Outer and middle ear modeling approaches

Several modeling (in particular bioengineering) approaches have been applied over the past fifty years or so, for simulating and predicting the dynamic behavior of the human hearing organ or prosthetic devices in physiological or pathological/post-surgical/post-traumatic conditions, as reviewed by [14].

The published models can be mainly classified into two broad categories [84]:

- lumped parameter models, including electro-acoustical analogue circuit models [78, 84], electronic and signal processing based models [85], mechanical [86, 87] or MB [88, 89] models;

- distributed parameter models, mainly represented by the FE method, widely applied since 1978 [90], and, extensively, in recent years [15, 91, 92, 93, 94, 95, 96, 97, 67, 98, 99, 100, 65, 64, 66, 62, 101, 16, 102, 103, 104]due to their capability of incorporating the complex geometries and the non-homogenous, anisotropic material (important when the TM is included in the model).

Three numerical solution techniques for nonlinear eardrum-type oscillations (the target function technique, the multiple-parameter technique and the direct integration technique) are proposed in [105]. A numerical simulation of the dynamical properties of the TM is presented also in [106] employing a superposition of waveforms as a model for describing the the vibratory patterns of the coupled system of the tympanum-malleus. A time-domain wave model of the TM was proposed in [84].

The first FE models of the TM were proposed by Funnell et al. since the 70's [90, 107, 108, 109, 110, 91, 111, 112, 113, 114, 34, 37]. A complete computer-aided design (CAD) and FE model of the human middle ear was published also as a patent application in 2006 by Gan et al. [96, 97, 15, 115, 95, 116, 94, 117], extended in 2007 by adding an uncoiled cochlear model. A FE model of the human middle ear was developed in 2006 by Lee et al. [98, 99, 100, 118, 119], who recently [67] have added a “third chamber” (the mastoid cavity) to the “two-chamber” model proposed by Gan et al. [95]. A complete FE model of the human middle ear was proposed by Prendergast et al. [120, 121, 64, 11, 65, 122] in 2000 and used firstly to analyse the normal middle ear and, secondly, to analyse both PORP and TORP prostheses; an application aimed at ventilation tube design is reported in 2008 [122]. In the same years the group of Koike et al. developed and applied an FE model to evaluate geometric variability and different mobility of the human middle ear [101, 16, 10, 102, 14]. Other interesting FE modeling approaches, appeared between 2001 and 2010, focusing on the human TM are reported in [62, 123, 66, 63, 103].

A crucial problem in modeling is the trade-off between the computational burden and the level of detail or approximation. On the one hand, a FE approach can give insight into the mechanical behavior of the single ear component, although leading rather complex models, as observed in [73]. Moreover, as material input data are often scattered or unavailable, due to the difficulties of experimental investigations a model calibration is required, which can be a challenging task. On the other hand, the simplicity of analogue models with few degrees of freedom, based only on impedance measurements, make them convenient to simulate specific aspects of acoustic signal transmission but they provide limited information with respect to the complexity of the actual biological structure.

A mechanical lumped-parameter rigid-body model could represent an intermediate alternative that simplifies the joint modeling and provides good accuracy at a low computational cost since only the essential dynamic aspects are considered. As a drawback, undoubted difficulties arise in the estimation of patient-specific geometric parameters. The MB approach is justified, if applied to the ossicular chain of the middle ear, as for every measured ossicle the first natural frequency is far away from the audible frequency range, filtered by the TM, so that the ossicles can be considered as rigid bodies [73, 10, 124]. As recently commented in [125], such assumption is no longer correct for some thin parts of the ossicles under particular conditions, e.g. quasi-static large sound pressures due to altitude or meteorological changes, especially in animals.

2.2 Outer ear modeling

2.2.1 Auditory canal modeling

Several papers were collected concerning the AC modeling [15, 95, 116, 94, 65, 122, 66, 67, 14, 111, 126, 127, 128, 129, 130, 131, 132].

Geometry

Several solutions have been reported in the literature to obtain the AC geometry:

- through histological section images of a human temporal bone [15, 95, 94, 127];

- through nuclear magnetic resonance spectroscopy [65, 122, 64, 11];

- through (spiral or high resolution) computed tomography data [67, 16, 66, 130];

- from measurements of the mold of a patient [128];

- through the direct scanning of the human external AC by using an electromagnetically actuated torsion micromirror [129].

As an example of typical dimensions, an air volume of ∼1442 mm^3, with 28.6 and 32.1 mm values of canal length superiorly and inferiorly, respectively, is reported in [67]. A volume in the ear canal of ∼1657 mm^3 and a superior, an inferior and along the canal axis length of 25.18, 31.9, 30.22 mm, respectively, are reported in [15]. The cross-sectional area ranges from 65.45 mm^2- 75.53 mm^2 at the TM to 90.13 mm^2- 96.16 mm^2 at the canal entrance, as reported in [67, 15].

Element type and mesh

In the literature, mainly acoustic solid elements were employed in FE analysis to mesh the AC [16, 15, 95, 94] and, particularly, some authors employ the *Ansys*® 3D acoustic element (FLUID30) [65, 64] for modeling the fluid medium and the interface in fluid-structure interaction (FSI). The 3D wave equation and a pressure based formulation are assumed in this element, which has the capability to include absorption of sound at the interface by generating a damping matrix using the surface area and boundary admittance at the interface. Experimentally measured values of the boundary admittance for the sound absorbing material may be input as material property, with values from 0.0 (i.e. no sound absorption) to 1.0 (i.e. full sound absorption). An FSI label, flagged by surface loads at the element faces couples the structural motion and the fluid pressure [133, 134].

Materials

There is a general agreement on assuming a compressible (i.e. density changes due to pressure variations), inviscid (i.e. no dissipative effect due to viscosity) fluid, without mean flow. The mean density and pressure are uniform throughout the fluid and the relatively small acoustic pressure is the excess from the mean pressure.

The air medium values of density (1.2-1.29 kg/m^3) and speed of the sound (334-343 m/s) are typically assumed [15, 67, 64].

Boundary conditions

A uniform input pressure is typically applied at the entrance of the AC. Values of 80[11, 65, 122], 90 [116], 120 dB [67] Sound Pressure Level (SPL) or the atmospheric value [95] are typically assumed.

The temporal bone is not typically included in the FE models and boundary conditions are applied corresponding to the bone wall action. In [67, 64], rigid walls of a bent tube were assumed.

In [15], the surfaces of acoustic elements next to the canal wall were defined as impedance surfaces, with a unitary specific sound absorption coefficient, denoting full absorption, while a 0.04 value of the absorption coefficient (i.e. fraction of absorbed acoustic energy to total incident energy) for the cavity walls is assumed in [67].

2.3 Middle ear modeling

2.3.1 Tympanic membrane modeling

A wide variety of TM FE models can be found in the literature, differing for geometry, mesh/element, boundary condition and material properties. A survey of model main features is reported in this section and next ones and collected in Tab. 2.1 and Tab. 2.2.

Geometry

Sources

Concerning the source of a geometric model of the anatomy of the human and animal TM to be used in FE analysis, many *in vivo* and *in vitro* solutions have been proposed [9, 14]. The geometry of the TM can be based on:

- a simplified parametric geometry (e.g. in terms of a conventionally defined radius of curvature) [90, 107, 62, 63];
- previously published anatomic measurement data [120, 64, 11, 16, 101, 102, 123];
- a 3D reconstruction from serial histological sections [108, 96, 97, 15, 115, 95, 116, 94, 117];
- interferometric techniques (i.e. phase-shift Moir shape measurement) [110, 109, 113, 112, 111, 33, 34, 37, 139];
- nuclear magnetic resonance (NMR) spectroscopy [65, 122];
- micro-Computed Tomography (CT) [91, 114, 10];

Ref.	GEOM	TCK (μm)	EL(N)	CONSTR	SW
[66]	spiral CT	50	shell(3)	sr	Ansys
[96]	histol. sect.	-	-	-	Ansys
[63]	parametric	100	shell	fc	Ansys
[91]	X-ray μCT	(75,200)	shell(3)	fc	SAP IV
[101, 16, 102]	Ref. [19, 21]	Ref. [21]	shell	sp	own
[120]	Ref. [19]	-	plane(8)	fc	-
[123]	Ref. [135]	-	solid(4)	-	Abaqus
[97]	histol. sect.	CAD model	shell(3/4)	sr	Ansys
[15]	histol. sect.	50-100	shell(3)	sr	Ansys
[95]	histol. sect.	50-100	solid(6)	sr	Ansys
[115]	histol. sect.	50-100	shell(3)/solid(6)	sr	Ansys
[98]	HRCT	100	solid(8)	sr	Patran/Ansys
[99]	HRCT	100	shell(4)	sr	Patran/Ansys
[100]	HRCT	100	solid(8)	sr	Patran/Ansys
[67]	HRCT	100	solid(8)	sr	Patran/Ansys
[10]	μCT	74(50-100)	solid(8)	-	SDT*
[62]	Ref. [136]	100	shell(4)	fc	Ansys
[64]	-	Ref. [137]	shell(8)	sp	Ansys
[11]	Ref. [138]	$\neq$ at each n	shell(8)	sp	Ansys
[65]	NMR spectr.	100-800	shell(8)	sp	Ansys
[122]	NMR spectr.	Ref. [19]	shell	sp	Ansys
[117]	histol. sect.	unif	solid(4)	-	Ansys

Table 2.1: A summary of human TM FE models (1st part). Legend: GEOM=source of geometry, TCK=thickness, EL=element type, CONSTR=constraint representation, SW=software, HR=High Resolution, CT=Computed Tomography, NMR=nuclear magnetic resonance, N=number of nodes per element, fc=fully clamped, sp=springs restraint, sr=structural ring, *SDT=Structural Dynamic Toolbox (Matlab,MathWorks),-=not specified.

Ref.	MM	ρ 10^3 (kg/m^3)	ν	DAMP	FR (kHz)
[66]	LE(IS-IS)	1.2	0.3	R(0,0.0001)	$0.1 - 10$
[96]	LE(IS-IS)	-	-	R(0,0.0001)	$0.1 - 10$
[63]	LE(IS-IS)	1.2	0.3	-	< 0.6
[91]	LE(IS-IS)	–	0.3	neglected	$0.25 - 0.3$
[101, 16, 102]	LE(IS-IS)	1.2	0.3	R(260,$3.7 \cdot 10^{-5}$)	$0.1 - 10$
[120]	LE(IS-IS)	1.1	0.33	-	-
[123]	LE(IS-IS)	-	0.3	-	-
[97]	LE(OR-IS)	1.2	0.3	R(0,0.0001)	$0.25 - 8$
[15]	LE(OR-IS)	1.2	0.3	R(0,$0.75 \cdot 10^{-4}$)	$0.2 - 8$
[95]	LE(OR-IS)	1.2	0.3	R(0,$0.75 \cdot 10^{-4}$)	$0.2 - 10$
[115]	LE(OR-IS)	1.2	0.3	R(0,$0.75 \cdot 10^{-4}$)	$0.2 - 10$
[98]	LE(OR-IS)	1.2	0.3	R	$0.1 - 8$
[99]	LE(OR-IS)	1.2	0.3	R	$0.1 - 8$
[100]	LE(OR-IS)	1.2	0.3	R	$0.1 - 8$
[67]	LE(OR-IS)	1.2	0.3	R	$0.2 - 8$
[10]	LE(OR-IS)	1.2	0.3/0.4	H	$0 - 4.5$
[62]	LE(OR-OR)	1.2	(0.35-0.43)	-	$0.1 - 10$
[64]	LE(4OR+1IS-IS)	1.2	-	R(260,$3.7 \cdot 10^{-5}$)	$0.2 - 10$
[11]	LE(4OR+1IS-IS)	-	-	-	$0.1 - 8$
[65]	LE(4OR+1IS-IS)	-	-	R(260,$3.7 \cdot 10^{-5}$)	$0.1 - 10$
[122]	LE(4OR+1IS-IS)	-	-	-	$0 - 6$
[117]	NL HE/LE(OR)*-LE(IS)	-	-	R	$0.2 - 8$

Table 2.2: A summary of human TM FE models (2^{nd} part). Legend: MM =Material model, ρ=density, ν(PT-PF)=Poisson’s ratios, DAMP=material damping, FR=frequency range [Hz] of validity, LE=linear elastic, NL=nonlinear, HE=hyperelastic, IS=isotropic, OR=orthotropic, TI=transversely isotropic, MLC=multilayered composite, R(α [s^{-1}],β [s])=Rayleigh’s damping, H=hysteretic, *static/dynamic analysis, -=not specified.

- spiral CT or High-Resolution Computed Tomography (HRCT) [66, 98, 99, 100, 118, 119, 67] of living human temporal bones.

Thickness

The human TM thickness is discussed in many works as a critical parameter with the greatest effects on results. Although there is a general agreement in considering a non-homogeneous distribution of thickness in different locations of the TM, a uniform thickness value, ranging from 30 μm to 150 μm for the human TM is usually adopted [8, 9, 40, 13, 66]. In [63, 62, 98, 99, 100, 67] a 100 μm value is assumed, while in other works a different thickness between PT and PF [91, 65] is considered. Most authors agree to adopt an average value around 74 μm [8, 15, 26, 35, 32, 14, 31, 10].

The first refinement in thickness representation was made by [140], who specified 10 thickness regions in their FE model, based on 10 thickness values measured by [22]. [141, 142, 143] assumed the same thickness representation for the human TM. Basing on the same data, [16] constructed a model with a slightly more detailed thickness distribution of the TM.

It is worth stressing that, according to many authors [40], the thickness should be related to the Young's moduli assigned to the different regions, therefore different combinations of thickness and elasticity could involve similar results.

Materials

Elastic behavior: models

The question of whether the gross mechanical properties of the (animal or human) TM are isotropic/anisotropic and uniform or not, have been investigated since the 40's [27, 28, 19] but it is still difficult to draw quantitative conclusions about this issue [8].

Mainly linear elastic (LE) models are implemented in the literature. The viscous behavior of the TM tissues, widely investigated in recent experimental activities [26, 13, 35], is introduced in the models as material damping. The main relevant distinction is between isotropic (IS) and anisotropic (and in particular orthotropic (OR)) materials. The multi-layer fiber ultrastructure of the PT, supported by an arrangement of collagen fibers organized into a matrix of ground substance along radial and circular directions, suggests the importance of considering the anisotropic material properties of this sub-membrane; in particular the collagen fiber alignment suggests the choice for an orthotropic material for the PT. Even if the PF ultrastructure is composed of distinct layers, the elastic properties are due to a random distribution of elastin filaments; a regularly and compactly arranged collagen fiber organization is not present in the PF [12]. Therefore an homogeneous isotropic material is commonly assumed for the PF. In the reviewed literature isotropic material models for both the PT and the PF (with equal or different Young's modulus values) have been proposed in [90, 63, 120, 16, 101, 102, 123, 96, 110, 109, 113, 91, 66, 112]. While they both are considered orthotropic in [62], many studies assume an orthotropic PT and an isotropic PF, respectively [90, 97, 15, 115, 95, 110, 98, 99, 100, 67, 14]. Other authors [64, 11, 65, 122] implement a 6-part material model (4 orthotropic and 2 isotropic), shown in Fig. 4.2.

A multilayered orthotropic composite structure of the TM has been considered in [111, 114]. In [111], since the overall membrane thickness is considered to taper linearly, the elastic modulus within the fiber layer decreases as $1/r$ from the umbo to the outer edge. In [114] distinct models for the radial and circumferential fibrous layers, as well as two layers corresponding to the combined epidermal and subepidermal layers and the mucosal and submucosal layers are developed. A nominal Young's modulus of 0.1 GPa is assigned to both the radial and circumferential fibers so that these fibrous layers are modeled as transversely isotropic materials, oriented with the observed fiber directions. Young's moduli of the radial fibers are normalized by the local thickness in order to compute a local equivalent modulus for the layer. In the inferior part, the radial fiber moduli increase as $1/r$ relatively to the umbo location. The matrix material and outer layers are assumed to have an isotropic Young's modulus of 1 MPa, corresponding to a soft tissue reinforced with elastin. The PF has an isotropic Young's modulus of 1 MPa due to the non-oriented collagen and elastin fibers in the matrix.

Nonlinear hyperelastic models for the TM characterization were used in [117, 26, 12]. An in-depth study of a TM constitutive model is described in [117]. A five-parameter hyperelastic Mooney-Rivlin model for incompressible material is utilized to represent the 3D constitutive relations of the PT in a quasi-static analysis. Material properties of the TM and other middle-ear tissues have been measured by using uniaxial tensile tests. Variations of the mechanical parameters with stress and in dynamic analysis are also reported in the same work. An Ogden model was applied to analyze experimental data obtained with uniaxial tensile, stress relaxation, and failure tests conducted on fresh human cadaver specimens of the TM in [26]. The Veronda-Westmann hyperelastic model was introduced by [12] to describe the gerbil PF behavior.

Linear elastic parameter values

If an isotropic material model is adopted, Young's modulus (E) and Poisson's ratio (ν) are the usual inputs, while the shear modulus (G) is obtained by the well-known formula

$$G = \frac{E}{2(1+\nu)} \tag{2.1}$$

In the reviewed papers, where isotropy is assumed, Young's moduli for human, where not alternatively specified, TM are widely distributed, as shown in Tab. 2.3, ranging from 1.5 MPa to $20 \cdot 10^3$ MPa for the PT and from 0.5 MPa to $10 \cdot 10^3$ MPa for the PF. In the isotropic case a 0.5 value of the Poisson's ratio can be assumed for incompressible materials while, for a material composed of parallel fibers with no lateral interaction among the fibers, Poisson's ratio should be considered zero for a stress applied in the direction of the fibers. A value of 0.3 for the Poisson's ratio of the TM can be adopted as a compromise [8].

In most cases an orthotropic model is assumed for the PT while an isotropic one is used for the PF. If an orthotropic material model is assumed, nine parameters (three Young's moduli (E_X, E_Y, E_Z), three Poisson's ratios (ν_{XY}, ν_{XZ}, ν_{YZ}) and three shear moduli (G_{XY}, G_{XZ}, G_{YZ})) must be used as input. In a plane stress element, which is commonly assumed in TM models, they reduce to four in-plane parameters: E_X, E_Y, ν_{XY} and G_{XY}.

Young's moduli values for the orthotropic material models adopted for regions of the human, where not alternatively specified, TM are reported in Tab. 2.3. Radial and circumferential Young's moduli values for plane stress elements are typically adopted, except in [10], where optimized values for the Young's moduli are obtained (0.9 MPa for the PF, 4 MPa, 1 MPa, and 0.9 MPa in the radial, circumferential and thickness directions of the PT, respectively) starting from initially assumed orthotropic PT (32-40 MPa radial; 20-40 MPa circumferential) and isotropic PF (11-14 MPa) as guess values for the parameter identification procedure.

Only few authors debate the shear modulus issue. In [90] the shear moduli is set to zero, assuming that the radial fibers slide over one another without interaction, but this assumption is not supported by experimental evidences. In [30] the shear modulus is varied from a large value similar to the fiber stiffness to a very soft value comparable to loose connective tissue or ground substance. In [10] an initial 93 MPa value and estimated shear moduli of the PT are reported (0.8 MPa, 0.9 MPa, 9 MPa in the radial, circumferential and thickness directions respectively) while in [62] a 6.2 MPa value for the PT and a 8.5 MPa value for the PF are assumed. In [114] this issue is extremely debated as a key parameter connected to microstructural details of the TM; a 35 MPa value of the shear modulus is mentioned, in order to fit experimental observations.

It is worth noting that, in the orthotropic case, even if Poisson's ratios may be specified in two formulations, denoted major and minor forms, related through the corresponding Young's modulus values, it is not always specified which convention has been adopted. In the reviewed works, there is a general agreement on setting a 0.3 value for the human and animal TM Poisson's ratio [90, 107, 63, 16, 101, 102, 123, 97, 15, 115, 95, 94, 110, 91, 66, 98, 99, 100, 118, 119, 67, 14, 8, 112, 17] as for the isotropic case and on the lack of relevant experimental data, even if motivation of this choice represents a controversial issue: some authors consider its influence negligible on simulation results [90, 8, 63, 97, 91, 14, 9] while other authors point out the necessity of further investigation on the influence of varying this parameter in biological material modeling, proposing other values as zero value [90, 110] or values closer to 0.5 [120, 113, 35, 13, 114, 34] since a 0.5 value [30] (i.e. incompressibility) can cause computational problems. Different values (0.3-0.35 and 0.4-0.43 respectively) for the PT and PF of the TM are reported in [10, 62].

Material damping

Rayleigh damping is a classical and probably the most common method to easily build the damping matric **C** of a numerical model, under the following form [144]:

$$\mathbf{C} = \alpha\mathbf{M} + \beta\mathbf{K} \tag{2.2}$$

where **M** and **K** represent the mass and the stiffness matrix, respectively. Many authors, instead of neglecting damping effects, introduce material damping in their models in terms of Rayleigh damping parameters (α [s^{-1}], β [s]) [109, 110, 96, 97, 15, 115, 95, 116, 94, 117, 64, 65, 101, 16, 14, 98, 99, 100, 118, 67, 66]. There is not a general agreement on α and β values, as shown in Tab. 2.2. In [114] a complex elastic modulus is used for each component to model material damping effects. So this simple viscoelastic model adds an imaginary component to the stiffness that does not increase with frequency. Hysteretic (or structural) damping is described in [10].

Density

Many authors agree on setting both the human and animal TM

	PT	PF	Ref.	PT	PF	Param.
LE	IS	IS	[66]	32	32	E
			[96, 63]	20	20	E
			[113](gerbil)	60	20	E
			[91]	40	20	E
			[16, 101, 102]	33.4	11.1	E
			[109](gerbil)	20	2	E
			[90, 110, 112](cat)	20	1	E
			[120]	1.5	0.5	E
			[123]	$20{\cdot}10^3$	$10{\cdot}10^3$	E
	OR	IS	[90, 110](cat)	20 0.1-0.2	1 1	E_r E_c
			[97]	32 20	10 10	E_r E_c
			[15, 95, 115, 98, 99, 100, 67]	35 20	10 10	E_r E_c
			[10]	32-40 20-40	11-14 11-14	E_r E_r
			[10]	4 1 0.9	0.9 0.9 0.9	E_r E_c E_z
	OR	OR	[62]	85.7 48	45.6 20	E_r E_c
	1IS+4OR	IS	[64, 11, 65, 122]	20,26.6,33.3,40,40 40,33.3,26.6,20,40	10 10	E_r E_c
	MLC (TI+IS)	IS	[114](cat)	100 1	1 1	E_f E_m
NL HE	MR	LE	[117]	0.4196,-0.2135,1357.8,-2843.5,1496.7	1	c_{ij},E
	OGD	OGD	[26]	0.46,26.76	0.46,26.76	μ_1,α_1
	-	VW	[12](gerbil)	- -	3.1±0.4,2.5±0.2 2.6±0.6,1.4±0.2	C_1,C_2 $C_1^{\epsilon_R}$,$C_2^{\epsilon_R}$,$\epsilon_R = 12 \pm 2\%$

Table 2.3: Material models. Legend: LE=linear elastic, NL=nonlinear, HE=hyperelastic, MLC=multilayered composite, MR=Mooney-Rivlin model, OGD=Ogden model,VW=Veronda-Westmann model, IS=isotropic, OR=orthotropic (TI=transversely isotropic), r=radial, c=circumferential, z=out-of-plane direction (thickness),=fiber, m=matrix, E_i(MPa)=Young's modulus, $i = r, c, z, f, m$

density value to that of water (10^3 kg/m^3) or that of undehydrated collagen ($1.2 \cdot 10^3$ kg/m^3) or to values included within this range [8, 109, 110, 111, 114, 10, 66, 63].

Element type and mesh

Concerning the FE modeling, different element types have been employed to mesh the animal or human TM geometry [14, 35]:

- (mainly) shell elements [90, 107, 62, 63, 64, 11, 16, 101, 102, 108, 97, 15, 115, 116, 113, 65, 122, 91, 66, 99, 112, 103, 13, 37, 34, 143], eventually thin shell elements combined with thin beam elements coincident with the common nodes in adjacent shell elements to represent the fiber structure [121].

- solid (tetrahedral, pentahedral or hexahedral) elements [123, 115, 95, 94, 117, 98, 100, 118, 119, 67, 10], especially in models accounting for fluid-structure interface between the air (filling the AC and the middle ear cavity) and the surrounding tissues modeled as structural parts.

The FE software codes where the mentioned models have been implemented in, are reported in Tab. 2.1.

Boundary conditions

Constraints

Boundary conditions at the periphery of the TM represent a critical issue [8]. As previously inferred, the annular ligament (AL) is the thickened peripheral edge of the PT attached to a groove in an incomplete ring of bone, the cartilagineous tympanic annulus (TA), which almost encircles it and holds it in place.

Different boundary conditions have been proposed to model the connection of the TM to the bony wall of the ear canal (Tab. 2.1):

- the periphery of the TM is assumed to be fully clamped (fc) to the ear canal [90, 8, 107, 112, 62, 63, 120, 113, 91];
- the TA is represented as a structural ring (sr) and in particular as a linear elastic shell [97, 15, 115] or a solid (pentahedral or tetrahedral) element structure [115, 95, 94, 100, 118, 67];
- the TM is constrained by linear and torsional springs (sp) in the longitudinal direction [64, 11, 16, 101, 102, 65, 122]. In some works, in the spring representation of the TA, due to the lack of the tympanic ligament in the superior portion of the TM, the stiffness of the springs in the superior portion is assumed to be less than that in the inferior portion [16, 101].

The inclusion of the AL or the TA modeled as structural parts, involves the fact that material parameters are required. Concerning the material parameters, a linear elastic material model is assumed for the tympanic AL: a 0.6 MPa values for the Young's modulus is adopted in [96, 15, 115, 95, 66] while a 2.5 MPa value in [94] and a 6 MPa value in [98, 99]. To simulate the flexible support around the periphery of the TM, the TA was modeled as an elastic ring of 0.2 mm width and 0.2 mm thickness in [97] with a Young's modulus initially assumed identical to the radial value for the TM, and then adjusted as 0.6 MPa through an FE model cross-calibration process. In [97] the Young's modulus of the part corresponding to the notch of Rivinus is assumed to be one third of that of the annulus while the Young's modulus of the part which divides the TM into PT and PF, is assumed to have the same Young's modulus of the PT.

The introduction of spring elements at the periphery of the TM, involves the assessment of suitable spring constants. In [64] the periphery of the TM was restrained against radial motion and was sprung along the longitudinal direction with 34 springs of 75 N/m stiffness giving a stiffness per unit length of $8.36{\cdot}10^4$ N/m^2. *Ansys*® COMBIN14 spring elements are employed in [11]. Spring constant values are reported in [101, 16]: a $3\ {\cdot}10^3$ and a $1.5{\cdot}10^5$ N/m per unit length value for the superior and the inferior portion respectively for the linear springs; $3{\cdot}10^{-5}$ and 10^{-4} Nm per unit length for the superior and the inferior portion respectively for the torsional springs.

Acoustic loading

A uniform harmonic input pressure stimulus of 80 dB Sound Pressure Level (SPL) [64, 11, 65, 122, 101, 98, 99, 62] or 90 dB SPL [91, 96, 15, 95, 117, 10, 123] is frequently applied to the lateral side of the TM or at the opening of the ear canal, corresponding to a 0.632 Pa value of pressure.

Other values (in the range $80-120$ dB SPL corresponding to 0.2 Pa and 20 Pa respectively) [120, 16, 67, 63, 97] are commonly applied as input sound pressure to the lateral side of the TM or at the opening of the AC in the numerical and in the experimental practice.

Model assembly: included parts

A critical issue arises in comparing FE results since models can include different parts of the ear in addition to the TM. Some authors investigate the behavior of the decoupled TM including sometimes boundary conditions that mimic the ossicular and eventually inner ear loading [90, 107, 112].

Several middle ear models in the literature include the ossicles and sometimes ligaments, tendons and muscles [108, 91, 113, 114, 97, 120, 101, 10, 102, 98, 99, 62, 123, 143, 145].

Complete models (including the air-filled AC and/or the middle ear cavities and/or the inner ear structures) have been developed in recent literature [96, 15, 95, 94, 117, 64, 11, 65, 122, 16, 67, 66, 103].

In §4.1, in order to compare different models, the TM has been considered decoupled from the other parts.

2.3.2 Ossicular chain modeling

Ossicle modeling

In order to simulate the vibratory behavior of the OC, geometric, inertial and material ossicle data are necessary. In FE analyzes, the geometry is usually derived by several imaging techniques, mainly:

- ex-vivo micro-computed tomography (μ-CT) scanning of temporal bones e.g. [65, 146];
- scansion and segmentation of histological sections of temporal bones [104, 96, 97];

Reference	Length (mm)		
	Malleus	Incus	Stapes
[15]	8.11 4.71(lateral)	6.02 (long) 4.58(short)	2.66 (height) 2.64 (SFP length) 1.32 (SFP width)
[102]	5.16 (manubrium)	4.99 (short) 4.36 (long)	3.32 (height) 3.03 (SFP major axis) 1.48 (SFP minor axis)
[14]	7.6-9.1 4.20-5.8 (lateral) 5.01-5.14 (lat-head)	6.02-7.74 (long) 4.16-5.12 (short)	2.5-4 (height) 2.40-3.36 (SFP length) 0.7-1.66 (SFP width) 0.474-0.95 (thickness)
[98]	7.48-8.12 4.17-4.41 (lateral) 4.40-5.90 (lat-head)	6.08-6.71 (long) 3.97-4.49 (short)	2.83-3.19 (height) .99-2.52 (SFP length) 0.91-1.39 (SFP width) 0.39-1.25 (thickness)
[99]	7.44-8.13 4.15-4.42 (lateral) 4.39-5.91 (lat-head)	6.08-6.76 (long) 3.95-4.49 (short)	2.81-3.19 (height) 1.99-2.53 (SFP length) 0.92-1.41 (SFP width) 0.37-1.25 (thickness)

Table 2.4: Geometric data of the ossicles according to the literature

- high-resolution magnetic resonance micro-imaging (micro-MRI) of human cadaver [62];
- in vivo spiral [66] or high-resolution [67] CT.

Mean anatomical estimations of the ossicle geometry are summarized in Tab. 2.4.

As far as density is concerned, ossicles are generally considered as non-homogeneous, with values ranging from 2.5 to $6.2 \cdot 10^3$ kg/m^3, as detailed in Tab. 2.5.

The resulting masses of malleus and incus are similar, about 23-30 mg, while the stapes is smaller 2-3.7 mg, Tab. 2.6.

On the other side, the ossicles are considered as made of a uniform, isotropic and linear elastic material, with a considerable dispersion of Young’s modulus from 14 to $2 \cdot 10^4$ MPa, (Tab. 2.7).

Reference	Density (kg/m^3)		
	Malleus	Incus	Stapes
[95, 11, 67, 97, 66, 100, 147, 148, 149]	$2.55 \cdot 10^3$(head) $4.53 \cdot 10^3$(neck) $3.7 \cdot 10^3$(handle)	$2.36 \cdot 10^3$(body) $2.26 \cdot 10^3$(short) $5.08 \cdot 10^3$(long)	$2.20 \cdot 10^3$
[120]	$2.2 \cdot 10^3$	-	-
[102]	$2.5 - 6.2 \cdot 10^3$	$2.5 - 6.2 \cdot 10^3$	$2.5 - 6.2 \cdot 10^3$
[14]	$2.55 \cdot 10^3$-$2.67 \cdot 10^3$(head) $4.53 \cdot 10^3$-$6.15 \cdot 10^3$ (neck) $2.67 \cdot 10^3$-$3.7 \cdot 10^3$(handle)	$2.36 \cdot 10^3$-$2.7 \cdot 10^3$(body) $2.26 \cdot 10^3$-$2.7 \cdot 10^3$(short) $5.08 \cdot 10^3$-$5.86 \cdot 10^3$(long)	$2.20 \cdot 10^3$
[62]	$3.3 \cdot 10^3$	$3.3 \cdot 10^3$	$3.3 \cdot 10^3$
[146]	$2.09 \cdot 10^3$-$2.68 \cdot 10^3$ $2.31 \cdot 10^3$ (mean)	$2.02 \cdot 10^3$-$2.23 \cdot 10^3$ $2.14 \cdot 10^3$(mean)	-

Table 2.5: Density data of the ossicles according to the literature

Reference	Mass (mg)		
	Malleus	Incus	Stapes
[95]	30.42	26.47	1.93
[14]	23-30.42	24.77-32	1.93-4.35
[150]	24.1±1.5 (male) 23.9±1.8 (female)	26.5±1.6 (male) 25.6±1.4 (female)	3.7±0.4 (male) 3.4±0.4 (female)
[146]	26.2-35.1 29.3 (mean)	25-38.7 30.2 (mean)	-
[88]	25.20	27.60	3.360

Table 2.6: Masses of the ossicles according to the literature

Reference	Young's modulus (MPa) Malleus/Incus/Stapes
[120]	$0.75 \cdot 10^3$ (malleus)
[16, 101, 102]	$1.2 \cdot 10^4$
[14]	$1.2 \cdot 10^4$-$1.41 \cdot 10^4$
[62]	$2 \cdot 10^4$
[91]	200
[15, 95, 67, 96, 97, 66, 98, 123, 99, 100, 148, 147, 149]	$1.41 \cdot 10^4$
[11]	14.1
[125]	$1.6 \pm 0.3 \cdot 10^4$

Table 2.7: Young's moduli of the ossicles from the literature

In the literature, there is a general agreement on assuming a 0.3 value for the Poisson's ratio for the ossicles, as well as for the other middle ear components.

In lumped parameters models, the ossicles, considered as rigid bodies, are characterized by a mass, a center of mass and a principal inertia tensor. Unfortunately, the inertia tensors and the position of the centers of mass of the ossicles are rarely reported in the literature,except in [88, 151, 152].

Because of the complexity of measuring the damping properties of the middle ear [14], in FE models the damping response of the ossicles and of the other elements is typically included in terms of Rayleigh parameters. Typical values are $\alpha = 0$ s^{-1} and $\beta = 0.75 \cdot 10^{-4}$ s in [15, 95], $\alpha = 0\ s^{-1}$, $\beta = 10^{-4}$ s in [97].

Joint modeling

The OC motion depends on the described joints, whose modeling is complex and crucial. The joints between the malleus and the TM (TMMJ) and between the stapes and the OW (SOWJ) are fibrous joints, usually modeled with solid elements; for the TMMJ typical density and Young's modulus values are 10^3 kg/m^3 and $4.7 \cdot 10^3$ MPa while the SOWJ is assumed to be twice as dense and with a wider dispersion in the elastic constant, 0.065-0.49 MPa.

Structural and functional features that distinguish the synovial IMJ and ISJ (i.e. the synovial capsules surrounding the articulating surfaces and the lubricating synovial fluid within those capsules) are typically reduced in FE models of the middle ear to elastic interfaces connecting the articulating surfaces. In particular for the ISJ, a portion of elastic ligamentous tissue is usually interposed between the two adjacent ossicles, whose characteristics, in terms of density and Young's modulus, are $1.2 \cdot 10^3$ kg/m^3 and 0.6 MPa respectively [15, 97]. However, recently two studies on the ISJ modeling were presented, one on a sub-structured FE model of the cat joint [153], the other one on an experimentally-calibrated FE model with hyperelastic tissue characterization [104].

The disagreement on the role of the IMJ, reported in §1.2.2, motivated alternative solutions for the modeling of this joint:

- similarly to the ISJ, i.e. as a layer of tissue, but with same Young's modulus of the ossicle, therefore acting as a continuous connection (0 DoFs) between the malleus and the incus [15, 95, 97, 66];
- in [11, 65] it is modeled by linking the malleus and the incus with stiff three dimensional truss spar elements;
- in [98] a rigid coupling between the FE nodes of the articulating surfaces is imposed;
- in [73, 87] it is considered as fixed (i.e. allowing no relative degrees of freedom);
- a two rotational axis (infero-superior and antero-posterior) joint is assumed in [152];
- in [154] an ideal pin joint scheme is adopted;
- in [123, 155, 148] a contact formulation with a basic Coulomb friction model is employed;

- in [104, 156] it is considered as a standard linear viscoelastic material with different material parameters ($E_0 = 40/60$ MPa, $E_1 = 240/180$ MPa, $\tau_1 = 20\ \mu$s).

All these references, as well as indications reported in §1.2.2, allow to infer that the IMJ modeling represents a critical aspect, due to the wide spread of solutions ranging from 0 (zero) to an effective 6 DoF joint.

In FE models the viscous part of the joint behavior is typically included in terms of Rayleigh parameters ($\alpha = 0$ s^{-1}, $\beta = 0.75{\cdot}10^{-4}$ s [15, 95], $\alpha = 0\ s^{-1}$, $\beta = 5 \cdot 10^{-4}$ s [65, 16]. In the lumped parameter mechanical model of [157], the viscous damping constants for the joints of the OC are reported within the range 0.001-0.5 Ns/m.

Modeling of other structures

The vibratory behavior of the OC is strongly affected also by the supporting structures, as ligaments and tendons, which should be properly modeled.

Commonly, in FE simulations they are included as solid components, whose geometry is determined on the basis of imaging techniques [15, 16, 101] or simply assumed as a parallelepiped [65]. Nonlinear hyper-elastic models proved to be suitable to represent the constitutive relation of ligaments and tendons and in particular of the ST [81][158], the TT tendon [82], the AML [83] and all of them [148, 117]. However, due to the reduced amplitude of the vibratory motion, their behavior may be locally approximated by a linear elastic assumption, e.g. [65, 98]. However, because of the difficulties involved with the experimental measurement of the properties

Reference	Young's modulus (MPa)					
	SML	AML	LML	PIL	TT	ST
[123]	$2 \cdot 10^3$	$2 \cdot 10^3$	$2 \cdot 10^3$	$2 \cdot 10^3$	-	-
[91]	20	20	-	20	-	-
[15, 95, 67]	4.9	21	6.7	6.5	70	52
[64]	-	21	-	0.65	-	-
[11, 65]	0.65	21	0.65	0.65	2.6	-
[16, 101, 102]	-	21	-	0.65	2.6	0.52
[14]	0.049-4.9	2.1-21	0.067-6.7	0.65-6.5	2.6-70	0.52-52
[66, 98, 99, 100, 155, 148, 97, 96]	0.049	2.1	0.067	0.65	2.6	0.52
[149]	4.9	21	6.7	6.5	8.7	52
[94]	4.9	8	6.7	6.5	8	10

Table 2.8: Young's moduli of the superior mallear ligament (SML), anterior mallear ligament (AML), lateral mallear ligament (LML), posterior incudal ligament (PIL), tensor tympani muscle and tendon (TT), posterior stapedial muscle and tendon (ST) from the literature.

of biological soft tissues, there is a wide dispersion of these data in the literature. Therefore, in most cases the mechanical properties used in the simulation models are defined on the basis of some measurements and then validated through a cross-calibration process [15, 14, 97, 16]. In Tab. 2.8), the Young's moduli of the abovementioned ligaments and tendons, mainly deduced from previously published experimental data or obtained through a calibration procedure, are reported, showing a dispersion even of some orders of magnitude.

Viscoelastic material properties for the SAL and for the round window membrane have been recently employed in [104, 156]. In a MB approach, tendons and ligaments are usually represented as spring and damper elements, whose properties are determined again by means of a calibration procedure.

It can be worth adding that nerves typically are not modeled.

End interfaces

In the last years, meaningful advances were made for including the cochlea in FE models, as an uncoiled [94, 93] or a spiral cochlea [104, 156], for understanding its function and interaction with the middle ear structures. More frequently, the effect of the cochlear fluid on the OC is taken into account by means of an equivalent cochlear load, represented by lumped parameters elements, as viscous dampers [64, 102], viscous dampers with mass [15, 95], spring-dashpot elements [67, 98] or more complex structures [10].

Such equivalent lumped systems are usually identified in terms of acoustic input cochlear impedance, defined as the ratio of sound pressure in the cochlear cavity at the SFP to the volume of fluid the SFP displaces per unit time (Pa s/m^3), whose experimental estimation can be found in the literature, e.g. [159, 160]. A viscous damper (0.62-0.89 Ns/m) was used by Koike and co-workers [101, 16, 102] giving a 50 $G\Omega$ impedance, deduced from measurements of [160] in the 0.1 5 kHz frequency range. A similar value (0.717 Ns/m) was also used in [64], based on a higher estimate of the cochlear impedance (70 $G\Omega$), derived from the stapes displacement measurements reported in [160]. In [67, 98] a distribution of 49 spring-dashpots elements on the SFP with constants of 60 N/m and 0.06-0.07 Ns/m, respectively, was adopted to simulate the action of the cochlear fluids. In [15, 95] a 20 $G\Omega$ cochlear impedance (based on [159, 160]) was obtained as a mass block of 25.5 mg with 10 dashpots of 0.02 Ns/m, five on each side of the mass, attached between the SFP and the bony wall. As far as the TM is concerned, while in the FE models it is almost always modeled (see [161] for a review), in the lumped parameter or mechanical models it is introduced as a mass element [88, 157] or omitted [86].

Model inputs and outputs

The kind of input used in the literature can be different, depending on which parts of the middle ear are modeled. When the AC is included, the input is a sound stimulus applied at 2 mm away from the umbo in the ear canal [93] or at the inlet (concha) of the ear canal [65]. Frequently, when the TM is included, the typical input is a uniform sound pressure in the 80-120 dB SPL range, applied on the lateral side of the TM [15].

When only the dynamics of the OC is considered, the displacement of the umbo, as a point of the malleus, in the ”piston-like” direction, can be assumed as reference input of the model. Although the TM could transmit also other displacement components to the malleus, they have been rarely measured [72] and are usually left as free DoFs.

Another crucial aspect in this kind of simulations is the choice of the model output, which should be representative of the sound transmission efficiency and consequently of the vibratory motion of the ossicles.

The most frequent output in the literature is the SFP displacement amplitude. An alternative representative parameter is the so-called lever ratio (LR), that is the ratio of the displacement of the umbo to the displacement of the stapes head, as defined in [76, 16], or viceversa [11]. The ratio of the umbo displacement to the SFP displacement is reported in [97, 162]. As stressed in [71, 77], the

LR issue is strictly related to the site of the rotation axis and it should be reexamined when the axis position is highly frequency dependent. Although initially the value of LR was assumed frequency-independent (∼1.31) (i. e. fixed axis) [76], more recently a highly frequency dependent displacement ratio was reported in [97, 16, 162], typically included in the 1.3-10 range [71]. In addition, it can be worth mentioning that alternative definitions of LR are adopted in the literature, e.g. [163, 51].

In order to give an example of the behavior of the middle ear, in Fig. 2.1 the peak-to-peak displacement of the umbo (a) and of the SFP (b) deduced from experimental and numerical literature results (for 90 dB SPL of input pressure) are superimposed and the consequent LR, computed as the ratio between the SFP and the umbo displacement, is shown in Fig. 2.2.

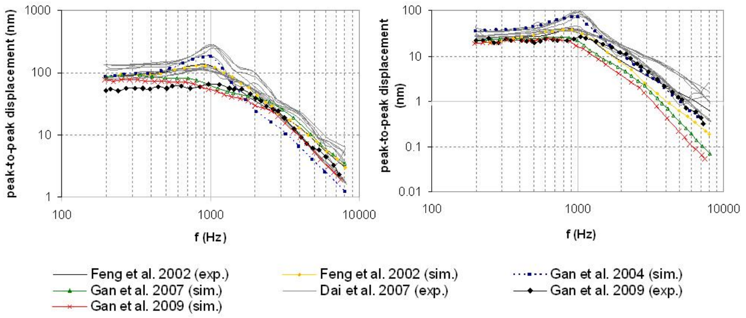

Figure 2.1: Umbo (a) and SFP (b) peak-to-peak displacement curves deduced from the literature for 90 dB SPL of input pressure (exp.= experimental, sim.=simulated data)

Below 1 kHz the umbo and SFP responses are quite flat; beyond a peak of resonance, the curve decreases; a pronounced second

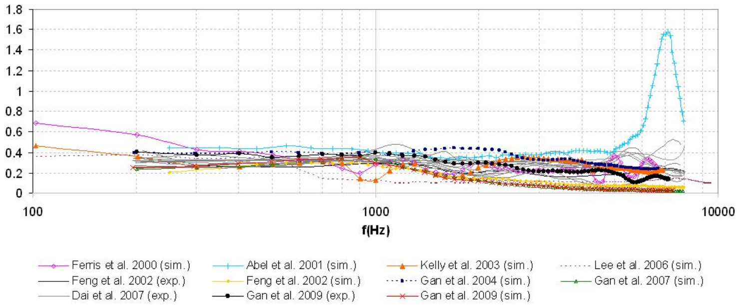

Figure 2.2: Lever ratio function deduced from literature data for 80 and 90 dB SPL of input pressure (exp.= experimental, sim.=simulated data)

resonance at about 3-4 kHz is reported by some authors [65, 62]. Although a general trend of the curves is evident, a wide dispersion of the shown results unavoidably mirrors the wide range of available data and parameters.

It is worth noting that the umbo and SFP displacement phase angle is rarely reported [157, 94, 93], Fig. 2.3.

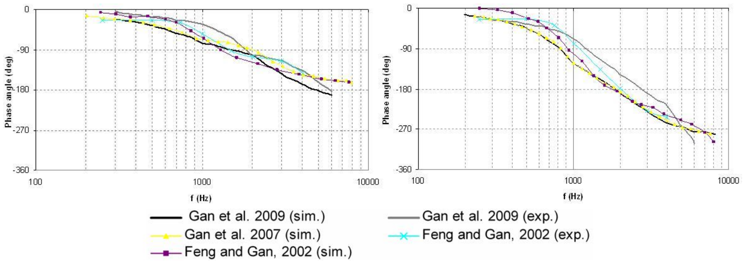

Figure 2.3: Umbo (a) and SFP (b) displacement phase angle curves deduced from the literature [157, 94, 93] for 90 dB SPL of input pressure (exp.= experimental, sim.=simulated data)

It has to be remarked that the OC proved to behave linearly within the range of input pressure from 80 to 120 dB SPL [97]. Due to the linearity of the OC in the input range of pressure amplitudes, the LR vs. frequency trend overlaps for different input pressure levels as can be ascertained from Fig. 2.2. A significant variability also in the experimental and numerical LR curves appears, consequent to uncertainties in experimental measurements (hindered by the scale of the variables) and in parameter setting, respectively.

It can be worth mentioning that many alternative outputs have been proposed, e.g. normalized variables such as the displacement transfer functions of the stapes and of the TM [15] the sound pressure gain or transmission gain/factor [101, 94, 102] and, more generally, the recorded and monitored pressure at different locations (e.g. near the OW or round window, ISJ [95] or umbo) inside the middle ear; the impedance of the middle ear [65]; modal and harmonic analysis results which are frequently presented in terms of eigenfrequencies and displacement distributions [62, 123], velocity plots [94] and transfer functions [97]; the elliptic trajectories drawn by the tips of the malleus handle and the stapedial head [16].

2.4 Discussion on the literature survey

2.4.1 Discussion on auditory canal survey

A general agreement on AC modeling arises from the survey. Many FE models of the human ear include the AC, with a general agreement on materials, element type and boundary conditions.

The geometry of the AC shows relevant inter-subject differences, although a range for a typical human adult subject can be identified.

An accurate study on the AC morphology can help in understanding the impact of noise on ears with different AC morphologies. Moreover, a sensitivity study on size and shape can help in reconstructive surgery.

2.4.2 Discussion on tympanic membrane survey

On the basis of a survey of the biomechanics of the TM, the relevant issues about the TM anatomy, structure and available experimental data have been firstly introduced. Then an overview of modeling approaches have been presented, mainly focusing on FE model features since in the last decades this technique has been extensively employed in hearing research.

Concerning the experimental characterization of the TM, several data are available on the geometry and anatomy, thanks to recent imaging techniques (e.g. μ-CT).

The thickness distribution still represents a critical issue since only few works in the literature actually measured this parameter in the human TM. The thickness choice strictly influences the material properties experimental characterization, since it is typically *a priori* assumed in data interpretation. Although some features on relative thickness distribution in different portions of the TM have been identified, absolute values of a typical human TM thickness distribution map are not still available; probably the age-related differences in thickness or pathologic alterations of available samples hinder the measurements. Even if histology and ultrastructure of the TM are deeply detailed by many authors, a standardization of techniques, trials and samples with the aim of material characterization does not yet exist, especially for orthotropic properties identification.

Most recent models still assume a uniform thickness, even if this parameter is considered highly significant on model results by many authors.

Another debated issue, highly significant on model outputs, is the AL constraint representation in the model, due to the complexity to represent the continuity between the TM fiber thickening, the fibrocartilaginous and the bony ring at the periphery of the TM with a lumped structure.

Despite the available knowledge on TM tissues and fiber arrangement the modeling of these features represents still an argued issue.

The high variability in design choices and modeling parameters, arising also in the wide range of result values, elucidates the necessity of further and standardized experimental activity for the TM characterization. Experimental investigations could be oriented towards the characterization of the most significant aspects, also in order to tune a patient-specific approach.

2.4.3 Discussion on ossicular chain survey

From the analysis of the state of the art concerning the ossicular chain modeling, reported above, two major issues arise: the wide dispersion of experimental data, which reflects the remarkable scattering of parameter values in modeling, and the choice of the most suitable investigation approach.

The dispersion of experimental data, affecting mainly the mechanical properties of soft tissues, can be attributed to the difficulties in testing such small elements and to the lack of a standardization of the experimental procedures. Moreover, although many authors [162] agree on the good correspondence between the *ex vivo* and *in vivo* measurement of mechanical properties, it is worth noting that most experimental activity is done on human or animal cadaveric samples and only few observations on some parts of the middle ear are done on living human beings [86]. Because of such a dispersion, parameter values are often tuned through a calibration procedure, as done in [15, 10, 97]. However, also model calibration are based on experimental curves, usually the umbo and the SFP displacement curves (measured with Laser Doppler Vibrometry [97, 93, 116]), that can markedly differ from author to author and show low repeatability even within a single experimental session. This can again produce a wide scattering of the calibrated parameters. It can be worth underlying that besides the model calibration procedure, the differences in displacement amplitudes between the simulated and the experimental curves are often remarkable, e.g. curves labeled Gan et al. 2009 (exp)/(sim) in Figs. 2.1 and 2.3. Although not much noticeable in the logarithmic scale, commonly adopted in output presentations, such differences can be even higher than 100-200%, underlying also the limits of current models.

As far as investigation approaches are concerned, the FE technique is employed in the quasi-totality of the recent studies for it can well represent the highly complex ossicle geometry and the TM material structure. On the contrary, the extremely simplified representation of the articulations certainly is one of the main limitations of the current FE models of the middle ear and maybe the cause of the above-mentioned discrepancy between simulated and experimental curves.

However, other modeling approaches (electro-acoustic or mechanical) are still pursued, because of their simplicity or improvement in the representation of joints. Till now no direct comparison has been made between the results of such types of models and the FE ones. The MB approach certainly involves some drawbacks, for example accounting of patient-specific geometries by means of a simplified scheme is not a direct and univocal procedure, while the FE approach allows a direct import from several imaging techniques (§2.3.2). However, a sensitivity analysis to geometric parameters is hindered by a complex geometry with respect to lumped parameters. Besides, the determination of inertia properties which highly influence the dynamic behavior of the ossicle, is complicated by the non-homogeneous densities of each ossicle, while in the MB approach it is simply expressed by means of the mass and inertia tensor [88] that can be tuned. Concerning material properties, the FE approach is capable to include viscoelastic and hyperelastic material models, although the small amplitude of the ossicle vibrations can justify a linearized analysis.

Chapter 3

Auditory Canal Model

The present chapter focuses on the TM and AC modeling, which are relevant components in the normal acoustic way and, precisely, in the outer and middle ear. The TM can be considered as either part of the outer or middle ear.

The problem was investigated considering two (fluid and structural) domains for the AC and the TM, respectively, in order to evaluate the coupling of different methods and to apply a fluid-structure interaction (FSI) formulation.

Standard finite element method (FEM) and wave methods, in particular Generalized Finite Element Method (GFEM), combination of standard FEM and Partition of Unity Method (PUFEM), were evaluated and applied, as detailed by the authors in [164]. The wave methods were selected as suitable to the modeling of sound propagation at high frequencies.

The analysis results, which include pressure distribution in the AC and displacement distribution and frequency response of the TM, confirm experimental and theoretical data proposed in the literature. The validation of the generalized methods with standard FEM simulation at increasing mesh density, show the computational advantages of these methods in terms of reduced required mesh density for a proper accuracy level of results.

3.1 Methods

As reviewed in [165], many physical systems in steady-state oscillation can be characterized using the Helmholtz equation. The acoustic lossless (i.e. viscous dissipation neglected) wave equation for propagation of sounds in a fluid is given by [133]:

$$\frac{1}{c^2}\frac{\partial^2 P}{\partial t^2} - \nabla^2 P = 0 \tag{3.1}$$

where c is the speed of sound in fluid medium, P is the acoustic pressure, and t represents time. Indicating with f the frequency, for harmonically varying pressure (i.e. $P = \bar{P}e^{j\omega t}$), where $\bar{P}$ is the pressure amplitude and $\omega = 2\pi f$, Eq. 3.1 reduces to the Helmholtz equation:

$$\frac{\omega^2}{c^2}\bar{P} + \nabla^2\bar{P} = 0 \tag{3.2}$$

Owing to the requirement of dense spatial discretization, the modeling of wave fields at high wave numbers is computationally demanding when standard, low-order polynomial finite element (FE) techniques are used. This presents one of the unsolved problems of the conventional FE method. The incorporation of the physical features of the solution into the approximation subspace represents an improvement for relaxing the mesh density of the FEM. This approach has been utilized for the Helmholtz problem by locally approximating the solution as a superposition of propagating plane waves or by enriching the polynomial FE basis function with the plane waves [165].

The methods proposed in the literature for the high frequency problems (i.e. when the wave length is lower than or comparable to the domain size) can be distinguished in Spectral Element Methods (SEM or SFE), based on Fast Fourier Transform (FFT) [166] or orthogonal polynomials [167], and Wave Element Methods (WEM) (e.g. Ultra Weak Variational Formulation, UVWF [165], the Partition of Unity Method, PUM or PUFEM [168], and the Generalized Finite Element Method, GFEM [169, 170]).

In the present study, FE models (*Ansys*®) of the TM and the AC, in anatomic geometries, Fig. 3.1a, were developed. Moreover, the GFEM [169] was applied to a simplified geometry of the AC-TM complex, Fig.3.1b-c. The GFEM method was validated at low frequency with respect to the FE results.

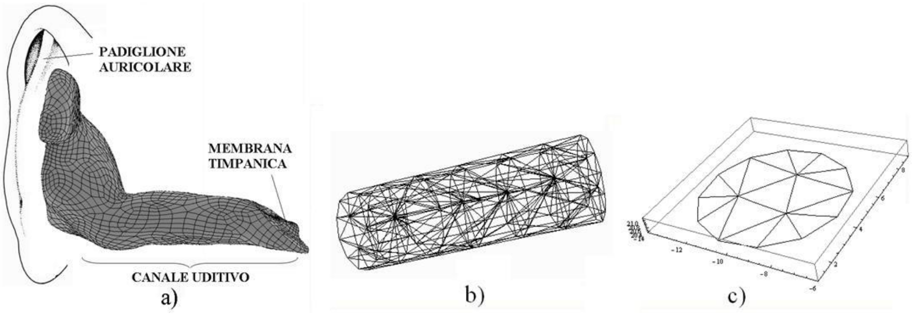

Figure 3.1: Anatomic (a) and simplified (b,c) auditory canal-tympanic membrane geometries.

3.1.1 Generalized finite element method (GFEM)

The generalized finite element method (GFEM) is a direct extension of FEM, which is a special case of GFEM, thus the boundary conditions can be imposed as in the FEM [169].

The GFEM is a combination of the standard FEM and the partition of unity method (PU(FE)M). The standard polynomial FE spaces are enriched with special functions (or *handbook* functions) reflecting the known information about the boundary value problem. The special functions are multiplied with the partition of unity corresponding to the standard FE linear or bilinear vertex "hat" shape functions and are pasted to the FE basis to construct a conforming approximation [169].

The local approximability is increased due to the handbook functions, while maintaining the existing infrastructures of the FE codes. In fact, the essential boundary conditions can be imposed in the GFEM exactly as in the standard FEM [169].

The generalized finite element space $S_{h,p}^{k,q}$ can be expressed as:

$$S_{h,p}^{k,q} = \left\{ u | u = \sum_{k=1}^{nfem} b_k N_k + \sum_{j=1}^{nnodes} \phi_i^{\Delta_h} (\sum_{j=1}^{q} a_j^{(i)} W_j^{(i)}) \right\} \tag{3.3}$$

where N_k denotes the standard bi-p hierarchical FE basis functions defined over the mesh Δ_h, p is the standard FE basis function degree on Δ_h, k is the wave number, q is the handbook function degree at each vertex of Δ_h, $\phi_i^{\Delta_h}$ are the bilinear basis functions corresponding to the mesh vertex i, $\{\phi_i\}_{i=1}^{nnodes}$ is the partition of unity employed in the pasting of the handbook functions for the conformity and $\{W_j^{(i)}\}_{j=1}^{q}$ are the handbook functions employed in the i^{th}

vertex. In the PU(FE)M, the first term in the sum in the right-hand side in Equ. 3.1.1 is not included.

The plane-wave, wave-band and Vekua handbook functions are evaluated in [170] for the GFEM applied to the Helmholtz problem solution concluding that they lead to equivalent results, although the employing of plane-wave functions involves a lower computational cost and ease of implementation without relevant variations in asymptotic accuracy for solving the Helmholtz problem, with respect to the more complex functions.

In the present study the plane-wave functions were adopted as handbook functions $\{W_j^{(i)}\}_{j=1,....,q}$; the more general expression is:

$$W_j^{(i)} = e^{i\boldsymbol{kr}} \tag{3.4}$$

In the 2D case the plane wave with direction vector $(cos(\theta_j), sin(\theta_j))$, where $\theta_j = \frac{2\pi j}{q}$ can be adopted as handbook functions:

$$W_j^{(i)} = e^{(ik((x-x_i)\cos\theta_j+(y-y_i)\sin\theta_j)}, \qquad j = 0, ..., q-1 \tag{3.5}$$

In the 3D case, as in the simulation of the fluid domain corresponding to the AC, an extension was required. In the 3D case the plane waves can be obtained in the following form [171]:

$$\begin{aligned} &W_j^{(i)} = e^{(ik(x\sin\theta_l\cos\phi_m+y\sin\theta_l sin\phi_m+z\cos\theta_l)}, \\ &\theta_l = l\frac{\pi}{p} \qquad l = 1, 2, ...p \\ &\phi_m = m\frac{2\pi}{q} \qquad m = 1, 2, ...q \end{aligned} \tag{3.6}$$

where θ_l and ϕ_m are the angles between the direction of propagation and two coordinate axes, following the classical spherical polar convention. Such a direct generalization of the 2D case, where only one angle is referred, restitutes a distribution of directions which are concentrated around the poles of an imaginary sphere. As stated in [171], it is impossible to obtain a perfectly equally-spaced distribution of directions.

In the below described implementation, the unit vectors of the propagation directions of the plane-wave functions in the 3D problems, were selected following the optimized "spherical covering" logic, borrowed from another method (e.g. Ultra Weak Variational Formulation, UWVF) [165].

The optimized "spherical covering" logic identifies n points (with n included in the 4-124 range, Fig. 3.2) on an imaginary sphere, centered in each mesh node, so that the maximum distance of each node belonging to the sphere from the nearest of the n considered points is minimized. Such a criterion allows to obtain a direction distribution as homogeneous as possible.

In the present study, the same number of directions was assigned to each node, although an equally-spaced distribution of directions and an equal number of degrees of freedom at each node are not required by the method; in fact, a different logic of selection of propagation directions, based on a priori knowledge about the solution, can allow reducing the number of directions required to obtain a given accuracy level.

As reported by many authors, an increasing number of wave directions involves a higher result accuracy with the drawback of introducing ill-conditioned system matrices and requiring dedicated integration techniques. Thus, it is often necessary to introduce in the implementation some checks on the condition number of the

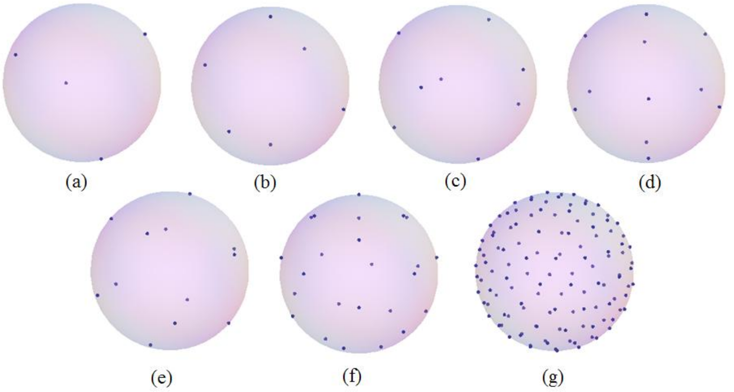

Figure 3.2: 4 (a), 6 (b), 8 (c), 11 (d), 12 (e), 24 (f) and 124 (g) points on a sphere, following the ”spherical covering” logic.

matrices and, if needed, to update the direction number assigned to each node.

A main issue in the implementation of GFEM is the possible linear (or almost linear) dependence between the added handbook and the standard basis FE functions [169].

3.1.2 Fluid structure interaction

The interfacing and coupling between different methods applied in partial domains of the whole model represents a relevant aspect including the debated issue of the fluid structure interactions (FSI) formulation.

The interaction of the fluid and the structure at the domain interface causes the acoustic pressure to exert a force on the structure an the structural motions produce an effective fluid load [134]. The introduction, in the system dynamics governing equations, of a coupling matrix accounting for the effective surface area and the normal to the interface area, represents a possible FSI formulation [134, 133].

In the present study, the FSI coupling formulation described in [133] was adopted at the interface between fluid and structural domains. Such a formulation involves the building of an asymmetric element matrix for the interface elements (typically fluid elements), which have the pressure (p_E) and three translational ($\boldsymbol{u}_E$) degrees of freedom. For the interface fluid element, the structural mass $[M_S]$, damping $[C_S]$ and stiffness $[K_S]$ matrices, as well as the fluid mass $[M_F]$, damping $[C_F]$ and stiffness $[K_F]$ matrices, assume the typical FE form. The total element matrices result:

$$\begin{pmatrix} [M_S] & 0 \\ [M_{FS}] & [M_F] \end{pmatrix} \begin{pmatrix} \ddot{\boldsymbol{u}}_E \\ \ddot{p}_E \end{pmatrix} + \begin{pmatrix} [C_S] & 0 \\ 0 & [C_F] \end{pmatrix} \begin{pmatrix} \dot{\boldsymbol{u}}_E \\ \dot{p}_E \end{pmatrix} + \tag{3.7}$$

$$+ \begin{pmatrix} [K_S] & [K_{FS}] \\ 0 & [K_F] \end{pmatrix} \begin{pmatrix} \boldsymbol{u}_E \\ p_E \end{pmatrix} = \begin{pmatrix} F_E \\ 0 \end{pmatrix} \tag{3.8}$$

where $[F_E]$ represents the pressure load, $[M_{FS}]$ and $[K_{FS}]$ indicate the coupling matrices, computed according to the following relations:

$$[M_{FS}] = \rho_0 [A]^T, \qquad [K_{FS}] = -[A] \tag{3.9}$$

where ρ_0 is the fluid density and the coupling matrix $[A]$ is obtained through the following integration on the interface surface S:

$$[A] = \int_S \{N\} \boldsymbol{n}^T \{N'\}^T dS \tag{3.10}$$

where $\{N\}$ and $\{N'\}$ represent the fluid and structural shape function matrices, respectively. The normal to the interface is indicated with $\boldsymbol{n}$.

3.1.3 Auditory canal analysis and modeling

Geometry

A standard geometry of human AC (including the air portion in the auricle), Fig. 3.3, was extracted through a semi-automatic segmentation algorithm, from computed tomography data (provided by the U.O. Otorinolaringoiatria 2° of the S. Chiara hospital in Pisa) and combined with the TM geometry, described in §4. Size and morphology of the reconstructed geometries was in the literature range for adult healthy subjects.

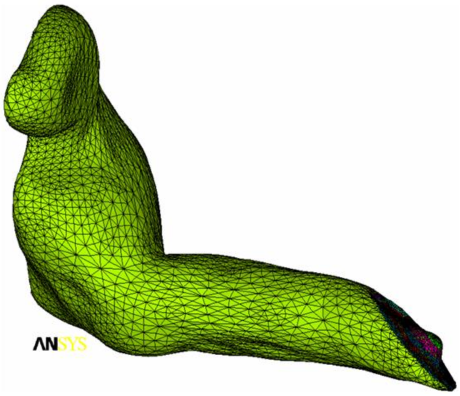

Figure 3.3: Auditory canal-tympanic membrane complex FE model.

To simulate the acoustic propagation in the AC-TM complex, spectral methods, based on orthogonal polynomials [167] and generalized FE methods (GFEM/PU(FE)M) [170, 169] were also evaluated, adopting plane waves as handbook functions.

The GFEM/PU(FE)M was applied to an approximately cylindric geometry (Fig. 3.1b-c), simulating the AC, closed at one end by a circular membrane, with the aim of facilitate the interface definition.

A fluid-structure interaction formulation (§3.1.2) was employed between the fluid domain (studied with GFEM/PU(FE)M) and the structural domain (TM, FEM), with asymmetric matrices.

Materials

The fluid in the AC was assumed as compressible, inviscid, with uniform mean density and pressure, with the typical values of the air medium (i.e. a 1.225 kg/m^3 density value and a 340 m/s speed of sound value).

Boundary conditions

The wall of the temporal bone was not included in the model and replaced by fully clamped boundary conditions at the interface, with a $\mu = 0.04$ value of adsorption coefficient of the wall.

A pressure load of 90 dB SPL was applied at the inlet of the AC, corresponding to 0.632 Pa.

Elements

Ansys® 3D acoustic elements (FLUID30) [133, 134] with fluid-structure interaction and a specific sound absorption coefficient at the interfaces with structural parts were employed to mesh the AC volume in the FE models.

In the present study, a mesh of about 69000 elements and 16000 nodes was adopted for the air in the AC, setting the FSI interaction for the fluid elements in contact with the TM elements. A coarse tetrahedral mesh with 224 elements and 94 nodes, was adopted to test the efficacy of the generalized method with respect to the standard one.

FE models with an increasing mesh density (i.e. element size (ESIZE) in the 0.5-4 range, corresponding to a node number between 183 and 8063 and an element number between 611 and 40802) were developed with the aim of validation of the GFEM models.

3.1.4 Tympanic membrane analysis and modeling

Geometry

The anatomic geometry of the TM was obtained as described in the following (§4), showing typical human adult size and morphology.

The combination of the TM and AC geometries caused size and shape changes lower than 1%. However, the FE simulation in *Ansys*® environment of the decoupled TM was repeated, applying the pressure load directly on the lateral surface of the membrane to check the uninfluence of the variations introduced by the image processing on results.

The circular geometry simulating the TM, adopted in the GFEM analysis, showed a radius equal to about the average between the elliptic axes.

Materials, boundary conditions and elements

The materials models reported by [15] were adopted, following an extended study on the TM, described in §4.

In all trials, the TM was fully clamped. When decoupled, a 90 dB SPL pressure load was applied on the lateral side of the TM.

Ansys® structural shell elements (SHELL63/93) with 6 degrees of freedom were adopted for the free mesh of the TM in FE models. Element size was selected through a convergence study on the first natural frequency, until a variation lower than 0.1%. About 1400 elements and 4000 nodes resulted, Fig. 3.4

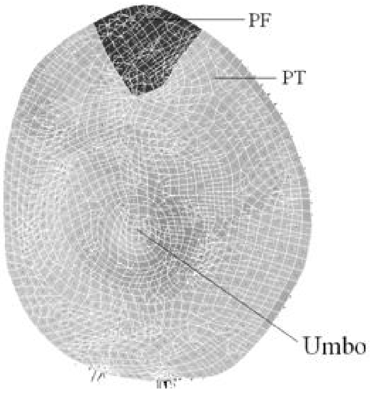

Figure 3.4: Tympanic membrane FE model.

3.1.5 Analysis types and outputs

Modal and harmonic analyses were developed in the *Ansys*® FE environment with the aim to evaluate the effects on the umbo displacement of adding the AC to the TM model. Frequencies in the 0-6000 Hz range were considered, with a 100 Hz step.

The umbo displacement in the ”piston-like” direction was selected as main output. The pressure distribution in the AC and the displacement distribution in the TM were also considered as FE results.

Modal and harmonic analyses were developed on the simplified geometries also in the GFEM models. The modal frequencies and shapes, as well as the displacement and pressure distributions in the structural and fluid domain, respectively, constitute the main implementation outputs.

3.2 Results and discussion

The inclusion of the AC to the decoupled TM model in the FE environment caused a decreasing of the frequency of the first resonant peak in the umbo displacement frequency response function and the arising of peaks in the 3-4 kHz range, often associated to the morphology of the AC in the literature [65, 128], Fig. 3.5.

As further outputs, the displacement and pressure distribution of the TM and in the AC, respectively, were selected, Fig. 3.6. The displacement distributions of the TM, as well as the modal frequencies of the system fall into the literature ranges. The pressure distribution in the AC results is analogous to the results of one of the main research group [15, 95] at 4 and 8 kHz frequencies. The values are not comparable due to the presence in the literature models of other ear parts.

Concerning the generalized methods, it was possible to validate the results at low frequencies by comparison with the FE results at increasing mesh refinement. A higher accuracy of the results with a coarse mesh was obtained, although further investigations

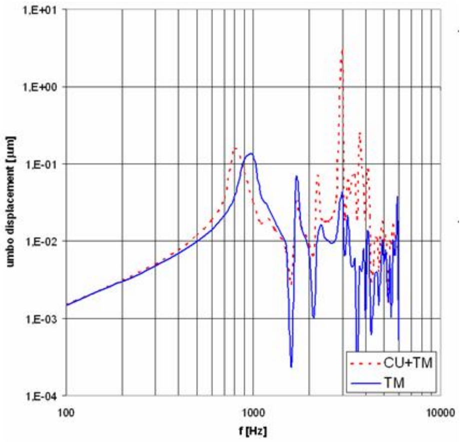

Figure 3.5: Umbo displacement in the decoupled TM and in the AC-TM models

are required.

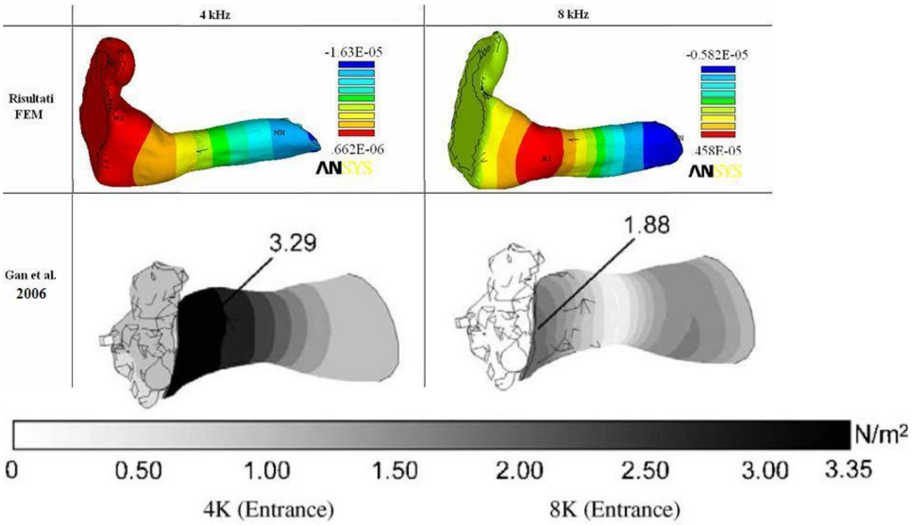

Figure 3.6: Pressure distribution in the AC: comparison between FE model and literature results [95]. (Reprinted from [95] with permission from Elsevier.)

Chapter 4

Tympanic Membrane Model

The human TM has a key role since it transfers sound waves into mechanical vibration from the ear canal into the middle ear. The changes in structure and mechanical properties of the TM due to middle ear diseases, such as the TM retraction, middle ear infection, otitis media with effusion, and perforation of the TM, can deteriorate sound transmission and cause conductive hearing loss [35]. An accurate model of the TM, which directly affects the acoustic-mechanical transmission, could improve the surgical reconstruction of damaged eardrums.

FEM is mostly applied to TM modeling for biomedical and clinical purposes. However in literature models with very different features (material models/parameters, boundary conditions, element type, etc.) can be found.

The TM anatomy and a brief summary of experimental investigations employed to characterize the TM mechanical properties and motion have been previously introduced in §1. Then an overview of modeling approaches was presented in §2, leading to a description of main features of FE models.

Eight selected reference studies were reproduced for a comparison carried out keeping fixed the TM geometry, except thickness, and decoupling it from other ear structures included in the original models. The results of the comparison and of a sensitivity analysis on one of the reference models are reported in the present chapter and in [161].

4.1 Comparison of literature finite element models

4.1.1 Outline of reference models

In this study, eight reference models, among the many cited, were selected for a comparison. Each of these models is at least a middle ear model, including the TM, the ossicular bones (and therefore incudomallear, incudostapedial and tympanostapedial joints) and the main ligaments.

FE models of the decoupled human TM were created in *Ansys*® trying to replicate the characteristics of the selected reference models in order to elucidate the influence of the main features on simulation results. A summary of the implemented models is reported in Tab. 4.1 supported by the main references for the design choices. The models have been sorted in increasing order of material model complexity. The missing parameters (not specified in the collected papers) were replaced with the most frequently mentioned values.

Label	Ref.	TCK (μm)	E (MPa)	G (MPa)	Damp.	CONSTR	CONSTR par.
Liu09	[66]	50	32	-	R(0,1e-4)	sa	E=0.6
Mik04	[91]	(75,200)	(40,20)	-	-	fc	-
Koi05	[101, 16, 102]	74	(33.4,11.1)	-	R(260,3.7e-5)	sp	(3e3,1.5e5,3e-5,1e-4)
Sun02	[97]	74	(32r20c,10)	-	R(0,1e-4)	sa	E=0.6
Gan06	[15, 95, 115]	74	(35r20c,10)	-	R(0,0.75e-4)	sa	E=0.6
Lee10	[98, 99, 100, 67]	100	(35r20c,10)	-	-	sa	E=60
Fer03pre	[10]	74	(36r30c,12.5)	93	-	fc	-
Fer03post	[10]	74	(4/1/0.9,0.9)	(0.8/0.9/9,-)	H(0.25,0.3)	sa	E=30,$\eta = 0.2$
Pre08	[64, 11, 65, 122]	(100,800)	(20/26.6/33.3/40/40r,10) (40/33.3/26.6/20/40c,10)	-	R(260,3.7e-5)	sp	kl=8.36e-4

Table 4.1: Implemented models. Legend: TCK=thickness, E=Young's modulus, G=Shear modulus, CONSTR=constraint representation, par.=parameters, fc=fully clamped, (PT,PF)=values for the PT and the PF respectively, (kls,kli,kts,kti)=longitudinal/torsional superior/inferior spring constants [N/m/m], [Nm/m], r=radial, c=circumpherential, sa=shell annulus, sp=springs, R(α,β)=Rayleigh damping, H(η)=hysteretic damping, η=loss factor, - =not specified.

Liu09

The FE model described in [66] is based on a complete set of CT images of a living human temporal bone and incorporates the ear canal, the middle ear suspensory ligaments and muscles, the middle ear cavity and the inner ear fluid. The TA is included in the model. A LE IS model, with a uniform thickness of 50 μm, is assumed for both the PT and the PF of the TM. Fluid-structural interfaces are defined on the surfaces of acoustic elements next to the movable structure, such as the TM, ossicles, and suspensory ligaments.

Mik04

Using an x-ray μ-CT of a human temporal bone, a middle ear model was developed in [91]. A LE IS model is proposed for the TM, with a uniform thickness of 75 μm and 200 μm for the PT and the PF, respectively. The TM was fixed around its entire circumference since the fibrocartilaginous ring not explicitly included in the model.

Koi05

In [101] a 3D FE model of the human middle ear with different depths of the conical shaped portion of the TM was developed, based on published data. The model described in [16] (mentioned and used in [102]) constitutes an improvement of previous models since includes the ligaments, tendons, middle ear cavities and external auditory meatus, the damping of the cochlea. More particular aspects, such as the TM thickness and constraints issues, and the attachment between the TM and the malleus, are reviewed and enhanced. A LE

IS material model is assumed for both the PT and the PF; a not uniform thickness distribution map was adopted, based on [21]. In all these studies, the boundary condition at the tympanic ring consists of linear and torsional springs, whose stiffness in the superior portion is assumed to be less than that in the inferior portion due to the lack of the tympanic ring in the superior potion.

Sun02

In [97] a geometric model of a human middle ear was constructed in a CAD environment from histological sections; a working FE model of the human middle ear was created using previously published material properties of middle ear components. Six ligaments and tendons are included and meshed with solid elements. Surrounding the TM periphery, the TA was modeled using shell elements, with a thickness assigned in accordance with the TM geometry of the CAD model. The TM is modeled as a LE shell structure with homogeneous and orthotropic material properties; the portion of AL which divides the eardrum into PT and PF, is assumed to have the same Young's modulus as the PT.

Gan06

A 3D finite element model (Fig. 4.1) of the human ear including the external ear canal, middle ear suspensory ligaments and muscles, and middle ear cavities and cochlear load, constructed based on a complete set of histological section images of a human temporal bone is proposed in [15]. The TA was modeled as elastic supports with shell elements, whose thickness is included in the range 50-100

μm, with a mean value of 74 μm. The PT and the PF of the TM are assumed as orthotropic and isotropic materials, respectively. In [95] the previous model is modified to include acoustic-structural interfaces for coupled analysis from the ear canal through the TM to the middle ear cavity. The extension consists in considering the acoustic-structural-acoustic coupling effect of the ear canal-TM and ossicles-middle ear cavity, passing from the “one-chamber” to the “two-chamber” (ear canal and middle ear cavity) simulation.

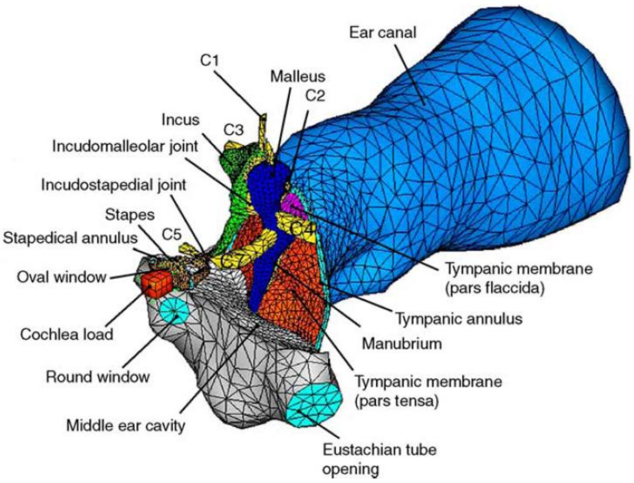

Figure 4.1: FE model, described in [95] (reprinted from [95] with permission from Elsevier).

Lee10

High-resolution computed tomography of temporal bone was performed in order to construct an FE model including tendons and muscles [98, 99, 100]. The PT of the TM was modeled as a solid element structure with homogenous and orthotropic material properties, while the PF is assumed isotropic. A uniform thickness of 100 μm was adopted in the model. The periphery of the TM is assumed to be connected to the bony wall of the ear canal through an elastic ring.

This model is extended in [67] and a three-chamber (ear canal, middle ear, and mastoid cavity) FE model of the right ear is developed, incorporating the external ear canal, middle ear cavity, and mastoid cavity.

Fer03pre and Fer03post

A mathematical model of the middle ear, based on μ-CT technique for the geometry importation, is detailed in the dissertation [10]. A relevant aspect of this work relies on the model validation issue, performed by means of an iterative fitting process in order to identify the model parameters. As a matter of fact [10] concluded that the variable conditions and the limitation of the measurement technique itself certainly affects the efficiency of the fitting procedure used to identify model parameters, which is strictly dependent on the number of involved parameters and on the comparison criteria. Moreover, concerning the physical meaning of the estimated parameters, the same author remarks the impossibility to know whether the identified set of parameter values let a FE model behave like a mean normal middle ear or like an extremal normal one since slightly different characteristics and qualities of normal ears exist.

Orthotropic and isotropic material models are assumed for the PT and the PF respectively and confirmed by the identification procedure. In the model, the TM is considered to be attached to the sulcus into the bony tympanic ring through the AL, so that the displacement of the TM at the ring is zero.

A preliminary set of parameters, deduced by [10] from the literature, and the estimated parameters, resulted from the fitting procedure, are assumed in the **Fer03pre** and **Fer03post** implemented models, respectively.

Pre08

The 3D FE model described in [64] includes the outer ear canal. A five part orthotropic PT and an isotropic PF of the TM are assumed; a varying thickness, taken from [137], was adopted. This model is improved in [11]. An FE model, based on μ-CT and nuclear magnetic resonance imaging, is developed and employed in [65, 122]. This model includes the ear canal, five ligaments (the anterior ligament of the malleus, the lateral ligament of the malleus, the posterior ligament of the incus, the superior ligament of the malleus, and the superior ligament of the incus) and two muscles (the tensor tympani muscle and the stapedius muscle). A varying thickness with a maximum of 800 μm in the PF and a minimum of 100 μm in the PT is adopted in [65]. Thickness measurements from [19] are employed in [122]. In all these works, the periphery of the TM is restrained against radial motion and springs are employed, along the longitudinal direction, to replicate the flexible connection.

4.1.2 Analysis and modeling

Geometry

The geometry of the TM was deduced from an anatomic model, available on line (`http://audilab.bmed.mcgill.ca/~daren/3Dear`), obtained by means of magnetic resonance imaging (MRI) of human cadaveric temporal bones. Its dimensions (Fig. 4.2) result in the mean range of human values (elliptic major and minor axis of about 9 mm and 8 mm respectively, cone depth of about 1.46 mm).

A default uniform thickness of 0.074 mm was assumed for both PT and PF [15] when not otherwise specified.

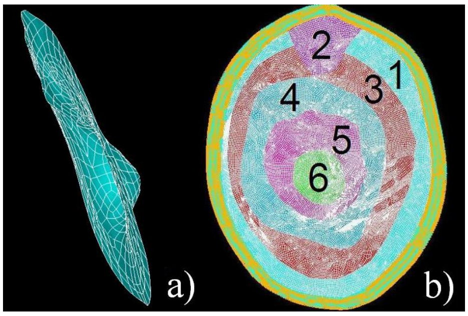

Figure 4.2: (a) Tympanic membrane FE model; (b) six pars in the TM.

Material models

Linear elastic material models definition required the identification of different regions in the TM. Six regions have been identified in the TM geometry (Fig. 4.2b), based on published measurement data, in order to isolate the PF and distinguish the PT in five zones, as described in [64], eventually fused in an homogeneous region depending on the adopted material model.

Young's moduli, Poisson's ratios and densities are required parameters. In order to include orthotropic properties, local coordinate systems have been introduced. Since most of the authors refers to radial and circumferential Young's moduli, a reference cylindrical coordinate system, centered in the umbo of the TM, was defined. All element coordinate systems were aligned with the umbo coordinate system. Shear moduli only appear explicitly in orthotropic models where they are independent of transverse Young's moduli. When required and not alternatively specified, the shear modulus (G_{XY}) was assumed [172] as

$$G_{XY} = \frac{\sqrt{E_X E_Y}}{2(1 + \sqrt{(p_{xy} p_{yx})})} \tag{4.1}$$

where E_X and E_Y represent the Young's moduli in the radial and circumferential direction respectively, p_{xy} and p_{yx} represent the Poisson's ratio in the major and minor formulation, related by the following

$$p_{yx} = \frac{E_Y}{E_X} p_{xy} \tag{4.2}$$

A default $1.2 \cdot 10^3$ kg/m^3 density value was assumed in all implemented models except in **Fer03post** [10] reference model where a $1.0 \cdot 10^3$ kg/m^3 density value was specified.

A default 0.3 Poisson's ratio value was assumed, except in **Fer03pre** [10] (where 0.4 and 0.3 values are specified for the PT and the PF, respectively) and **Fer03post** [10] reference models (where 0.4/0.1/0.1

values in the radial, circumferential and thickness directions are specified for the PT and a 0.3 value for the PF).

Material damping was included when specified in the reference study. Mainly Rayleigh damping is employed. α [s^{-1}] and β [s] coefficient are reported in Tab. 4.1. Hysteretic damping loss factors η, assumed in [10], are also reported. The loss factor, used to quantify the level of hysteretic damping of a material, was related to the damping ratio ζ so viscous damping models were used for analysis. At resonance it results $\eta = 2\zeta$.

Boundary conditions

Mainly three constraint representations were implemented in order to replicate the conditions described in the mentioned works: a fully clamped periphery, a shell annulus or a spring restraint at the periphery of the TM. It's worth noting that the choice of considering the whole TM to be rigidly attached to the tympanic ring around its entire circumference, represents an approximation of the TM anatomy, since the fibers of the TM extend around the periphery of the PT, forming the AL, that is a fibrous thickening firmly attached to a sulcus in the bony tympanic ring, except superiorly where it separates the PT from the PF [8].

An annular shell structure, extending around the whole periphery of the TM and constrained at the outer boundary was introduced in the models where the presence of the AL was deduced. A 0.22 mm width, a 0.2 mm thickness, a $1.2 \cdot 10^3$ kg/m^3 density value and a 0.6 MPa Young's modulus have been assumed, where not otherwise specified.

As an alternative to directly model the TA, a longitudinal (and sometimes torsional) spring restraint was adopted when specified in the corresponding reference model. The TM has been constrained by means of linear springs in the longitudinal direction ("piston-like" direction of the ossicles chain and drums) and sometimes also torsional springs (the *Ansys*® COMBIN14 element as in [11]). All other degrees of freedom has been forced to zero displacement and rotation. Differentiated elastic constants in the inferior or in the superior portion (representing the "notch of Rivinus") of the TM periphery were specified when indicated by the authors. Values of $3.0 \cdot 10^3$ N/mm and $1.5 \cdot 10^5$ N/mm for the linear spring constants and values of $3.0 \cdot 10^{-5}$ Nm/m and 10^{-4} Nm/m for the torsional spring constants have been assumed for the superior and inferior portion of the tympanic ring respectively, referring to [101, 16]. Alternatively the spring constant value was assigned to each spring element considering a total stiffness per unit length of $8.36 \cdot 10^4$ N/m^2 and a TM radius of 4.8 mm, referring to [64].

Sound pressure stimulus of 90 dB SPL was applied as a uniform surface load on all elements on the lateral side of the TM.

Mesh, analysis types and outputs

A free quadrilateral mesh (Fig. 4.2) of *Ansys*® SHELL93/63 elements was employed in all models. A convergence analysis based on first undamped natural frequency values was conducted reducing the mesh size until a variation inferior to 0.1% was obtained. Assuming this stopping condition, a mesh of 3032 elements and 9027 nodes was selected.

Modal and harmonic analysis were applied in the commercial FE simulation environment *Ansys®*. Undamped natural frequencies were recorded as main modal analysis result. The displacement of the node corresponding to the umbo location, evaluated in the 0−6000 Hz frequency range with a step of 100 Hz, was recorded as main output of the harmonic analysis.

4.1.3 Results

In this section modal and harmonic analysis results of the implemented models are reported. As already stressed, each model consists in a decoupled TM, since other parts of the ear are not modeled, and the obtained results can differ from those reported by the original authors.

Modal analysis

Modal results in terms of the first twenty undamped natural frequencies for all models are compared in Fig. 4.3; the first three are reported in Tab. 4.2.

It can be observed that the first natural frequency approximately results in the 0.9-1.5 kHz range for all models, except for the **Fer03post** reference model that gives a 247 kHz value of the first natural frequency. It is interesting to underline that the initial parameter values, used in **Fer03pre**, give the highest frequency values in Fig. 4.3, while values obtained after fitting lead to the lowest ones. A lower first frequency (about 600-650 kHz) with respect to the mentioned range results also in **Liu09**, **Sun02**, **Gan06** reference models, which give very similar values for the first three modal frequencies, despite the different thickness and material model.

A different combination of parameters results in similar modal frequencies in **Liu09** and **Sun02** reference models. The damping and the boundary conditions at the periphery being equal, a different material model (IS and homogeneous for the whole TM in the former, OR in the PT and IS in the PF, and therefore non-homogeneous, in the latter) and a different thickness result in a similar behaviour concerning the first twenty resonance frequencies.

As a general observation, a fully clamped or spring restrained (with the used values of stiffness constants) TM, proposed by **Mik04**, **Koi05**, **Fer03pre** and **Pre08**, result in a higher first resonance frequency with respect to the shell annulus structure proposed by **Liu09**, **Sun02**, **Gan06**, **Lee10** and **Fer03post**. The next frequencies (Tab. 4.2) show a similar trend and dependence on the parameters. However **Lee10** model shows several analogies with **Mik04**, **Fer03pre**, **Koi05** and **Pre08**, on the basis of modal results and, particularly, of the third resonant frequency (Fig. 4.3 and Tab. 4.2); the high values of the first three resonance frequencies could be related to the fact that **Lee10** model shares a similar constraint, since the periphery of the TM is constrained by a high-stiffness annulus.

If the modal frequencies are assumed as the most relevant output of analysis, it appears that a simpler model, as material formulation and boundary conditions, can be sufficient to reproduce the physiological TM behaviour.

Harmonic analysis

Harmonic analysis results of most models of the literature consist in an umbo displacement frequency response curve, whose features and values are validated by experimental trials. The results of harmonic analysis for each implemented model, performed in the 0−6000 Hz frequency range with a step of 100 Hz are reported in Fig. 4.4.

As already stressed, a wide spread of experimental data is available in the literature. The obtained values show a good agreement as order of magnitude and curve trend with respect to the curves deduced from published results (and overlapped in Fig. 1.6) for all models, except for **Fer03post**, for the same reasons reported in 4.1.3. Despite the first resonance is commonly evident in most models, the TM frequency response at low frequencies does not result as flat as reported by most authors and the behavior at high frequency shows a lot of variability, confirming the necessity of further experimental investigations in these frequency ranges, due to their importance for hearing.

On the basis of harmonic results (Tab. 4.2), analogies can be found between model behaviors. Considering both resonances and maximum value of the umbo displacement, **Liu09**, **Sun02** and **Gan06** reference models (Fig. 4.4), may form a first group. The **Mik04**, **Fer03pre**, **Pre08** and **Lee10** reference models can be classified as a second group, on the basis of the resonance peak frequency. The **Koi05** reference model shows an intermediate behavior between the two above mentioned groups concerning the first three resonant peaks frequencies, while the umbo displacement trend and peak amplitude are similar to those obtained for **Sun02** model. Here again

Label	Ref.	1^{st} f	2^{nd} f	3^{rd} f	UD_{Max}, f
Liu09	[66]	645	828	1167	0.135, 600
Mik04	[91]	1130	1419	1886	0.366, 1100
Koi05	[101, 16, 102]	893	1090	1665	0.104, 900
Sun02	[97]	606	818	1207	0.107, 600
Gan06	[15, 95, 115]	614	833	1228	0.137, 600
Lee10	[98, 99, 100, 67]	977	1246	1812	0.762, 3200
Fer03pre	[10]	1103	1442	2157	3.03, 1100
Fer03post	[10]	247	316	450	0.25, 300
Pre08	[64, 11, 65, 122]	1102	1698	1935	0.0472, 1100

Table 4.2: Model result comparison in terms of first three frequencies (f [Hz]) and the maximum absolute umbo displacement (UD [μm]) value at f frequency.

the boundary conditions at the TM periphery appear crucial in result variations, while the assumption of an OR-IS or a mean-value uniform IS-IS material model for PT and PF seems not to be of great influence on results.

Despite a similar first resonance frequency, the umbo displacement trends of the **Mik04**, **Fer03pre**, **Pre08** and **Lee10** show significative differences in the peak amplitude values, related to the inclusion/neglecting of material damping. It is worth noting that, even if the higher displacement value is recorded at 3200 Hz for **Lee10** model, a local maximum of $3.57 \cdot 10^{-1}$ μm appears at 1000 Hz, according to the other models.

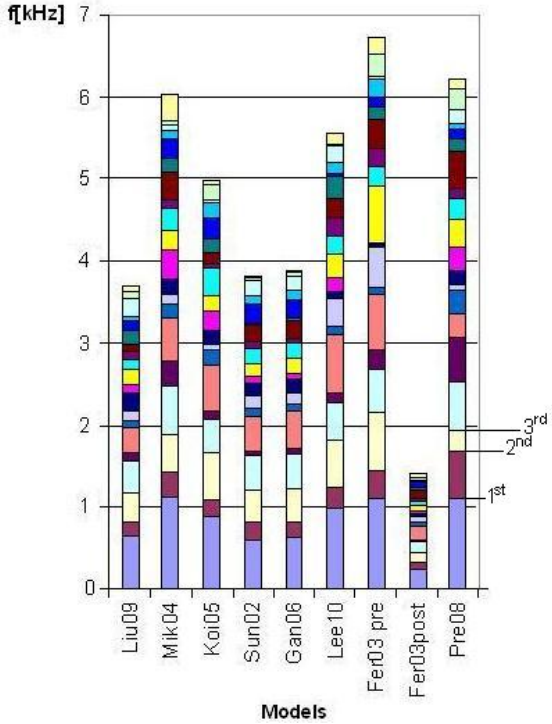

Figure 4.3: Bar diagram of the first 20 natural frequencies for the material models reported in Tab. 4.1. The bar height corresponds to the frequency value (Hz). See Tab. 4.2 for references of model labels.

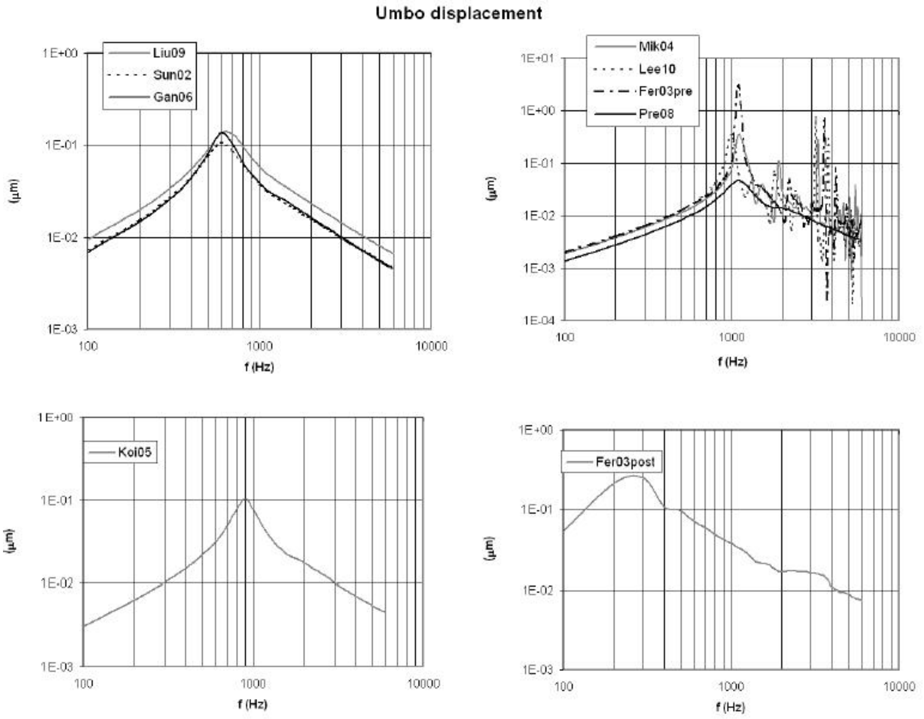

Figure 4.4: Umbo displacement (μm) for the implemented models. See Tab. 4.2 for references of model labels.

4.2 Sensitivity analysis

From the comparison of modal and harmonic results, the model sensitivity to the parameters arises, allowing to infer that the thickness and the constraint features could be the most influent aspects in TM modeling, while the complexity of the material model and the choice of material parameter values appear less influent.

A sensitivity analysis was carried out [173], as a useful tool to identify the parameters with the highest influence on model results. A probabilistic approach was adopted, assuming one of the previously introduced reference models [15, 95] as base model. A uniform distribution of input parameters was assumes, deducing the parameter ranges from the examined literature.

As outputs, the first twenty modal frequencies were analyzed..

4.2.1 Input variables

The input variables consisted of the TM geometric, inertial and material parameters. In details, the TM geometry was varied in terms of size, cone depth and thickness. Size and cone depth variations were obtained through a radial and a linear scale factor, respectively.

Thicknesses of the PT and PF was varied as independent variables with a uniform distribution. Concerning the inertial properties, only the homogeneous density value of the whole TM was varied. The TM material model was varied in terms of Young's and shear modulus, Poisson's ratio and Rayleigh damping parameters. Distinct Young's moduli and Poisson's ratios for the PT and PF were considered.

The influence of the shell annulus, representing the tympanic annulus and annular ligament which anchor the TM at the periphery, was evaluated varying its features in terms of geometry (width and thickness) and material properties (Young's modulus).

4.2.2 Results

As first result, the statistics of the results were analyzed for varying of the above mentioned variables in the assigned ranges.

The first modal frequency resulted in the 700-1500 Hz range for all trials, as widely accepted in the literature.

The most significant parameters consisted of the size scale factor and density, the thickness and Poisson's ratio of the PT and the shell annulus geometry.

Less influent resulted the cone depth scale factor, the PF thickness and the material properties of the PF and shell annulus.

4.3 Discussion

Eight reference models have been compared keeping the geometry and the loading fixed, and decoupling the TM from other ear structures included in the original models.

Concerning the critical issues arising in the modeling step, as previously mentioned in 2, most recent models still assume a uniform thickness, even if this parameter is considered highly significant on model results by many authors, as confirmed also by some preliminary trials made by our group in order to better clarify the importance of lacking or non-specified parameters.

Another debated issue, highly significant on model outputs, is the AL constraint representation in the model. Moreover, despite the available knowledge on TM tissues and fiber arrangement, the modeling of these features represents still an argued issue.

The results show that the complexity of the material model and the choice of material parameter values is less influent with respect to the constraint representation, as assumed in the *a posteriori* classification of reference models based on similar results.

Modal and harmonic results confirmed published assertions on the TM behavior. From the comparison of results, it can be inferred that the constraint feature is the most influent feature in TM modeling. However the fundamental importance of the combination of geometric and material parameters arises from the comparison of the modal and harmonic results of the implemented models, making the definition of an optimal model complicated.

Due to the high variability in design choices and modeling parameters, a sensitivity analysis is a useful tool to identify the parameters with the highest influence on model results.

Chapter 5

Ossicular Chain Model

This chapter is focused on the human middle ear behavior, following a previous investigation on the AC and the TM [161], described in §4. From the description of the middle ear anatomical features (§1) and the detailed model-oriented review of this part (§2) stressing the most significant assumptions and issues, an original 3D multi-body (MB) model of the OC is proposed in the present chapter and in [174].

The MB approach was preferred in this study to the most widespread finite element method (e.g. [15, 95]), for its main advantage of being a lumped parameter approach. Thus it simplifies the model elements definition (body, joints, ligaments etc.) by taking into account only the characteristics that affect the system dynamic behavior. The model was used in particular to investigate the debated issue of the mobility allowed at the incudo-malleolar joint. Simulation results indicate that such a model achieves a good accuracy, moreover with a low computational cost.

5.1 Methods: a multibody model

In order to investigate debated aspects, on the basis of ascertained data and not including unnecessary assumptions, a simple but accurate 3D lumped parameter model of the OC was developed in the *SimMechanics* environment (*Matlab*®, *MathWorks*, *Massachussetts*, USA).

The model structure was based (although with some significant modifications) on the doctoral thesis and other studies of T. Wright [88], while, when available, model parameters were deduced from [15, 95]. Wright's model [88] was selected from the literature since he reported most parameters, allowing reproducing his work; however, improvements were made in modeling the IMJ and also by including the LML, the SML and the TT and ST tendons.

It was assumed that the ossicles behave as rigid bodies and that tissues have a linear visco-elastic response; the synovial joints were described as smooth ideal mechanical couples. The main elements of the developed lumped parameter model (shown in Fig. 5.1) are:

- four rigid bodies representing the ossicles (the manubrium and the head of the malleus are modeled separately) and the lumped cochlear load mass;
- ideal joints to simulate the IMJ, the ISJ but also the connections at the ends of the OC (TMMJ and SOWJ);
- spring and damper elements to represent the actions of soft tissues (tendons, ligaments, joint capsule); in particular six elements link the ossicles to the ground, representing the AML,

LML, SML, PIL, TT and ST, while other five elements act at the TMMJ, IMJ, ISJ and SOWJ.

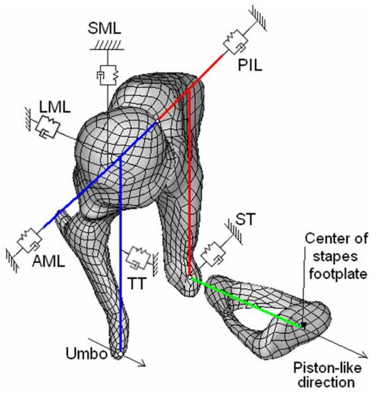

Figure 5.1: Geometric scheme of the model

Our model differs from Wright's one [88] in the following details:

- the masses, which in Wright's model represented the TM, the ear cavities and the TM suspension equivalent masses, respectively, are omitted in the model because it is aimed at reproducing the mechanical behavior of just the OC and not of the whole middle ear. Only the cochlear load mass is left;
- the LML, SML and the two tendons of the TT and the ST muscles, not included in Wright's model, are added, instead, to the model as spring and damper lumped blocks in order to improve the simulation of the actual behavior.

Nerves were not considered.

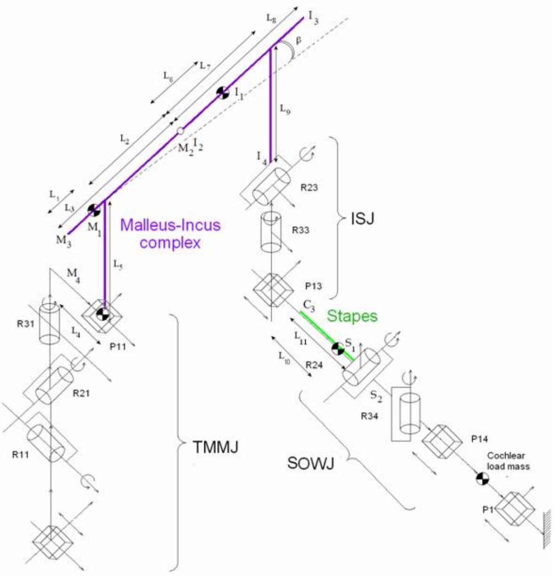

Figure 5.2: Robotic-like diagram of the joints with 0 Dof IMJ

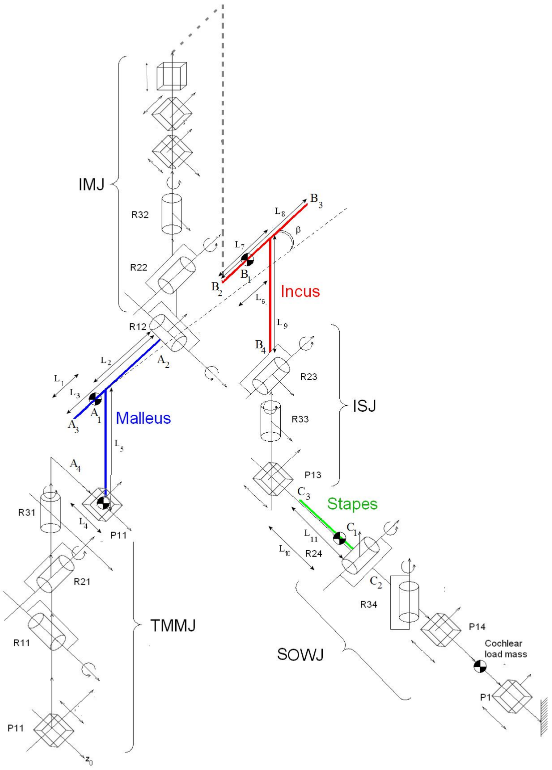

Figure 5.3: Robotic-like diagram of the joints with 6 Dof IMJ

In our study two different configurations of the model were developed, with moveable or fixed IMJ in order to better simulate the behavior of such a joint.

5.1.1 Basic model geometry

As far as OC geometry is concerned, according to Wright's model [88], the main points of the malleus, incus and stapes are indicated with the letters M, I and S, respectively (Fig. 5.2 and Fig. 5.3). M_1, I_1 and S_1 denote the centers of mass. M_2 denotes the IMJ (coincident with I_2, point on the incus), M_3 the point at which the AML is attached to the malleus, M_4 the umbo, considered as the effective attachment point (umbo) of the manubrium to the TM, I_3 the point of attachment of the PIL to the incus, I_4 the ISJ location on the incus, respectively. The ISJ enables a relative motion in both rotational and translational modes so the location of the joint on the stapes (denoted as S_3) does not in general coincide with I_4, accounting for some rotational components around the short and long axes of the SFP, described in [175]. Unlike in Wright's model, in our model the IMJ has relative motion in translation too, according to experimental evidences in [68, 69]. Point S_2 on the stapes coincides with the geometrical centre of the SFP. Points M_4 and S_3 are confined to move on parallel lines, in the "piston-like direction" of the OC. A γ angle [88] was introduced as a geometric parameter that represents the inclination defining the AML-PIL ligament axis.

Inertia tensor ($mg \cdot mm^2$)			
	Malleus	Incus	Stapes
I_{11}	107.8	66.86	1.731
I_{22}	85.49	75.76	4.839
I_{33}	50.73	29.16	6.219
I_{12}	-4.570	6.045	0.4008
I_{13}	33.14	-0.2815	0.0464
I_{23}	12.07	4.095	-0.0111

Table 5.1: Inertia tensors of the ossicles from [88].

5.1.2 Component definition

Ossicle chain

Ossicle data (location of the center of mass and inertia tensor) were deduced from Wright's studies [88] (Tab. 5.1).

Since a dispersion of mass values exists, mainly concerning the stapes, due to the biological variability, the mass values of [15] were preferred.

A critical issue was the definition of ideal mechanical joints to represent the behavior of the much more complex natural articulations. A robotic-like scheme (Fig. 5.2 and Fig. 5.3) can help the comprehension of the adopted solutions:

- TMMJ: two prismatic (P) joints and a spherical (S) one, defined as three revolute joints. One of the prismatic and the spherical primitives represent the TMMJ connection, while the other prismatic joint lays in the piston-like direction, assumed as the only possible movement direction for the umbo;
- IMJ: a weld or a 6 DoF joint;
- ISJ and SOWJ: a prismatic and two revolute joints, with the

joint axes oriented in the same way;

- a prismatic primitive in the piston-like direction limits the cochlear load mass movement with respect to the ground.

The prismatic primitive in the IMJ and ISJ allowed a limited physiological dislocation/ interpenetration of the ossicles in the articulation in physiological working conditions, controlled by means of linear and torsional spring and damper elements. Parameters for the linear elements, were partially deduced from [157] while an order of magnitude of the torsional and bending constants were estimated as initial values to be tuned in an optimization procedure, knowing the Young's moduli, the Rayleigh [s] coefficient, an average gap and the area of contact of each articulation.

Other structures

Spring and damper elements were also introduced to represent ligament (AML, LML, SML, PIL) and tendon (TT, ST) actions, not included in the robotic-like scheme. The location of the ligaments and the muscle tendons was estimated from textbooks of anatomy. Geometric parameters, concerning the ligaments and tendons, absent in Wright's model, were deduced from other authors. In particular, ligaments were assumed 0.8 mm long and 0.5 mm × 0.5 mm. The TT muscle was taken as 3 mm long and 0.5 mm × 0.5 mm in cross-section, while the stapedial muscle was taken to be 2 mm long and 0.43 mm × 0.46 mm in cross-section as in [65, 98]. The material properties (Young's modulus, density) of ligaments and tendons were mainly deduced from [15, 95]. The Young's modulus E and the β Rayleigh coefficient were used to estimate an order of magnitude of the elastic and the damping constants, for linear, torsional and bending behavior, according to the classic beam theory. The widespread range of literature Young's modulus values suggested an optimization procedure in order to estimate suitable parameters and calibrate the model.

As a noticeable aspect, it is worth noting that the cochlear load was explicitly modeled as a mass-spring-damper system, instead of a mass-damper system as in [15] in order to account for the omitted SAL action.

5.1.3 Model implementation

A *SimMechanics* machine (Fig. 5.4) was built and tuned in order to simulate the dynamics of the human OC. Two variants with 0 and 6 DoFs in the IMJ were tested.

The machine environment and the simulation configuration parameters were set in order to carry out a 3D forward dynamic analysis, in absence of gravity. A linear state space model of the system around an operating point was defined, in order to check the model stability by monitoring the system poles.

The *SimMechanics* graphic components depicting the model convex hulls and inertia ellipsoids are shown in Fig. 5.5.

5.1.4 Parameter identification procedure

The values of umbo and SFP displacement (peak-to-peak amplitude and phase angle) assumed as input and reference signals, respec-

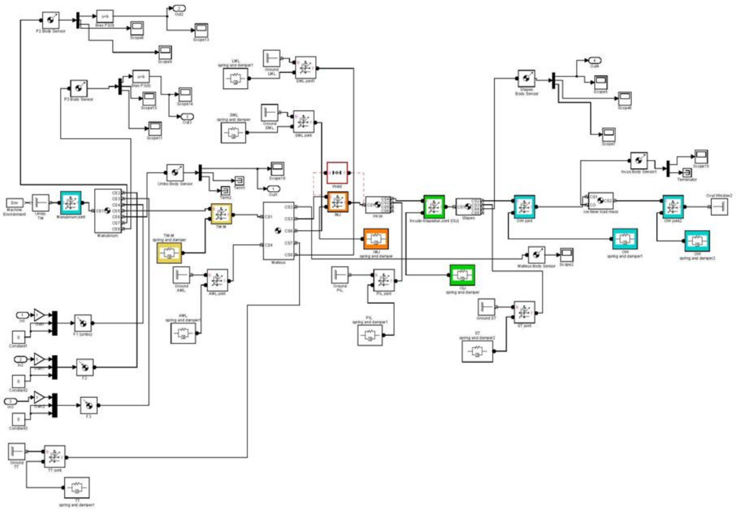

Figure 5.4: *SimMechanics* machine

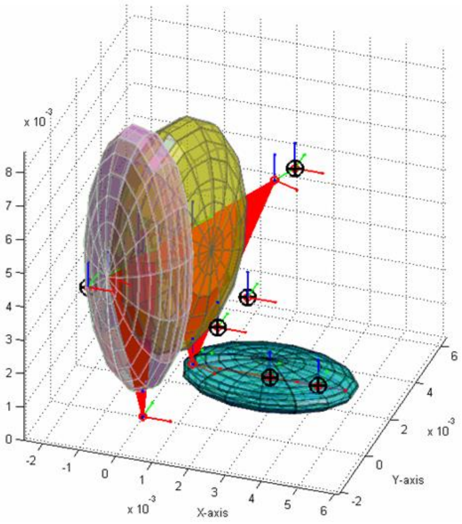

Figure 5.5: *SimMechanics* graphics: convex hulls and ellipsoids

tively, for the parameter identification procedure were taken from published numerical and experimental data [93]. The phase angle values were expressed as phase differences with respect to the input pressure on the TM, which causes the umbo displacement. The umbo displacement amplitude and phase angle reference curves are reported in §2, respectively, with the label Gan et al. 2009 (exp)/(num).

An optimization procedure was developed in order to identify unspecified parameters but also to tune some parameters whose literature values range within different orders of magnitude [14], as done also in [15, 10, 97].

In [15, 97] a cross-calibration procedure based on the minimization of the differences between the numerical and experimental SFP mean peak to peak displacements, in the 250 Hz- 8 kHz range at 90 dB SPL of input pressure at the TM, is employed to derive four undetermined elastic and damper constants; in [10] an iterative fitting procedure with 87 parameters, based on trial and error principle and on a fitting on partial models, is reported.

In this work, as objective function, the sum of the relative errors between the obtained and the desired SFP displacement amplitude and phase angle at 58 logarithmically spaced frequencies in the 0.3-6 kHz range was assumed.

The minimization problem was solved in *Matlab*® by means of two different optimization approaches: a constrained nonlinear local and a global (Direct [176]) algorithm. In both cases, lower and upper boundaries for each variable were defined as 75% of an ascertained literature or estimated value. In addition, the local minimization approach required a suitable set of initial values; they were chosen from the literature, preferably from [93].

Parameter calibration was carried out to fit the two model versions (0/6 DoFs at the IMJ) both on numerical (NUM) and experimental (EXP) reference curves, by means of local (LOC) and global (GLO) optimization algorithms. Moreover, in order to take into account the higher human sensitivity in the 1-5 kHz frequency range, the calibration procedure was repeated introducing the A-weighting curve [5]. Further investigations considered a parameter identification based only on the amplitude (and not on the phase angle) and a double calibration splitting the frequency range in two (<1 kHz, >1 kHz) and considering 58 logarithmically spaced frequencies in each range.

It is worth noting that the calibration procedure is very complex due to the high number of parameters to identify and criteria which must be fulfilled by a set of values, so that the identified set of parameters must be considered as acceptable and not as the absolute best set. The choice of the ranges for each parameter is also a critical issue, since the existence of a set of values out of the boundaries can not be excluded.

The MB model is characterized by a huge number of geometrical, inertial and material parameters. In order to reduce the computational burden of the calibration procedure, only those whose values were most widespread in the literature, were selected for tuning. A parameter vector was defined, with 11 and 19 components for the 0/6 DoF IMJ model version, respectively, including the translational elastic and damping constants of the TMMJ, ISJ (in the piston-like direction) and of the AML, PIL (in their main line of action), the damping constants of the ST and SOWJ in the piston-like direction, the γ angle and, in the 6 DoF IMJ version, all the translational and rotational elastic and damping constants of the IMJ; for symmetry in the articulation anatomy, the IMJ constants were assumed equal in the piston-like and in the vertical directions.

	0-GLO-NUM	6-LOC-NUM	6-GLO-NUM
Amplitude (RMS)	0.175	0.115	0.113
Phase angle (RMS)	0.105	0.091	0.080
Sum	0.280	0.206	0.194

Table 5.2: RMS values of cumulative errors (all over the frequency range) of stapes displacement amplitude and phase angle and their sum, with respect to the numerical reference curve.

5.2 Results

5.2.1 Model calibration

As results of the optimization procedures, the obtained SFP displacement amplitude and phase angle, fitted on numerical and experimental curves [93], are shown in Fig. 5.6 and Fig. 5.8, respectively.

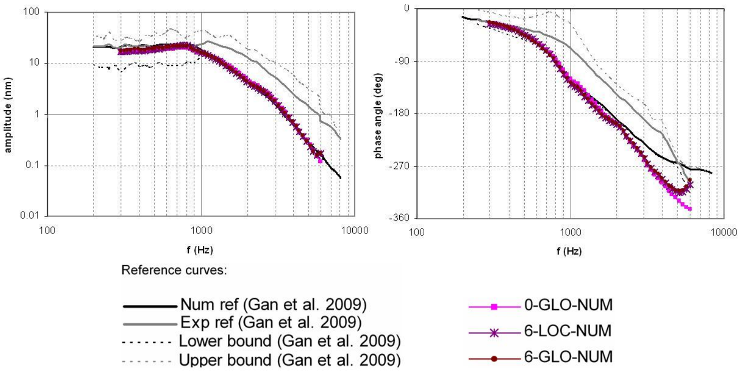

Figure 5.6: Stapes displacement amplitude and phase angle curves with respect to the numerical reference curve.

Upper and a lower boundaries of literature experimental data deduced from [93] are also reported; the width of such curves confirms

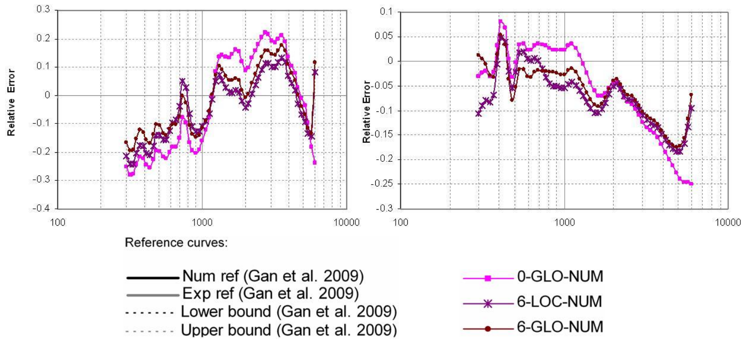

Figure 5.7: Relative errors on stapes displacement amplitude and phase angle curves with respect to the numerical reference curve.

the wide scattering of experimental data, partially hidden by the logarithmic scale.

The proposed MB model was initially fitted on the numerical reference curve since many data were taken accordingly to the corresponding FE model. From Fig. 5.6 it can be observed that both model versions (0/6 DoF at the IMJ) reproduce satisfactorily the stapes displacement amplitudes. In order to better compare models and approaches, the amplitude and phase angle relative errors are also shown in Fig. 5.7 and Tab. 5.2. All over the frequency range the amplitude error remains almost within -30 to +22%.

On the other side, the trend of the stapes displacement phase angle, underestimated with respect to the reference curve at high frequency, shows lower errors (from -25 to +10%.). It can be observed that the 6 DoF model seems able fit numerical reference curves, especially the amplitude one, better than the 0 DoF version, that is with a Root Mean Square (RMS) amplitude error of about 11% vs. 17%.

It can be worth noting that the raising trend at high frequencies of the phase angle reference numerical curve [93], is absent in the experimental results. This allows inferring that our results show an acceptable trend, although a slightly more pronounced loss in phase angle appears at increasing frequency with respect to the experimental trend.

The comparison on the optimization method (LOC/GLO), reported only for the 6 DoF model for brevity, indicates that there are no meaningful differences on results, the RMS error being comparable in the two approaches. I

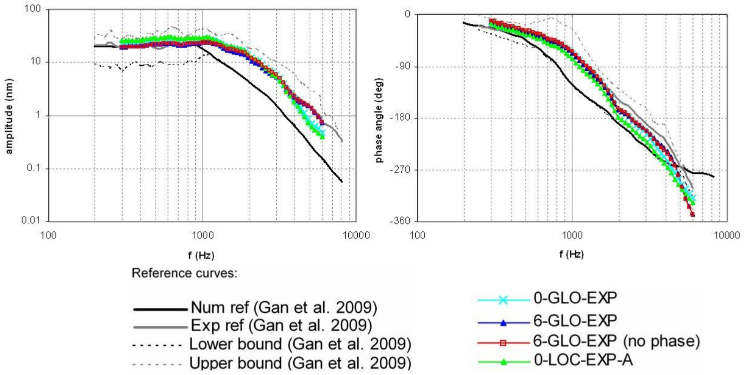

Figure 5.8: Stapes displacement amplitude and phase angle curves with respect to the experimental reference curve.

The model calibration on the experimental data (Fig. 5.8 and Fig. 5.9, Tab. 5.3) was less satisfactory than the former, giving higher errors both on amplitude (approximately within -60 to +60%) and phase angle (from -21 to 60%). In particular an initial offset on amplitude at low frequencies (< 1 kHz) can be observed for all the simulations. The phase angle relative error is higher at low frequen-

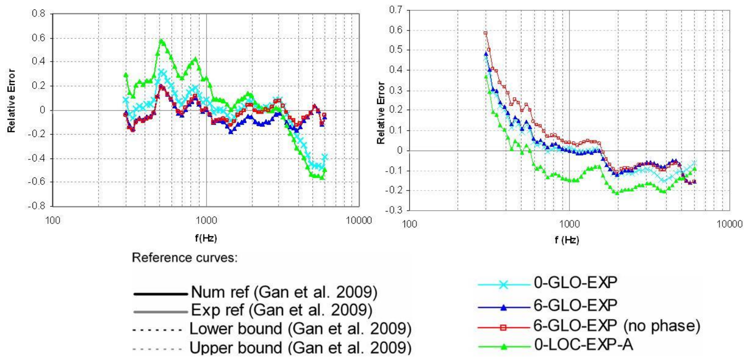

Figure 5.9: Relative errors on stapes displacement amplitude and phase angle curves with respect to the experimental reference curve.

	0-GLO-EXP	6-GLO-EXP	6-GLO-EXP (no phase angle)	0-LOC-EXP-A
Amplitude (RMS)	0.183	0.096	0.080	0.299
Phase angle (RMS)	0.134	0.136	0.179	0.152
Sum	0.316	0.232	0.258	0.450

Table 5.3: RMS values of cumulative errors (all over the frequency range) of stapes displacement amplitude and phase angle and their sum, with respect to the experimental reference curve.

cies, about 0.4-0.6; however it can be observed that this means an absolute error below 15 deg. Also in this case the 6 DoF-GLO behaved better than the others, as confirmed by the RMS error.

Comparing our results with the numerical reference curve, it can be remarked that the proposed MB model is able to fit the experimental data better than the corresponding FE model described in [93].

The addition of the A-weighting function for the calibration on experimental data, increased the RMS errors both on amplitude and phase angle, mainly at the boundaries of the frequency range, as expected. The lowest amplitude error (8%) was obviously obtained neglecting the phase angle error in the objective function (6-GLO-EXP (No Phase)); moreover a limited error on the phase angle, comparable to the other cases, was obtained.

Since some studies distinguish the behavior of the IMJ as showing 0 or 6 DoF at low (< 1 kHz) or high frequencies (> 1 kHz) respectively, a double calibration procedure was performed on two partial ranges (< 1 kHz, > 1 kHz).

Results, reported in Fig. 5.10 and Fig. 5.11, indicate that the calibration on limited ranges is more satisfactory, as confirmed by the lower RMS errors (Tab. 5.4). While at low frequency (< 1 kHz) both the 0 and the 6 DoF models gave similar results, above 1 kHz the latter was able to better fit the experimental curve, giving a lower error (0.16 vs. 0.294) particularly on amplitude (0.093 vs. 0.199).

The parameter values obtained for the 6-GLO-EXP, fitted on the whole range and on the restricted ranges (< 1 kHz, > 1 kHz) cases, are reported, as an example, in Tab. 5.5.

All identified parameters fall strictly within the assigned ranges

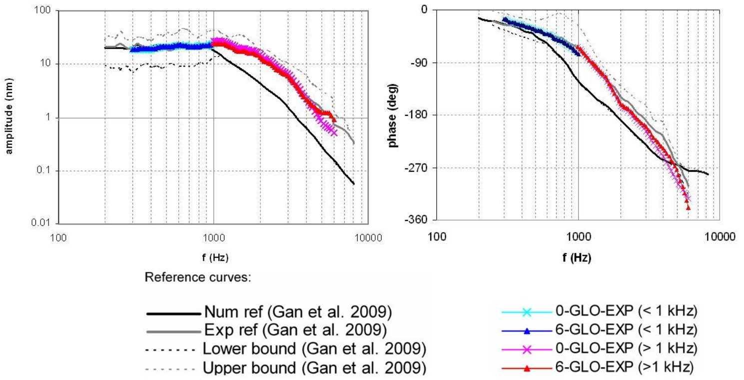

Figure 5.10: Stapes displacement amplitude and phase angle curves with respect to the experimental reference curve for a calibration procedure on partial (<1 kHz, >1 kHz) frequency ranges.

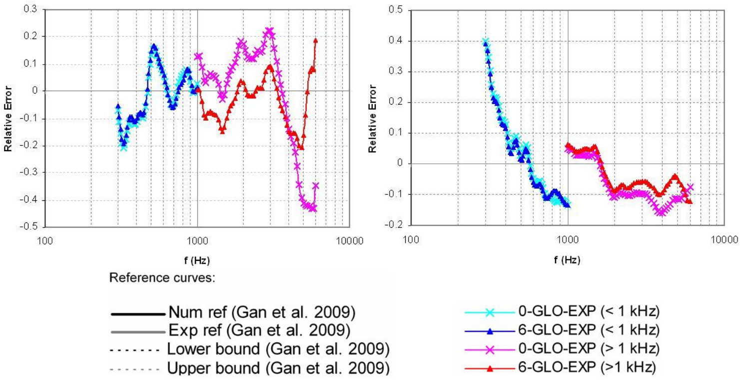

Figure 5.11: Relative errors on stapes displacement amplitude and phase angle curves with respect to the experimental reference curve for a calibration procedure on partial (<1 kHz, >1 kHz) frequency ranges.

	0-GLO-EXP (< 1 kHz)	6-GLO-EXP (< 1 kHz)	0-GLO-EXP (> 1 kHz)	6-GLO-EXP (> 1 kHz)
Amplitude (RMS)	0.097	0.094	0.199	0.093
Phase angle (RMS)	0.145	0.138	0.095	0.067
Sum	0.242	0.232	0.294	0.160

Table 5.4: RMS values of cumulative errors (all over the frequency range) of stapes displacement amplitude and phase angle and their sum, with respect to the experimental reference curve, for a calibration procedure on partial (< 1 kHz, > 1 kHz) frequency ranges..

(not on the boundaries) and in most cases tend to take on the upper boundary values. The γ angle and the stapedius translational damper constant in the AML-PIL direction remain unchanged in all three shown cases.

Comparing the identified parameters for the three cases, it can be noted that parameters mainly change without a recognizable trend. As far as the IMJ is concerned, the lowest values of all rotational spring and damper constants are identified in the > 1 kHz case, while a general trend is not evident in the resulting translational constant values.

To complete the description of the calibration procedures, it should be added that each calibration took about 5-6 hours, while a simple dynamic simulation of the OC just few seconds.

Parameter	Optimization parameters				
	6-GLO-EXP	6-GLO-EXP (< 1 kHz)	6-GLO-EXP (> 1 kHz)	Lower bound	Upper bound
ISJ transl. spring constant (N/m) (piston-like direction)	$1.141 \cdot 10^3$	$1.141 \cdot 10^3$	$1.027 \cdot 10^3$	$1.712 \cdot 10^2$	$1.199 \cdot 10^3$
TMMJ transl. spring constant (N/m) (piston-like direction)	$1.590 \cdot 10^3$	$7.95 \cdot 10^2$	$1.590 \cdot 10^3$	$3.975 \cdot 10^2$	$2.782 \cdot 10^3$
AML transl. spring constant (N/m) (AML-PIL direction)	$2.430 \cdot 10^3$	$8.102 \cdot 10^2$	$4.051 \cdot 10^3$	$6.067 \cdot 10^2$	$4.253 \cdot 10^3$
PIL transl. spring constant (N/m) (AML-PIL direction)	$1.472 \cdot 10^4$	$8.836 \cdot 10^3$	$1.473 \cdot 10^4$	$2.209 \cdot 10^3$	$1.546 \cdot 10^4$
ISJ transl. damper constant (N·s/m) (piston-like direction)	$3.00 \cdot 10^{-2}$	$2.569 \cdot 10^{-2}$	$1.284 \cdot 10^{-2}$	$6.422 \cdot 10^{-3}$	$4.495 \cdot 10^{-2}$
TMMJ transl. damper constant (N·s/m) (piston-like direction)	$5.300 \cdot 10^{-2}$	$1.987 \cdot 10^{-2}$	$1.325 \cdot 10^{-2}$	$9.937 \cdot 10^{-3}$	$6.956 \cdot 10^{-2}$
AML transl. damper constant (N·s/m) (AML-PIL direction)	1.367	$8.658 \cdot 10^{-1}$	1.367	$2.051 \cdot 10^{-1}$	1.435
PIL transl. damper constant (N·s/m) (AML-PIL direction)	$8.280 \cdot 10^{-1}$	$5.522 \cdot 10^{-}1$	$9.204 \cdot 10^{-1}$	$1.381 \cdot 10^{-1}$	$9.664 \cdot 10^{-1}$
ST transl. damper constant (N·s/m) (AML-PIL direction)	$5.592 \cdot 10$	$5.593 \cdot 10$	$5.593 \cdot 10$	8.389	$5.872 \cdot 10$
SOWJ transl. damper constant (N·s/m) (piston-like direction)	$1.330 \cdot 10^{-2}$	$1.000 \cdot 10^{-2}$	$3.333 \cdot 10^{-3}$	$2.500 \cdot 10^{-3}$	$1.750 \cdot 10^{-2}$
IMJ transl. spring constant (N/m) (piston-like and vertical directions)	$2.666 \cdot 10^4$	$1.111 \cdot 10^4$	$3.333 \cdot 10^4$	$1.000 \cdot 10^4$	$7.000 \cdot 10^4$
IMJ transl. spring constant (N/m) (AML-PIL direction)	$7.583 \cdot 10^4$	$7.583 \cdot 10^4$	$3.792 \cdot 10^4$	$1.137 \cdot 10^4$	$7.962 \cdot 10^4$
IMJ rotat. spring constant (N·m) (piston-like and vertical directions)	2.059	3.084	2.056	$5.139 \cdot 10^{-1}$	3.598
IMJ rotat. spring constant (N·m) (AML-PIL direction)	5.139	3.426	1.713	$8.566 \cdot 10^{-1}$	5.996
IMJ transl. damper constant (N·s/m) (piston-like and vertical directions)	$1.250 \cdot 10^{-1}$	$2.500 \cdot 10^{-1}$	$1.667 \cdot 10^{-1}$	$6.250 \cdot 10^{-2}$	$4.375 \cdot 10^{-1}$
IMJ transl. damper constant (N·s/m) (AML-PIL direction)	$1.300 \cdot 10$	8.667	$2.600 \cdot 10$	6.500	$4.550 \cdot 10$
IMJ rotat. damper constant (N·s·m) (piston-like and vertical directions)	$1.160 \cdot 10^{-2}$	$1.153 \cdot 10^{-2}$	$7.709 \cdot 10^{-3}$	$1.927 \cdot 10^{-3}$	$1.349 \cdot 10^{-2}$
IMJ rotat. damper constant (N·s·m) (AML-PIL direction)	$1.500 \cdot 10^{-2}$	$1.499 \cdot 10^{-2}$	$1.285 \cdot 10^{-2}$	$3.212 \cdot 10^{-3}$	$2.248 \cdot 10^{-2}$
γ (deg)	$2.210 \cdot 10$	$2.210 \cdot 10$	$2.210 \cdot 10$	5.525	$3.867 \cdot 10$

Table 5.5: Optimization parameters obtained in the 6-GLO-EXP case.

5.2.2 AML-PIL axis

On the calibrated models, further attention was focused on other important features of the middle ear, as the motion of the AML and PIL axis in the 0 DoF IMJ version. For this purpose the M_3 and I_3 points of connection of the AML and PIL to the malleus and the incus, respectively, were monitored in the steady state since they represent the ends of the identified axis in the fixed-axis hypothesis.

A precession of this axis is evident from the elliptic curves drawn by the two ends, reported in Fig. 5.12. Therefore, simulations showed a changing rotation axis (even at low frequency, having assumed a single-fused malleus-incus complex), due to the compliance of the ligamentous structures, according to [77]. However, the size of the ellipses is negligible, supporting the fixed-axis assumption.

The distance between the AML and PIL locations has been scaled for visualization purposes in Fig. 5.12, due to the extremely reduced size of the precession trajectories.

5.2.3 Instantaneous axis of motion of the malleus-incus complex

The instantaneous screw axis of motion of the malleus-incus complex was computed in the 0 DoF IMJ model version, as done in [11, 177] and overlapped on the model structure in Fig. 5.13.

The instantaneous distance and the angle between the central axis and the AML-PIL axis were also evaluated; the mean and maximum values in the steady state are reported in Fig. 5.13. While at low frequency (600 Hz) the central axis is almost horizontal and co-

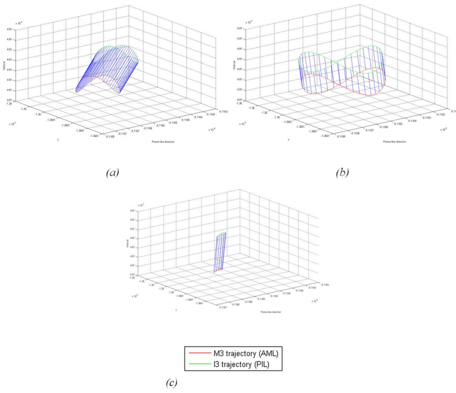

(a) (b)

(c)

Figure 5.12: Elliptic curves drawn by the AML and PIL connections to the ossicles in the 0 DoFs IMJ model at 600 (a), 1000 (b) and 3000 (c) Hz.

	Distance mean value (mm)	Distance max value (mm)	Angle mean value (deg)	Angle max value (deg)
600 Hz	$4.543{\cdot}10^{-1}$	1.443	89.8	175.5
1000 Hz	$6.055{\cdot}10^{-1}$	1.467	90.4	174.7
3000 Hz	$7.321{\cdot}10^{-1}$	1.588	86.1	178.4

Table 5.6: Distance and angle between the AML-PIL and screw axes on the model structure at 600, 1000 and 3000 Hz.

incident with the AML-PIL for most of the time in the steady state, at higher frequencies (1000, 3000 Hz) the axis tends to rotate and become vertical.

5.2.4 Relative motion at the IMJ

The six relative motion components of the IMJ, in the 6 DoF IMJ model version, were also monitored in the steady state conditions as a quality check. Values in the 0.01-10 nm range were obtained for linear displacement components in the piston-like, AML-PIL and

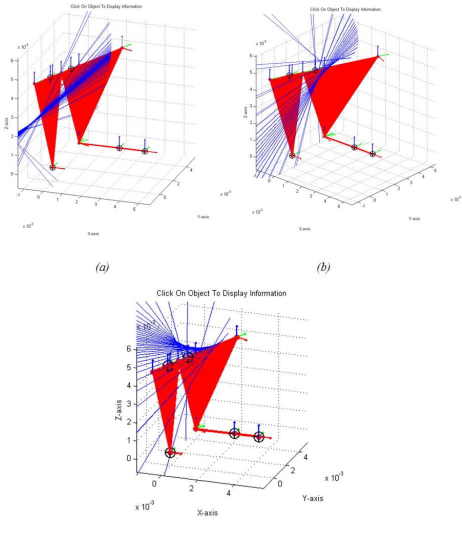

(a) (b)

(c)

Figure 5.13: Distance and angle between the AML-PIL and screw axes on the model structure at 600 (a), 1000 (b) and 3000 (c) Hz.

vertical directions.

5.3 Discussion

In this chapter a MB model was proposed, which eases the computational aspect and allows improving the joint behavior as ideal mechanical joints. The simulation and prediction of the OC behavior was focused on some issues related to the IMJ mobility, came up from the literature survey. At this purpose two versions of the model were developed assigning 0 or 6 DoFs to the IMJ.

A calibration procedure was applied to tune uncertain parameters, in particular those whose values were found the most scattered in the survey. With respect to the literature, where details on the model calibration are rarely reported, the present study deepens also that aspect, specifying the objective function, identified parameters and making a comparison between a local optimization algorithm and a global one. The first method requires initial guess values, which can have an influence on the solution; on the other side the global optimization needs only the definition of boundaries for the parameters and in this sense could be more reliable. However, no significant differences were noticed in the results obtained with the different optimization algorithms.

The proposed MB model succeeded in satisfactorily replicating both experimental and numerical reference SFP displacements [93], even with a better response compared to the reference FE model. To explain this particularity, it is worth noting that the differences between our model and the reference one, mainly regard the joint and cochlear modeling. In [93] the IMJ is modeled as a bone-like layer between the malleus and the incus (0 DoF), while the TMMJ and ISJ are modeled as portions of elastic tissues with mechanical properties taken from [15, 95]. In our model ideal mechanical joints were used with spring and damper elements characterized by means of a calibration procedure. Moreover in [93] an uncoiled cochlea was modeled, while we assumed a mass and damper cochlear load as in [15].

Our results showed lower amplitude and phase angle RMS errors for the numerical curve than for the experimental one. The 6 DoF IMJ version of the model performed better than the 0 DoF one, showing a lower error. In particular, as highlighted by a separate calibration on two restricted frequency ranges (< 1 kHz, > 1 kHz), the main differences between the two model versions arise at high frequency, the 6 DoF attaining an error around 16% versus a 30% error of the 0 DoF model. On the other side, at low frequencies the error is almost the same (24%). These comparative results suggest improvement of joint modeling as a way to enhance FE model performance.

It is interesting to underline that neglecting the phase angle error in the objective function gave the lowest error in amplitude ($\sim$ 8%) maintaining a satisfactory approximation of the phase angle curve with an average error comparable to the other cases (17.9% vs. 13.6%). The introduction of an A-weighted objective function resulted in a higher error, mainly at the boundaries of the frequency range.

On the calibrated models, further attention was focused on other important features of the middle ear. The AML-PIL axis displacement was observed in the 0 DoF IMJ version, both at low and high frequencies, describing an elliptic precession trajectory, although of very small amplitude. The instantaneous screw axis of motion was also computed and the distance and angle between this axis and the AML-PIL axis were monitored.

Due to its simplicity, physical foundations and good performance, the proposed MB model may represent a convenient and effective tool to quickly assess the benefits and risks of middle ear interventions and implants or to estimate the consequences of pathologies In fact, the main mechanical damages which influence the OC mobility (e.g. fixation or disruption) can be associated with a variation of the geometrical and/or the mechanical properties of the structures, and can be simulated by simply changing model parameters [178, 102, 116, 66].

As future developments, the introduction of other parts of the ear in the model will be pursued. A more accurate cochlear load estimation, as well as a more realistic representation of the complex connection between the TM and the malleus, certainly could improve the present model in finding more meaningful parameters, directly correlated to physical quantities and measurable variables. For this purpose a hybrid modeling approach, coupling an MB model of the OC and a FE model of the TM, could help overcoming some concerns affecting the middle ear simulation [179, 180], as described in the following chapter.

Chapter 6

Hybrid middle ear model

The middle ear models in the literature are typically defined either in a FE or in a MB environment. As detailed in §4, the FE method is capable of representing the complex geometry and the material orthotropy of the TM. On the contrary, a multi-body approach can be adopted for the OC (§5).

In this section, a complete middle ear model is presented combining the FE model of the TM, described in §4, with the MB model of the 6 DoF IMJ version of the OC model, described in §5. The hybrid FE/MB modeling approach was pursued through a feedback control strategy. Model parameters were estimated (in a first study [180]) through a calibration procedure with the aim of reproducing ascertained experimental literature data [93] in terms of umbo (reference point of connection between the malleus and the TM) and stapes footplate centre displacements.

The sensitivity of the calibrated model to both TM and OC parameters was investigated. Material, geometrical and inertial parameters were considered, in particular those whose values are most widespread in the literature.

6.1 Model components

6.1.1 Tympanic membrane finite element model

Th FE model of the human TM as isolated from the middle ear system, Fig. 6.1 was deduced as detailed by the authors in §4.

Thicknesses and material properties were deduced from [93, 15, 95] which developed a FE model of the middle ear, in order to replicate the characteristics and the numerical/experimental results of this reference research group. Briefly, the PT and the PF of the TM are assumed as orthotropic (with a 35 MPa and a 20 MPa values of the Young's moduli in the radial and circumferential directions, respectively) and isotropic materials (with a 10 MPa Young's module), respectively.

The TA was modeled with shell elements, whose thickness has a value of 200 m. Differing from [161], a rigid region is defined, corresponding to the insertion of the manubrium of the malleus into the TM.

Simulations were carried out in *Ansys*® 11. A study of convergence, based on the first frequency above 20 kHz, was performed to set the element size.

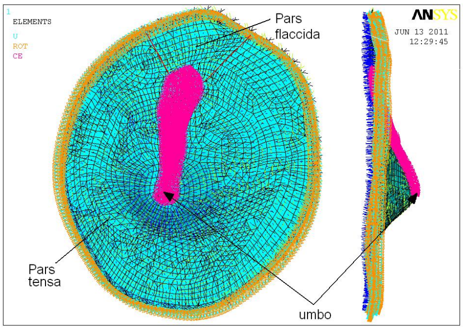

Figure 6.1: Finite element model of the tympanic membrane. The rigid region corresponding to the malleus insertion is highlighted.

6.1.2 Ossicular chain multibody model

In a previous study [180] two different configurations of the model were developed, with moveable or fixed IMJ. In this study the 6 DoF IMJ configuration of the MB model, described in §5, was adopted since it showed to better reproduce experimental results.

6.2 Hybrid FE/MB middle ear model

Combining the previously described models of the TM and the OC, an hybrid FE/MB model of the complete middle ear was developed.

A feedback control strategy was adopted to dynamically solve the contact problem between the TM and the OC, Fig. 6.2. Such an approach allows an automatic estimation of reaction forces and torques between the TM and the OC, which are internal actions and, then, not easily measurable; no data on these forces are available, as far as our knowledge is concerned.

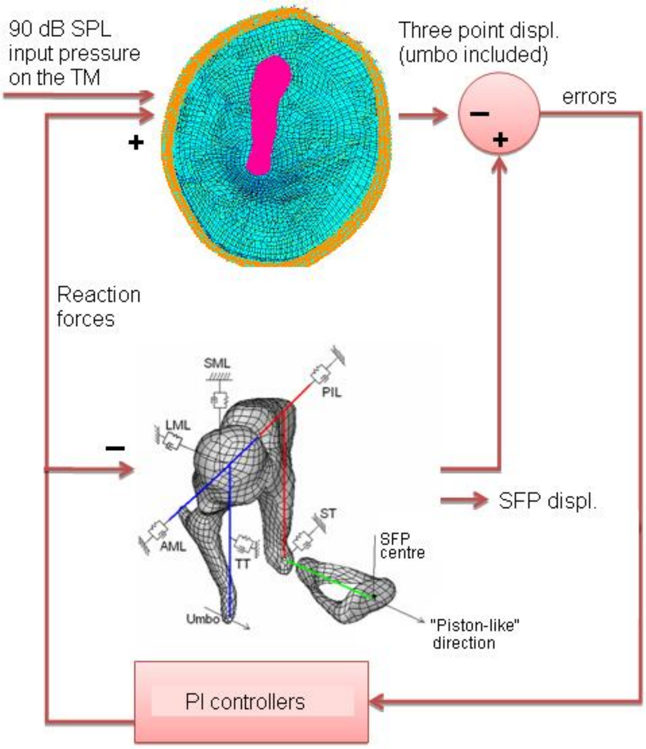

Figure 6.2: Scheme of the complete middle ear model.

The eigenvalue results from the FE model were used to develop a state space model of the TM, as described for a simpler problem in [181]. The number and location of master DoFs and the number of modes required were assigned in order to obtain consistent results between the FE and the state space model. Moreover, through linearization, about an equilibrium point, of the block diagram, a state space linear model of the OC was obtained.

A 90 dB sound pressure level sinusoidal pressure input was applied to the TM. The outputs include three parallel reaction forces between TM and OC on three misaligned points of the rigid region (umbo included), the umbo and SFP displacement, and the residual errors at the steady state.

Three proportional-integral controllers were introduced. Three error functions are provided as inputs to the controllers. Each error function is computed as the difference between the current displacement value, estimated by the model, and the reference one, deduced from the literature [93], of each mentioned point. The gain values were tuned in order to have an error dynamics faster than the system dynamics.

6.2.1 Parameter identification procedure

The values of umbo and SFP displacement (peak-to-peak amplitude) assumed as reference signals for the parameter identification procedure were taken from published experimental data [93].

As done for the OC model and described in §5, an optimization procedure was developed in order to identify unspecified parameters but also to tune some parameters whose literature values range over orders of magnitude, as detailed in [180].

6.2.2 Sensitivity analysis

A sensitivity analysis was carried out varying the TM FE model and the OC MB model parameters, each at a time with respect to the identified ones. The umbo and SFP displacement curves were monitored. Concerning the TM model, the selected parameters were:

- the thicknesses of the PT, PF and of the TA;

Parameter	Lower bound	Upper bound	Identified
TM thickness (μm)-PT	50	100	74
TM thickness (μm)-PF	50	800	74
TA thickness (μm)	50	200	200
TM Young's mod. (MPa)-PT-rad.	20	85.7	35
TM Young's mod. (MPa)-PT-circ.	20	60	20
TM Young's mod. (MPa)-PF-isot.	10	32	10
TA Young's mod. (MPa)-isot.	0.6	60	0.6

Table 6.1: Literature boundaries for sensitivity parameters of the tympanic membrane model.

- the Young's moduli of the PT, PF and of the TA;
- the size (through a radial scaling) and the cone depth (through a unidirectional scaling).

Concerning the OC model, the selected parameters were:

- the ossicle masses;
- the γ angle;
- stiffness and damping constants of ligaments and tendons.

Where available (i.e. for TM thicknesses and Young's moduli and for the ossicle masses), reference lower and upper boundary values from the literature (Tab. 6.1 and Tab. 6.2, [161]) were adopted to vary the selected parameters with respect to the identified ones.

The size and cone depth of the TM were reasonably varied in the 25% range. Finally, concerning the CO stiffness and damping coefficients and the γ angle, due to the lack of certain data, values twice the calibrated value and half were adopted to investigate the model sensitivity. These variables include the translational elastic

Parameter	Lower bound	Upper bound	Identified
Malleus mass (mg)	22.1	35.1	30.42
Incus mass (mg)	24.2	38.7	26.47
Stapes mass (mg)	1.93	4.35	1.93

Table 6.2: Literature boundaries for sensitivity parameters of the ossicular chain model.

and damping constants of the TMMJ, ISJ (in the piston-like direction) and of the AML, PIL (in their main line of action), the damping constants of the ST and SOWJ in the piston-like direction and all the translational and rotational elastic and damping constants of the IMJ; for symmetry in the articulation anatomy, the IMJ constants were assumed equal in the piston-like and in the vertical directions. The sensitivity of three other variables, presenting a wide spread of values in the literature was tested (i.e. the SML, LML and TT translational elastic constant in their line of action).

As index of sensitivity, a percentage relative variation (i_S) was computed as:

$$i_S = \frac{\|x_{var}\| - \|x_{ref}\|}{\|x_{ref}\|} \tag{6.1}$$

where x_{var} and x_{ref} represent the varied and reference displacement amplitude vectors at each frequency in the 0.3-6 kHz frequency range. The expression corresponds to the ratio of the Root Mean Square (RMS) values of the varied and reference vectors and sums up the effects of parameter variations over the entire frequency range, allowing a comparison among them.

6.3 Results

As results of the calibration procedures, umbo and SFP displacement amplitudes, fitted on experimental data [93], are shown in Fig. 6.3 and Fig. 6.4 as reference curves. The sensitivity analysis results are presented in details in the following sections.

6.3.1 Tympanic membrane parameters

TM model sensitivity to size and cone depth features, was evaluated in terms of variations of umbo and SFP displacement curves, Fig.6.3a-b.

Size is definitely more influential than cone depth and marked variations appear especially in the high frequency range where an increase in size produces lower umbo and SFP displacements while an opposite trend occurs in the low frequency range.

The influence of the TM and TA thickness and Young's modulus is evident in Fig. 6.3c-d. A thickness increase produces lower umbo displacements at all frequencies while for the SFP that is observed only at high frequencies.

Concerning the Young's modulus, a noticeable decrease in displacement amplitudes at low frequency arises at high values of the elastic moduli, especially for the SFP, while at high frequency displacements appear unaffected in both cases.

It is worth noting that the reference values are close to the lower boundary of the assigned values so that variations on displacements are negligible.

6.3.2 Ossicular chain parameters

The sensitivity of the OC model to ossicles masses and the γ angle, was evaluated in terms of umbo and SFP displacement curves variations, Fig.6.4a-b. The influence of the elastic and damping constants is evident in Fig. 6.4c-d.

Results show a small influence of the assigned mass values on the curves, while a high influence of the γ angle is evident, mainly in the SFP curve, with lower displacement amplitudes for greater angles; for the umbo the influence of γ is limited to the low frequency range.

Considering the elastic and damping constants, a higher influence on the umbo displacement curve of the former with respect to the latter appears, while their influence on the SFP curve is comparable. For the umbo, higher variations mainly arise at low frequencies and an increase of the elastic constants produces an amplitude decrease. For the SFP an inversion of such a trend appears at high frequency while as regards the influence of damping, an increase of it produces, in general, lower amplitudes. Sensitivity indexes The sensitivity indexes for the TM and OC parameters are reported in Tab. 6.3 and Tab. 6.4, respectively.

The index signs are consistent with those of the parameter variations but for TM thickness and OC masses on SFP. Moreover the indexes appear to depend, in various cases, on the parameter variation magnitude indicating a non-linear dependence. In particular, higher sensitivity index values are obtained varying the TM thicknesses and increasing the Young's moduli.

Considering the sensitivity index values for the umbo response, the OC elastic constants and a decreasing γ angle appear to cause

Parameter	Umbo(%)	Stapes(%)
Size (lower)	-8.54	-8.16
Size (upper)	8.52	7.47
Cone depth (lower)	4.78	7.66
Cone depth (upper)	-4.60	-6.25
Thickness (lower)	26.98	37.99
Thickness (upper)	-21.78	6.30
Young's modulus (lower)	2.57	5.62
Young's modulus (upper)	-51.53	-60.76

Table 6.3: Tympanic membrane parameter sensitivity index.

higher variations. Concerning the SFP response, high values of the sensitivity indexes arise varying the γ angle and the damping constants.

6.4 Discussion

In the present chapter, a hybrid FE/MB middle ear model was introduced, where a FE model of the TM is connected to a MB scheme of the OC through a feedback strategy.

The sensitivity of the complete model was evaluated distinguishing the TM and the OC parameters in order to test its robustness to uncertainties. Geometric (size, cone depth and thickness) and material (Young's modulus) parameters of the TM and annulus were varied in the FE part of the model. Geometric (γ angle), inertial (ossicle masses) and material (elastic and damping constants) parameters of the OC and surrounding structures of the tympanic cavity (joints, ligaments and muscle tendons) were varied in the MB part of

Parameter	Umbo(%)	Stapes(%)
OC masses (lower)	0-62	0.46
OC masses (upper)	-1.45	7.11
γ angle (lower)	43.31	157.76
γ angle (upper)	-3.97	-58.86
Elastic const. (lower)	49.87	19.49
Elastic const. (upper)	-35.26	-19.91
Damping const. (lower)	8.22	36.05
Damping const. (upper)	-5.22	-32.57

Table 6.4: Ossicular chain parameter sensitivity index.

the model. The effect of parameters variations on umbo and stapes footplate centre displacement curves was examined with respect to a reference curve previously calibrated on literature experimental data [93].

As far as the TM model is concerned, the results show a higher sensitivity to thickness, and to the increased Young's moduli. On the other side for the MB model of the OC, the results show a higher sensitivity to the γ angle and to the elastic/damping constants in the umbo/stapes curves.

A patient-specific application involves an unavoidable variation in parameter values. The availability of accurate ex vivo and in vivo experimental data could help to limit uncertainties and increase the model reliability to simulate pathological/post-surgical/post-traumatic conditions and evaluate ossicular replacement prostheses. However, some influential parameters (e.g. the damping constants) are still not easily measurable and their determination will still require the application of identification techniques.

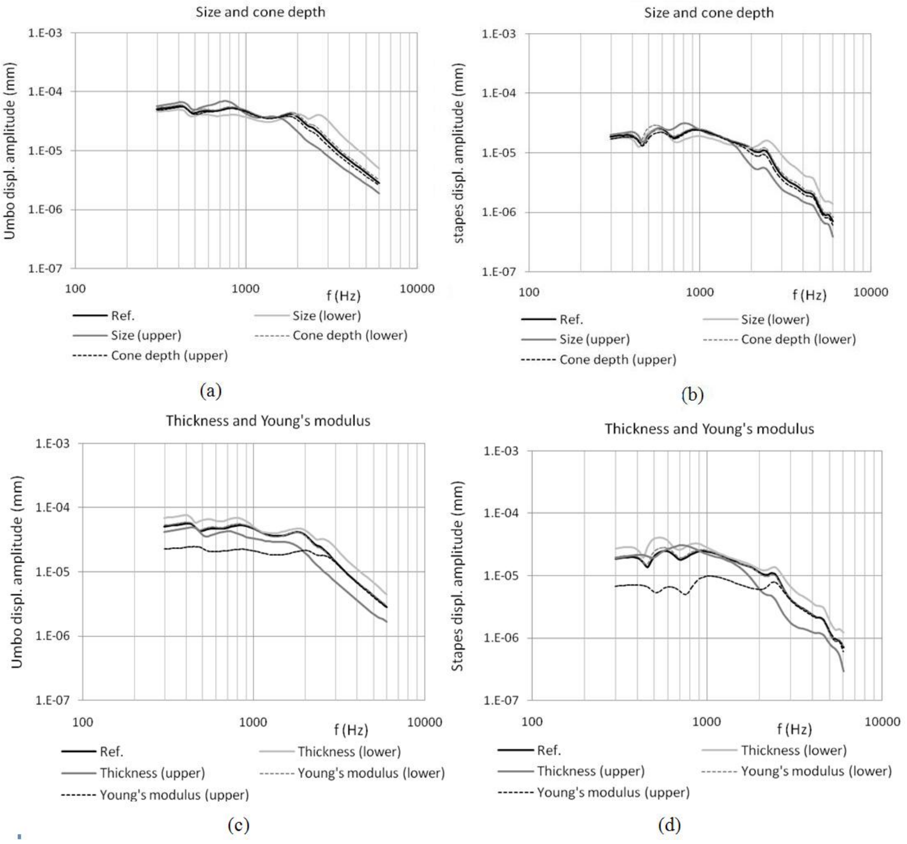

Figure 6.3: Sensitivity results to tympanic membrane parameters (size and cone depth (a, b), thickness and Young's modulus (c, d). Umbo (a, c) and stapes footplate (b, d) displacement amplitude curves.

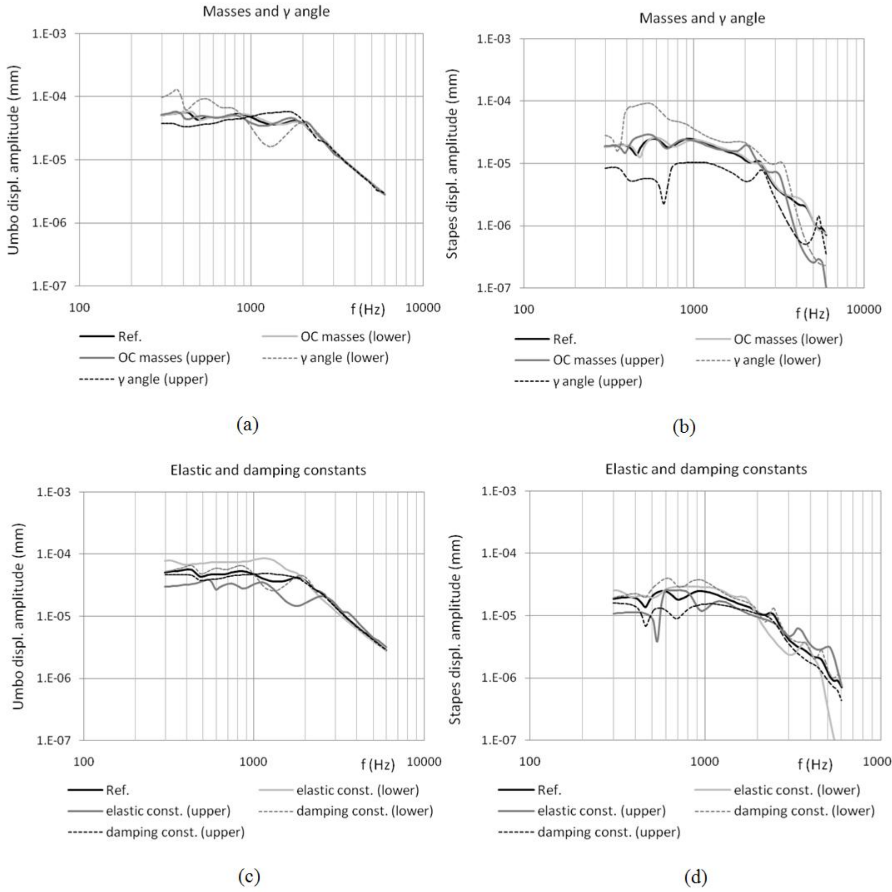

Figure 6.4: Sensitivity results to ossicular chain parameters (masses and γ angle (a, b), elastic and damping constants (c, d). Umbo (a, c) and stapes footplate (b, d) displacement amplitude curves.

Chapter 7

Psychoacoustics

Psychoacoustics, which is a branch of acoustics, deals with the relationships between the physical characteristics of sounds and their perceptual attributes [5, 182]. It is concerned with the frequency-dependent sensitivity of the auditory system, the masking processes, the loudness, pitch and timbre perception of sounds.

The information processing in the auditory system, in terms of preprocessing in the peripheral system (outer, middle and inner ear) and neural processing, both including non-linearities, is a central issue of the psychoacoustic approach. The most important physical magnitude for psychoacoustics is the time-varying sound pressure, in the 10^{-5}-10^{2} Pa amplitude range and in the 20 Hz- 20 kHz frequency range.

Psychoacoustic methodologies were investigated and applied within the project "Supporto tecnico per la revisione e l'aggiornamento di procedure per il calcolo di componenti MAGNA" in collaboration between the Department of Mechanical, Nuclear and Production Engineering of the University of Pisa and Magna Closures S.p.A. from March 2011. The research activity mainly focused on power windows acoustics for automotive application and included experimental and theoretical activities, as detailed in §7.3.2 and §7.3.3, respectively. The main objective of this study was to reproduce and predict the customers'opinion.

A first work package (RL 1280, April 2011) included the identification of suitable theoretical models of noise perception for automotive products, particularly referring to the state of the art on power window noise characterization, as detailed in §7.3.1. A second work package (RL 1291, December 2011) included the data processing and analysis of experimentally acquired signals, as described in §7.3.2 and §7.3.3. The project is still in progress and the future developments include a jury test as well as the validation of a computational modal and acoustic model with the aim to have an instrument to reproduce and predict the customers'perception, to simulate and design power windows mounted on car doors.

7.1 Characteristics of sounds and hearing area

Temporal and spectral characteristics of sound are frequently used in psychoacoustics [182]. The time varying sound pressure (Pa) is typically referenced. In order to account for such a broad range, the sound pressure level (SPL, dB) was introduced and defined as [182]:

$$SPL(dB) = 20\log_{10}\left(\frac{p_{rms}}{p_0}\right) \tag{7.1}$$

where p_{rms} and $p_0 = 20\ \mu$Pa denote the root mean square and the standard reference values, respectively. The RMS value is defined as:

$$x_{rms} = \sqrt{\frac{1}{n}\sum_{i=1}^{n} x(t_i)^2} \tag{7.2}$$

An alternative relation, known as the *Parseval* relation, can be adopted to estimate the RMS value in the discrete case:

$$x_{rms} = \frac{1}{n}\sqrt{\sum_{i=1}^{n} |X(f)|^2} \tag{7.3}$$

where $X(f)$ indicates the Fourier transform of $x(t)$. This expression is useful when the A-weighting is introduced in the computation to estimate the A-weighted SPL (dBA) (§7.2.1).

The SPL value has to be estimated in a time range which is determined by the time constant, introducing a moving window and applying the Fast Fourier Transform (FFT) algorithm. Among the conventionally defined time constants (i.e. 125, 1000 and 35 ms corresponding to *Fast*, *Slow* and *Impulse* time-weighting, respectively), the *Fast* one was adopted. The intensity (W/m^2) and intensity level are similarly defined, although less employed.

The hearing area is represented on a plot with frequency or critical bands as the abscissa, and sound pressure (Pa) or intensity (W/m^2) or the respective levels (dB) as the ordinate [182]. It is included in the $10^{-5} - 10^2$ Pa and 20 Hz- 20 kHz ranges of sound pressure values and frequency, respectively.

The critical-band concept is used in many models (e.g. *loudness* model). A *Bark* unit was defined leading to the so-called critical-band rate scale. This scale is based on the fact that our hearing system analyzes a broad spectrum into parts corresponding to critical bands.

The concept of critical bands was proposed assuming that the part of a noise that is effective in masking a test tone is the part of its spectrum lying near the tone [182]. The width of a critical band corresponds to a distance along the basilar membrane of about 1.3 mm, representing the ear's resolving power for simultaneous tones [182].

At low frequencies, critical bands show a constant width of about 100 Hz, while above 500 Hz critical bands show a bandwidth which is about 20% of centre frequency [182].

7.2 Psychoacoustic metrics and models

7.2.1 Loudness

Loudness is considered the metric which corresponds most closely to the sound intensity of a stimulus [182].

Loudness level in *phon* is defined as the SPL of a 1 kHz tone in a plane wave and frontal incident that is as loud as the sound in exam [182]. A 1 kHz, 40 dB SPL tone is assumed as reference for define 1 *sone*, the unit of measurement of *loudness*, corresponding to 40 *phon*. The relation between *phon* and *sone* units is based on the fact that an increment of 10 dB (e.g. 20 *phon*) corresponds to a doubling in perceived *loudness* above 40 dB SPL; below 40 dB SPL, the *loudness* decreases more quickly [5, 182].

Equal-loudness contours and A-weighting

The loci of points of equal *loudness* in the hearing area are called equal-loudness contours, typically defined for pure tones and for a frontally incident plane sound field [182].

Some weighting curves were conventionally defined as A, B, C and D-weighting curves. The A-weighting curve is the most frequently referenced in the norms and it is obtained reversing the 40 *phon* equal-*loudness* contour.

The equal-*loudness* contours highlight the *loudness* dependence on frequency, while the dependence on bandwidth, frequency content and duration are not evident. Therefore it is too simple to approximate *loudness* level of noises or complex tones (or combinations of both) by the A-weighted SPL [182].

Spectral effects

It is worth considering the uniform exciting noise. The 1 *sone* value is reached at 30 dB for uniform exciting noise. The Critical-band rate may also be used as the abscissa. This scale is more equivalent to features of our hearing system than frequency.

Band-pass noise of small bandwidths is as loud as the 1-kHz tone of the same level, up to a certain bandwidth. which corresponds to the critical bandwidth. Above the critical bandwidth, the loudness of the band-pass noise increases, clearly indicating the dependence of *loudness* on bandwidth [182]. Critical bandwidth plays a very important role in loudness sensation also for the loudness of two-tone complexes as a function of the frequency separation of the tones.

Other phenomenons have to be considered in *loudness* perception, such as the spectrally partial masking (e.g. the decrease in loudness of a tone by a spectrally separated partially masking high-pass noise) [182].

Temporal effects

Loudness depends on duration and repetition rate concerning a single tone burst and a sequence of sound bursts, respectively. The loudness of a tone burst decreases for durations smaller than about 100 ms. For longer durations, the loudness is almost independent of duration.

When a sound and a masker are not simultaneously presented, the pre- and post-masking effects influence temporally partially masked *loudness*. The pre-masking is evident when a second loud sound reduces the loudness of a preceding short sound. When a sound is presented after the termination of a masker, the effect is called post-masking [182].

Model of loudness

The previously described effects have to be considered in the development of a model of *loudness*.

Loudness N in *sone*, or "total *loudness*", is obtained as an integral of a *sone/Bark* variable ("specific *loudness*" or "*loudness* distribution/pattern", N') over critical-band rate[182]:

$$N = \int_0^{24Bark} N' dz \tag{7.4}$$

Specific *loudness* is developed assuming Stevens'law, stating that an intensity sensation grows with physical intensity following a power law.

With a constant of proportionality k, relating the specific *loudness* N' and its corresponding increment $\Delta N'$ to the excitation E and its corresponding increment ΔE the power law results:

$$\frac{\Delta N'}{N' + N'_{gr}} = k \frac{\Delta E}{E + E_{gr}} \tag{7.5}$$

where N'_{gr} and E_{gr} represents the internal noise floors.

Treating this equation of differences as a differential equation and introducing the reasonable boundary condition that $E = 0$ leads to $N' = 0$, the final expression using a reference specific loudness N'_0 results [182]:

$$N' = N'_0 \left(\frac{E_{TQ}}{sE_0} \right)^k \left[\left(1 + \frac{sE}{E_{TQ}} \right)^k - 1 \right] \tag{7.6}$$

where s is defined as the ratio between the intensity of the just-audible test tone and the intensity of the internal noise appearing within the critical band at the test tone's frequency, E_{TQ} is the excitation at threshold in quiet and E_0 is the reference excitation and $k = 0.23$.

For frequencies in the neighborhood of 1 kHz (s = 0.5) and with the additional boundary condition that a 1 kHz tone with a level of 40 dB has to produce exactly 1 *sone* as total *loudness*, a quantitative final equation for specific *loudness* (*sone/Bark*) is obtained as [182]:

$$N' = 0.08 \left(\frac{E_{TQ}}{E_0} \right)^{0.23} \left[\left(0.5 + 0.5 \frac{sE}{E_{TQ}} \right)^{0.23} - 1 \right] \tag{7.7}$$

Loudness calculating procedure

A procedure to calculate specific and total *loudness* for steady-state sounds was developed to make use of third-octave band levels and the implementation was published in DIN 45 631 [182]. A graphical *loudness* calculation procedure, part of the ISO 532 B international standard is described in [182], starting from a chart of the third octave band levels.

Approximating the human ear's frequency selectivity through third-octave band filters instead of critical-band filters involves that the differences in bandwidth are not 1 $Bark$ and a $k = 0.25$ value to account for additional specific *loudness* towards lower frequencies. Such an approximation is acceptable above 300 Hz since for lower frequencies, third octave band are too small with respect to critical bands. Therefore, the critical-band level has to be approximated by adding up the sound intensities falling in the given third-octave bands. For precise measurements, especially in cases where the components at very low frequencies are dominant, the procedure can gain accuracy introducing a tabulated weighting of the frequency components below 250 Hz corresponding to the equal *loudness* contours [182].

In the present work the specific and total *loudness* were computed according to DIN 45631/ISO 532B norm [182] through the available code[1]

For time-varying sounds, however, in addition the nonlinear temporal processing of *loudness* in the human hearing system has to be simulated in *loudness* meters. *Loudness* meters calculate the loud-

---

[1] http://www.acoustics.salford.ac.uk/res/cox/sound_quality/index.php?content=MATLABcodes

ness corresponding to ISO 532B almost instantaneously (i.e. using the same temporal characteristics as our hearing system). In order to simulate the characteristics of our hearing system, critical-band analysis has to be done every 2 ms. This means that a filter bank has to be installed that simulates the frequency selectivity of our inner ear.

A *loudness* meter can be made by a filter bank of third-octave-band filters, accounting also for temporal effects with respect to the graphical procedure accounting only for the spectral effects. The sound pressure time function is processed by the filter bank, a rectifier and a lowpass with 2 ms time constant producing the temporal envelope of the outputs [182].

The above mentioned generalization of *loudness* model, known as time-varying *loudness*, was introduced by [183] to account for temporal effects, according to DIN45631. The algorithm measures the third octave spectrum using exponential averaging with a 2 ms time constant, combines the fractional-octave bands into critical bands, and applies temporal and spectral masking, returning the specific *loudness* versus critical band rate and the integral of the specific *loudness*, applying temporal post-masking filters to measure the time-varying *loudness* (*LabView* 2010 Help, *National Instruments*).

In addition to *loudness* pattern and time function, statistical *loudness* distributions can be estimated, such as the percentile *loudness* N_i (e.g. *loudness* value reached or exceeded in $i\%$ of the measurement time). Mainly the N_{90} and N_5 values are referred in the literature [184].

In the power window application described in [185], peak values of time-varying loudness of a closing phase (i.e. stationary phase with initial and final transients) below to 30 *sone*, included in the 30-35 *sone* range or above 35 *sone* are associated to absence of negative impact, marginal and significant negative effects on perceived overall quality and annoyance, respectively.

7.2.2 Sharpness

The sensation of *sharpness* belongs to the timbre perception, but it is often considered separately [182]. The spectral envelope and the centre frequency of narrow-band sounds, rather than the fine structure, of a sound mainly influences the sensation of *sharpness*.

A narrow-band noise one critical-band wide at a centre frequency of 1 kHz having a level of 60 dB is conventionally assumed as reference sound producing 1 acum (i.e. the *sharpness* unit of measurement).

For narrow-band noises, *sharpness* increases with increasing centre frequency. For centre frequencies below 3 kHz, *sharpness* increases almost in proportion to critical-band rate. Above 3 kHz *sharpness* increases faster than the critical-band rate. This effect seems to be the reason that very high-frequency sounds produce a sensation that is dominated by their *sharpness*. From 200 Hz to 10 kHz, *sharpness* increases by a factor of 50.

The dependence of *sharpness* on bandwidth, as long as smaller than the critical band, can be ignored. However, *sharpness* is highly dependent on bandwidth as it is evident observing the *sharpness* of band-pass noise as a function of lower and upper cut-off frequency with an 10 kHz upper and a 0.2 kHz lower cut-off values, respectively [182].

Increasing the upper cut-off frequency from about 300 Hz increases *sharpness* continuously. Decreasing the lower cut-off frequency of this noise band decreases *sharpness* until 1 kHz and remains almost constant for further reduction.

The addition of noise at higher frequency increases the *sharpness*, as it was expected. However, *sharpness* can be decreased by adding sound at lower frequencies. This is an effect that may be unexpected.

These behaviors have to be considered developing a model of *sharpness*.

The *sharpness* metric, combined with *loudness* and relative RPM deviation of the electric motor, is a crucial factor in power window noise evaluation [184].

Model of sharpness

The spectral envelope, which mainly affects *sharpness*, may be represented by the specific *loudness* versus critical-band rate.

There are several methods to calculate *sharpness* (e.g Von Bismarck's method [186], Aures's method [187] and Zwicker and Fastl's method [182]).

Using the approach described in [182] *sharpness* S can be calculated as the weighted first moment of the specific *loudness* over critical-band rate:

$$S(acum) = 0.11 \frac{\int_0^{24Bark} N' g(z) z dz}{\int_0^{24Bark} N' dz} \tag{7.8}$$

where the $g(z)$ factor is critical-band rate dependent which is constant to a 1 value below 16 kHz and gradually increases only above 16 kHz to a value of 4. The denominator represents the total *loudness*.

In the present study, specific and total *sharpness* were computed as in [182].

7.2.3 Fluctuation strength and roughness

Two different kinds of hearing sensations are produced by modulated sounds: for a modulation frequency below 20 Hz and above 20 Hz, the sensations of *fluctuation strength* and *roughness* occur, respectively, with a smooth transition [182].

A unit of measurement (*vacil*) of *fluctuation strength* is defined for a 60 dB, 1-kHz tone 100% amplitude-modulated at 4Hz. The unit of measurement of *roughness* is the *asper*, defined for a 60 dB 1 kHz tone which is 100% modulated in amplitude with a 70 Hz modulation frequency.

The *fluctuation strength* shows a band-pass behavior as a function of modulation frequency with a maximum at 4 Hz, which corresponds to the speaking rate indicating the tuning of the hearing system during the evolution.

Fluctuation strength depends on SPL, modulation depth or factor and, in details, :

- increases at increasing SPL;
- is zero until a modulation depth of about 3 dB
- increases approximately linearly with the logarithm of modulation depth, reaching a maximum at 30 dB.

A little and a high dependence of *fluctuation strength* produced by amplitude- and frequency-modulated pure tones on centre frequency was shown in [182], respectively.

In [182] a large *fluctuation strength* is associated to amplitude-modulated broad-band noise and frequency-modulated pure tones with large frequency deviation probably due to the fact that excitation varies to a large extent along the critical-band rate scale. Therefore, the authors of [182] postulated that fluctuation strength is summed up across critical bands in developing a model.

At about 15 Hz the *roughness* sensation starts to increase, reaching a maximum at 70 Hz. It is produced by modulation frequencies in the 15-300 Hz, also without an exact periodicity. Frequency and temporal resolution of the hearing system influence the *roughness* sensation.

Frequency modulation can produce much larger *roughness* than amplitude modulation. Modulation frequency, together with the degree of modulation or the frequency modulation index in case of amplitude and frequency modulation, respectively, are considered the most influent parameters on *roughness*.

Fluctuation strength and *roughness* were applied to sound quality evaluation of power windows. Specific (versus the 24 critical bands in *Bark*) and total *fluctuation strength* and *roughness* were computed. The Aures's method [188] was adopted for *roughness* implementation.

Model of fluctuation strength

A model of fluctuation strength F was developed based on the equation [182]:

$$F \sim \frac{\Delta L}{(f_{mod}/4Hz) + (4Hz/f_{mod})} \tag{7.9}$$

where f_{mod} is the modulation frequency and ΔL represents the masking depth of the temporal masking pattern. The masking depth is a basic feature of the model which show a low-pass behavior.

While for test sounds, the ΔL is available, this is not true in practical applications. In some implementations, the corresponding differences in specific *loudness* are used instead of the ΔL values.

Model of roughness

In the model of *roughness* described in [182], the frequency resolution of the human ear is modeled by the excitation pattern or the specific *loudness* versus critical-band rate pattern since the hearing system is capable to detect only the differences in excitation produced by the modulation.

The temporal resolution also constitutes a main factor. The above mentioned ΔL values (masking depth of the temporal masking pattern) can account for temporal effects. However *roughness* is not only determined by the masking depth, but it is proportional also to the frequency modulation as in the following relation:

$$R \sim f_{mod}\Delta L \tag{7.10}$$

From the above equation and some considerations on the ΔL and f_{mod} trend versus the frequency, a maximum value arise at 70 Hz, following the experimental evidences.

For more precise calculations, the dependence of the ΔL value on the critical band rate have to be considered. Another approximation is proposed in [182]:

$$\begin{aligned} R(asper) &\sim f_{mod} \int_{0}^{24Bark} \Delta L_E(z) dz \\ &\sim 0.3 f_{mod}(kHz) \int_{0}^{24Bark} \Delta L_E(z) dz (dB/Bark) \end{aligned} \tag{7.11}$$

Again, since the ΔL values versus critical bands are not available in the general application, it can be advantageous, for example with the aim of a computer implementation, to transfer the ΔL values into the corresponding variations of specific *loudness* time function.

7.2.4 Tonality

The tonality concept (i.e. a feature distinguishing noise versus tone quality of sounds) is considered highly subjective and not quantifiable nor measurable in [182]. No dependencies on *loudness* or critical bands have been identified. Relative tonality, however, decreases with increasing critical band rate spread, starting from a tonality of unity for a sinusoidal tone to about 0.1 for critical band rate spread of 1.5 Bark.

In the present study the Aures’s algorithm [187] was adopted. The tonality metric (tu) measures the importance of a tone component with respect to the total spectrum of the signal.

7.2.5 Combined psychoacoustic metrics

A psychoacoustic metric model can be required to represent an experienced perceptual dimension as a combination of metrics. Combined metrics can be developed as regression models as functions of a number of acoustic or psychoacoustic metrics [189].

In [184] a linear regression model based on *loudness*, *sharpness* well predicted the subjectively perceived annoyance while a model based on *loudness*, *sharpness* and speed variations of the electric motor of a power window well predicted the overall product quality perception. It indicates that the speed variations of the electric motor are judged as a sign of bad quality.

Aures proposed a combination of *loudness* N, *sharpness* S, *roughness* R and *tonality* T known as *sensory pleasantness* [182, 189]. A relative value of *sensory pleasantness*, P/P_0 can be estimated for any sound as a first approximation through the equation [182]:

$$\frac{P}{P_0} = e^{-0.7R/R_0} e^{-1.08S/S_0} (1.24 - e^{-2.43T/T_0}) e^{-(0.023N/N_0)^2} \qquad (7.12)$$

where tonality is subjectively estimated.

Widman developed a combined metric named *psychoacoustic annoyance*, (PA), based on the fifth percentile of *loudness*, $N_5(sone)$, *sharpness*, $S(acum)$, *roughness*, $R(asper)$, and *fluctuation strength*, $F(vacil)$, to evaluate sound quality [182, 189].

The psychoacoustic elements and annoyance ratings of annoying sounds can be quantitatively described by the PA, which is a combination of hearing sensations.

Based on results of psychoacoustics experiments with modulated versus unmodulated narrow-band and broad-band sounds of different spectral distribution, a quantitative description was developed as follows [182]:

$$PA = N_5 \left(1 + \sqrt{w_S^2 + w_{FR}^2} \right) \qquad (7.13)$$

where

$$\begin{aligned} w_S &= 0.25(S-1.75)log(N_5+10) \quad if \quad S>1.75 \\ w_S &= 0 \quad if \quad S<1.75 \end{aligned} \tag{7.14}$$

to account for *sharpness*, and

$$w_{FR} = \frac{2.18}{N_5^{0.4}}(0.4F+0.6R) \tag{7.15}$$

to account for *fluctuation strength* and *roughness*.

It is commented in [182] that PA can be predictive of data from psychoacoustic experiments also for technical sounds like car or tool noises.

In the present study, the PA index was implemented and applied to power window sound quality evaluation.

7.3 Application to power window noise evaluation

7.3.1 State of the art

Noise perception in automotive products and components was studied from the Nineties. It is considered crucial in global quality perception of a car. Therefore, the prediction of customer's expectations is the main aim of most acoustics and psychoacoustics studies, as well as the noise sources identification and a consequent conscious design of components. Studies on acoustics of power windows [184, 185, 190] and other automotive DC motor-powered mechanisms (e.g. powered seat adjusters) were collected. From the analysis of the recent literature the following information arose, mainly concerning:

- the experimental set-up to test interior noise or automotive components;
- the objective and subjective characterization techniques of acoustic signals from automotive products;
- the main temporal and frequency features of power window noise;
- the identified noise mechanical sources and the consequent design guidelines oriented to noise limitation, including threshold values on some computable (also psychoacoustic) variables.

The analysis techniques to characterize automotive product sound quality can be classified as:

- subjective evaluation techniques in listening jury tests (e.g. individual preferences rating scales, and paired comparison tests);
- psychoacoustic metrics (e.g. loudness, sharpness, roughness, fluctuation strength and kurtosis) and models (e.g. Psychoacoustic Annoyance (PA));
- correlation techniques between objective measurements and subjective tests applying statistical analysis tools;
- order analysis and indices to quantify the relative RPM deviation (e.g. motor DIP [190]);
- time-frequency analysis techniques (e.g. fast (FFT) and short time (STFT) Fourier transform, spectrogram, power spectral

density (PSD), third octave band spectrum, cepstrum, Wigner-Ville distribution and ambiguity function, wavelet transforms);

- artificial neural networks and fuzzy logic, also combined with wavelet analysis;
- Computer Aided Engineering (CAE) models and, in particular, FE method, dynamic simulation of elastic bodies and lumped-parameter models.

7.3.2 Materials and experimental activity

The experimental activity was conducted in three sessions between April and September 2011 at MAGNA Closures S.p.A in Guasticce (Collesalvetti, LI) and at the Scalbatraio laboratory in San Piero a Grado (PI). The instrumentation included a microphone, some accelerometers, a Hall rolling velocity transducer on the electric motor, an instrumented hammer with a steel tip. Two kinds of tests were run:

- closing (travelling-up)-opening (travelling-down) event sequences of the power window rail to evaluate the component noise, varying the test conditions in terms of input voltage, kind of DC motor, with or without silent blocks;
- impact tests (”Multiple-reference Impact Test”) with an instrumented hammer, to characterize the component dynamic behavior and to validate a computational model;

with the decoupled component (both in the free-free, or grounded-grounded test boundary conditions) or fixed to a car door.

Additional tests in a semi-anechoic chamber were run at EuroAcoustics in Avigliana (TO) on November 2011. During this session, 39 decoupled DC motors for power windows were tested in a free-free condition while 12 power window rails were fixed on a rigid fixture and tested in different configurations of input voltage and load, according to technical specifications. Data from microphone and accelerometers recorded in these acquisitions will be available for processing in the near future and are not included in the following data processing presentation.

7.3.3 Methods and models

Data processing consisted of analysis techniques partially deduced from the state of the art review. Some general analysis instruments were applied to the microphone and accelerometer signals to evaluate sound quality:

- the Sound Pressure Level (SPL) vs. time with "Fast" time exponential averaging, with reference value $p_0 = 20\ \mu\text{Pa}$. An analogous expression was employed for accelerometer signals with a reference value $a_0 = 10^{-6}\ \text{m/s}^2$. The SPL was expressed in dBA applying the A-weighting to account for the different sensitivity of the human ear in the frequency range. Temporal characteristics were distinguished into time segments (e.g. transient initial and stopping events and stationary travelling phase) by means of a semi-automatic identification based on the SPL (dBA) function.
- auto- and cross-correlation to evaluate the repeatability of ex-

perimental set-up;

- Signal to Noise Ratio (SNR), evaluated on the raw sound pressure time function or on the SPL (dBA), to estimate the ground noise;
- signal conditioning and filtering techniques, investigated to limit the measuring noise, to avoid aliasing problems in decimation procedures, to segregate the DC motor sound (¡ 1500 Hz) and most of the window seal scratching (¿ 1500 Hz) [184];
- time-frequency analyses and, in details: FFT of stationary signals; spectrogram, computed by means of STFT; PSD function; the third octave band spectrum (dB or dBA).

The following methodologies were applied to the microphone signal, focusing on the travelling-up segment:

- parameters from customer's specifications and data sheets in the time and frequency domains;
- kurtosis function to quantify the squeak phenomenon;
- psychoacoustic metrics and models [182] and, in details: specific and total loudness (DIN 45631, ISO 532B) for stationary signals, time-varying loudness and loudness percentiles; total and specific sharpness, roughness and fluctuation strength; PA model, a combination of loudness percentile, sharpness, fluctuation strength and roughness metrics.

Scalar parameters were computed to characterize the DC motor velocity in the closing phases, monitored by a Hall transducer, since motor velocity variations appear to have a high influence on radiated noise:

- the percentual decrement (”motor DIP”, [190] with respect to the mean value (RPM) of rotational velocity of the DC motor and translational velocity of the glass;
- the Relative RPM Deviation (RRD), ”steadiness” metrics [184].

Concerning the impact hammer tests, the accelerometer signals and hammer load cell were processed applying the following methodologies:

- Frequency Response Function (FRF) estimation and partial completion of the FRF matrix;
- quality checks: reciprocity check (based on the FRF matrix symmetry) to evaluate the linearity and the quality of the measurement system; force auto-spectrum, to identify the frequency range of excitation and response; coherence function, to estimate the degree of linear relation between the input/ouput signals.
- modal parameter extraction techniques (e.g. Peak Picking method, ARX/ARMAX models, Least Square Complex Exponential Method).

7.3.4 Results and discussion

The experimental and theoretical analyses allowed to define and tune a procedure to investigate the sound quality of power windows. Some methodologies and parameters were introduced and compared with threshold values from the literature and reference specifications from data-sheets. From the analysis of the closing-opening sequence signal, the following conclusions can be drawn:

- the SPL (dBA) time function is highly related to the supply voltage, to the DC motor type and to the presence of silent blocks, in terms of temporal phases duration, maximum, mean and minimum values in the travelling-up phases;
- loudness, a loudness percentile and the integral of the exceeding area of the third octave band spectrum out of a reference specification mask showed lower values for the V5 motor and with silent-blocks;
- psychoacoustic metrics and models, such as the PA and the maximum value of the time-varying loudness were able to distinguish between test arrangements, although they result controversially related in different sessions;
- the scalar motor DIP and RRD were sensitive to the load conditions of the electric motor. The RPM variation time function results strictly related to the SPL (dBA) time function of the microphone signal in all tracks, indicating an high influence on noise generation;
- in addition to the introduced scalar indices, the analysis of the spectra of the microphone and accelerometer signals completes the quantitative and objective description of different experimental configurations.

From the analysis of the closing phases, significant differences arise between tests conducted with the component in different arrangements (decoupled in the free-free or grounded-grounded boundary conditions or mounted on a car door) in terms of duration difference between travelling-up and travelling-down phases; these differences can be dependent on the fact that a constant weight does not exactly reproduce the variable resistance of the seals on the glass; the line of action of the load, relative to the component, also depends on the orientation and fixing of the component to the panel and it can not exactly reproduce the glass action.

Guidelines for future experimental activities were identified from the analysis of background noise and repeatability: a standardization of the experimental conditions (e.g. environment, mounting, measurement system); quality checks prior to the acquisition; recording of several repetitions of a track with the aim of increasing the statistical significance; a sensitivity analysis to identify the dispersion sources (e.g. the variability among component, mounting or environment); a sensitivity analysis of data processing results to mechanical changes with the aim to gain a thorough knowledge of all parts of the system/component. The application of further analysis techniques (e.g. order analysis, cepstrum, wavelet analysis and Wigner-Ville distribution) can constitute an in-depth examination, although they are not readily understandable or can be oriented to the evaluation of the decoupled motor or gearmotor.

Conclusions

The main research activity carried out during the PhD course consists in the investigation and development of mathematical models of the human ear with the aim of predicting the human sound perception.

On the basis of a thorough review of the literature on ear anatomy, physiology and modeling, outer and middle ear models were developed as first stages to build a "virtual" ear.

In details, the auditory canal and the tympanic membrane were modeled in a finite element (FE) environment. A multi-body (MB) model of the ossicular chain and supporting structures (joints, ligaments and muscle tendons) was developed and combined with the tympanic membrane FE model in a hybrid FE-MB model of the complete middle ear. Generalized FE methods were also applied to the acoustic canal-tympanic membrane model.

A comparison between literature FE models of the tympanic membrane was conducted. Calibration procedures were adopted to tune the highly widespread parameters of the ossicular chain model. The sensitivity of developed models to uncertain parameters was also investigated with the aim of identify the most relevant parameters.

The combination of the outer and middle ear models, together with the development of models of the inner ear constitutes the main future developments of the undertaken research activity. The availability of a complete "virtual" ear, as a patient-specific tool, evenly based on accurate data from experimental activities, constitutes the main objective of the future research activity.

In parallel, during the last year of the PhD course, the quantitative correlation between the physical characteristics of sounds and the hearing perception due to the information processing of the auditory system as a whole, was investigated in terms of psychoacoustic mathematical models, applied to an experimental and theoretical activity on power window noise carried out within a project in collaboration with the MAGNA Closures S.p.A.

As a future development, a listening jury test is in progress with the aim to validate and develop psychoacoustic metrics and models, correlating with the subjective sensation. Moreover, the development and validation of a computational modal and acoustic model as a tool to predict design power windows accounting to customers' sound perception is in progress.

Bibliography

[1] H. Fastl and E. Zwicker. *Psycho-acoustics: facts and models.* Springer, 2007.

[2] G. Moncada Lo Giudice and S. Santoboni. *Acustica.* Masson, 1995.

[3] H. Gray. *Anatomy of the Human Body, 20th edition revised and re-edited by Warren H. Lewis Philadelphia: Lea and Febiger, 1918 New York: Bartleby.com.* http://www.bartleby.com/107/, 2000.

[4] F. A. Everest. *The Master Handbook of Acoustics.* Edition 4, Mc Graw-Hill, 2000.

[5] T. D. Rossing. *Springer Handbook of Acoustics.* Springer, 2007.

[6] S. A. Gelfand. *Essentials of Audiology.* Thieme, 2009.

[7] D. J. Lim. Structure and function of the tympanic membrane: A review. *Acta oto-rhino-laryngologica belg.*, 49:101–115, 1995.

[8] W. R. J. Funnell and C.A. Laszlo. A critical review of experimental observations on ear-drum structure and function. *ORL*, 44:181–205, 1982.

[9] W. F. Decraemer and W. R. J. Funnell. Anatomical and mechanical properties of the tympanic membrane. *Chronic otitis media: Pathogenesis-oriented therapeutic management, B. Ars (ed.), Kugler, The Hague*, pages 51–84, 2008.

[10] M. Ferrazzini. *Virtual Middle Ear: a Dynamic Mathematical Model Based On The Finite Element Method.* PhD thesis, Swiss Federal Institute of Technology. Diss. ETH no 15294, 2003.

[11] D. J. Kelly. A study of middle ear biomechanics using the finite element method. Master's thesis, University of Dublin Trinity College, 2001.

[12] J. Aernouts and J. J. J. Dirckx. Elastic characterization of the gerbil pars flaccida from in situ inflation experiments. *Biomech Model Mechanobiol*, 2010 Nov 11, 2010.

[13] N. P. Daphalapurkar, C. Dai, R. Z. Gan, and H. Lu. Characterization of the linearly viscoelastic behavior of human tympanic membrane by nanoindentation. *Journal of the Mechanical Behavior of Biomedical Materials*, 2(1):82–92, 2009.

[14] F. Zhao, T. Koike, J. Wang, H. Sienz, and R. Meredith. Finite element analysis of the middle ear transfer functions and related pathologies. *Medical Engineering and Physics*, 31:907–916, 2009.

[15] R. Z. Gan, B. Feng, and Q. Sun. Three-dimensional finite element modeling of human ear for sound transmission. *Annals of Biomedical Engineering*, 32:847–859, 2004.

[16] T. Koike, H. Wada, and T. Kobayashi. Modeling of the human middle ear using the finite-element method. *The Journal of the Acoustical Society of America*, 111(3):1306–1317, 2002.

[17] C. L. Kuypers, W. F. Decraemer, J. J. J. Dirckx, and J. P. Timmermans. Thickness distribution of fresh eardrums of cat obtained with confocal microscopy. *JARO*, 6:223–233, 2005.

[18] Y. Koyo. Morphological studies of the human tympanic membrane. *J. Otolaryngol. Jpn.*, 57:115–126, 1954.

[19] I. Kirikae. The structure and function of middle ear. *Tokio University Press*, page 60, 1960.

[20] D. J. Lim. Human tympanic membrane. an ultrastructural observation. *Acta Oto-laryngologica*, 70(3):176–186, 1970.

[21] Y. Oka T. Ishii K. Kamifusa, A. Kodama. Thickness of human normal ear drum. *Ear Res. Jpn.*, 19:16–21, 1988.

[22] K. Uebo, A. Kodama, Y. Oka, and T. Ishii. Thickness of normal human tympanic membrane. *Ear Res Jpn*, 19:70–3, 1988.

[23] S. H. Schmidt and S. Hellstrom. Tympanic-membrane structure-new views. a comparative study. *ORL Journal for Oto-rhinolaryngology and its Related Specialities*, 53(1):32–36, 1991.

[24] C.B. Ruah, P.A. Schachern, D. Zelterman, M.M. Paparella, and T.H. Yoon. Age-related morphologic changes in the human tympanic membrane. *Arch Otolaryngol Head Neck Surg*, 117:637–34, 1991.

[25] L. C. Kuypers, W. F. Decraemer, and J. J. J. Dirckx. Thickness distribution of fresh and preserved human eardrums measured with confocal microscopy. *Otology and Neurotology*, 27(2):256–264, 2006.

[26] T. Cheng, C. Dai, and R.Z. Gan. Viscoelastic properties of human tympanic membrane. *Annals of Biomedical Engineering*, 35:305–314, 2007.

[27] G. v. Békésy. The structure of the middle ear and the hearing of one's own voice by bone conduction. *J. Acoust. Soc. Am.*, 21:217–232, 1949.

[28] G. v. Békésy. *Experiments in Hearing.* McGraw-Hill, 1960.

[29] W. F. Decraemer, M. A. Maes, and V. J. Vanhuyse. An elastic stress-strain relation for soft biological tissues based on a structural model. *Journal of Biomechanics*, 13:463–468, 1980.

[30] J. Fay, S. Puria, W. F. Decraemer, and C. Steele. Three approaches for estimating the elastic modulus of the tympanic membrane. *Journal of Biomechanics*, 38:1807–1815, 2005.

[31] H. Luo, C. Dai, R. Z. Gan, and H. Lu. Measurement of young's modulus of human tympanic membrane at high strain rates. *Journal of Biomechanical Engineering*, 131:064501–7, 2009.

[32] H. Luo, H. Lu, C. Dai, and R. Z. Gan. A comparison of young's modulus for normal and diseased human eardrums at high strain rates. *Int. J. Experimental and Computational Biomechanics*, 1(1):1–22, 2009.

[33] A. N. Buytaert, J. E. F. Aernouts, and J. J. J. Dirckx. Indentation measurements on the eardrum with automated projection moir profilometry. *Optics and Lasers in Engineering*, 47:301–309, 2009.

[34] J. Aernouts, J. A. M. Soons, and J. J. J. Dirckx. Quantification of tympanic membrane elasticity parameters from in situ point indentation measurements: Validation and preliminary study. *Hearing Research*, 263(1-2):177–182, 2009.

[35] G. Huang, N. P. Daphalapurkar, R. Z. Gan, and H. Lu. A method for measuring linearly viscoelastic properties of human tympanic membrane using nanoindentation. *Journal of Biomechanical Engineering*, 130:014501–1, 2008.

[36] S. M. Hesabgar, H. Marshall, S. K. Agrawal, A. Samani, and H. M. Ladak. Measuring the quasi-static young's modulus of the eardrum using an indentation technique. *Hearing Research*, 263:168–176, 2010.

[37] J. Aernouts, I. Couckuyt, K. Crombecq, and J. J.J. Dirckx. Elastic characterization of membranes with a complex shape using point indentation measurements and inverse modelling. *International Journal of Engineering Science*, 48:599–611, 2010.

[38] A. Elner, S. Ingelstedt, and A. Ivarsson. The elastic properties of the tympanic membrance system. *Acta Otolaryngol.*, 72:397–403, 1971.

[39] M. Gaihede. Mechanics of the middle ear system: computerized measurements of its pressure-volume relationship. *Auris Nasus Larynx*, 26:383–99, 1999.

[40] M. Gaihede, D. Liao, and H. Gregersen. In vivo areal modulus of elasticity estimation of the human tympanic membrane system: modelling of middle ear mechanical function in normal young and aged ears. *Phys. Med. Biol.*, 52:803–814, 2007.

[41] K. R. Jr. Whittemore, S. N. Merchant, B. B. Poon, and J. J. Rosowski. A normative study of tympanic membrane motion in humans using a laser doppler vibrometer (ldv). *Hearing Research*, 187:85–104, 2004.

[42] J. J. Rosowski, R. P. Mehta, and S. N. Merchant. Diagnostic utility of laser-doppler vibrometry in conductive hearing loss with normal tympanic membrane. *Otol Neurotol.*, 25(3):323–332, 2004.

[43] J. J. Rosowski, H. H. Nakajima, and S. N. Merchant. Clinical utility of laser-doppler vibrometer measurements in live normal and pathologic human ears. *Ear Hear.*, 29(1):3–19, 2008.

[44] A. M. Huber, C. Schwab, T. Linder, S. J. Stoeckli, M. Ferrazzini, N. Dillier, and U. Fisch. Evaluation of eardrum laser doppler interferometry as a diagnostic tool. *The Laryngoscope*, 111:501–507, 2001.

[45] E. Dalhoff, D. Turcanu, H. P. Zenner, and A. W. Gummer. Distortion product otoacoustic emissions measured as vibration on the eardrum of human subjects. *PNAS*, 104(5):1547–1551, 2007.

[46] H. J. Foth, C. Huthoff, M. Brenner, S. Ftirber, N. Stasche, A. Baker-Schreyer, and K. Hiirmann. Measuring the motions in the human middle ear by laser doppler vibrometry. *Optics and Lasers in Engineering*, 25:289–301, 1996.

[47] C. H. Jang, H. Park, C. H. Choi, Y. B. Cho, and I. Y. Park. The effect of increased inner ear pressure on tympanic membrane vibration. *International Journal of Pediatric Otorhinolaryngology*, 73:371–375, 2009.

[48] J.R.M. Aerts and J.J.J. Dirckx. Nonlinearity in eardrum vibration as a function of frequency and sound pressure. *Hearing Research*, pages 26–32, 2010.

[49] O. de La Rochefoucauld and E. S. Olson. A sum of simple and complex motions on the eardrum and manubrium in gerbil. *Hearing Research*, 263(1-2):9–15, 2009.

[50] A. Eiber, H. G. Freitag, and T. Hocke. On the relationship between mft-patterns and the dynamical behavior of the middle ear. *The Function and Mechanics of Normal, Diseased and Reconstructed Middle Ears*, pages 157–166, 2000.

[51] S. M. Khanna and J. Tonndorf. Tympanic membrane vibrations in cats studied by time-averaged holography. *J. Acoust. Soc. Am.*, 51:1904–20, 1972.

[52] J. Tonndorf and S. M. Khanna. Tympanic-membrane vibrations in human cadaver ears studied by time-averaged holography. *J. Acoust. Soc. Am.*, 52:1221–1233, 1972.

[53] O. J. Lokberg and K. Hogmonen. Vibration phase mapping using electronic speckle pattern interferometry. *Appl. Opt.*, 15:2701–04, 1976.

[54] H. Wada, M. Ando, M. Takeuchi, H. Sugawara, T. Koike, T. Kobayashi, K. Hozawa, T. Gemma, and M. Nara. Vibration measurement of the tympanic membrane of guinea pig temporal bones using time-averaged speckle pattern interferometry. *J. Acoust. Soc. Am.*, 111 (5):2189–2199, 2002.

[55] H. O. Saldner. Phase-stepped television holographic technique for measuring phase and amplitude maps of small vibrations. *Appl. Opt.*, 35:3791–98, 1996.

[56] A. L. Dancer, R. B. Franke, P. Smigielski, F. Albe, and H. Fagot. Holographic interferometry applied to the investigation of tympanicmembrane displacements in guinea pig ears subjected to acoustic impulses. *J. Acoust. Soc. Am.*, 58:223–228, 1975.

[57] C. Furlong, J. J. Rosowski, N. Hulli, and M. E. Ravicz. Preliminary analyses of tympanic-membrane motion from holographic measurements. *Blackwell Publishing Ltd Strain*, 45:301–309, 2009.

[58] J. J. Rosowski, J. T. Cheng, M. E. Ravicz, N. Hulli, M. Hernandez-Montes, E. Harrington, and C. Furlong.

Computer-assisted time-averaged holograms of the motion of the surface of the mammalian tympanic membrane with sound stimuli of 0.4-25 khz. *Hearing Research*, 253:83–96, 2009.

[59] A. A. Aarnisalo, J. T. Cheng, M. E. Ravicz, C. Furlong, S. N. Merchant, and J. J. Rosowski. Motion of the tympanic membrane after cartilage tympanoplasty determined by stroboscopic holography. *Hearing Research*, 263(1-2):78–84, 2009.

[60] M. Hernndez-Montes, C. Furlong, J. J. Rosowski, N. Hulli, E. Harrington, J. Tao Cheng, M. E. Ravicz, and F. Mendoza Santoyo. Optoelectronic holographic otoscope for measurement of nanodisplacements in tympanic membranes. *J Biomed Opt.*, 14(3):1–17, 2009.

[61] J. T. Cheng, A. A. Aarnisalo, E. Harrington, M. Hernandez-Montes, C. Furlong, S. N. Merchant, and J. J. Rosowski. Motion of the surface of the human tympanic membrane measured with stroboscopic holography. *Hearing Research*, 263:66–77, 2010.

[62] E .W. Abel and R.M. Lord. A finite element model for evaluation of middle ear mechanics. In *Proceedings of the 22rd Annual EMBS International Conference*, volume 2, pages 2110–2112, 2001.

[63] C. D. Le and Q. L. Huynh. Mathematical models of human middle ear in chronic otitis media. In *Proceedings of the 5th International Conference on Information Technology and Application in Biomedicine*, pages 426–429, 2008.

[64] P. Ferris and P.J. Prendergast. Middle-ear dynamics before and after ossicular replacement. *Journal of Biomechanics*, 33(5):581–590, 2000.

[65] D. J. Kelly, P. J. Prendergast, and A. W. Blayney. The effect of prosthesis design on vibration of the reconstructed ossicular chain a comparative finite element. *Otology and Neurotology*, 24:11–19, 2003.

[66] Y. Liu, S. Li, and X. Sun. Numerical analysis of ossicular chain lesion of human ear. *Acta Mech Sin*, 25:241–247, 2009.

[67] C. Lee, P. Chen, W. Lee, Y. Chou, J. Chen, and T. Liu. Computer aided modeling of human mastoid cavity biomechanics using finite element analysis. *EURASIP Journal on Advances in Signal Processing*, 2010:9, 2010.

[68] U. B. Willi. Middle-ear mechanics: The dynamic behavior of the incudo-malleolar joint and its role during the transmission of sound. Master's thesis, University of Zurich., 2003.

[69] U. B. Willi, M. A. Ferrazzini, and A. M. Huber. The incudo-malleolar joint and sound transmission losses. *Hearing Research*, 174:32–44, 2002.

[70] H. Helmholtz. The mechanism of the ossicles of the ear and the tympanic membrane. *Pflügers Arch. Physiol. (Bonn)*, 1:1–60, 1868.

[71] K. Gyo, H. Aritomo, and R. J. Goode. Measurement of the ossicular vibration in human temporal bones by use of a video

measuring system. *Acta. Oto-laryngol (Stockh)*, 103:87–95, 1987.

[72] W. Decraemer and S. Khanna. New insights into vibration of the middle ear. In *Rosowski JJ, Merchant SN (eds) Second International Symposium on Middle-Ear Mechanics in Research and Otosurgery, Boston, MA, USA, 1999. The Hague, The Netherlands*, pages 23–38. Kugler, 2000.

[73] A. Eiber and H. G. Freitag. On simulation models in otology. *Multibody System Dynamics*, 8:197–217, 2002.

[74] K. B. H*ü*ttenbrink. The middle ear as a pressure receptor, proc. of the international workshop on middle ear mechanics in research and otosurgery. In *Dresden, Germany,*, pages 15–20, 1996.

[75] W. F. Decraemer, S. M. Khanna, J. Rosowski, and S. N. Merchant. Complete 3-dimensional motion of the ossicular chain in a human temporal bone. In *Abstract, Proc. Twenty-fourth Annual Research Meeting of the Association for Research in Otorhinolaryngology*, page 221, 2001.

[76] H. Dahmann. Zur physiologie des horens; experimentelle untersuchungen uber die mechanik der gerhorknochelchenkeltte, sowie uber deren verhalten auf ton und luftdruck. *Z Hals-Nasen-Ohrenheilkd*, 24:462–497, 1929.

[77] W.F. Decraemer and S.M. Khanna. Modelling the malleus vibration as a rigid body motion with one rotational and one

translational degree of freedom. *Hearing Research*, 72:1–18, 1994.

[78] J. Zwislocki. Analysis of the middle ear function. *J. Acoust. Soc. Am.*, 34:1514–1523, 1962.

[79] K. B. Huttenbrink. Middle ear mechanics and their interface with respect to implantable electronic otologic devices. *Otolaryngol Clin North Am.*, 34(2):315–335, 2001.

[80] J. A. N. Buytaert, W. H. M. Salih, M. Dierick, P. Jacobs, and J. J. J. Dirckx. Realistic 3d computer model of the gerbil middle ear, featuring accurate morphology of bone and soft tissue structures. *Jaro*, 12(6):681–696, 2011.

[81] T. Cheng and R. Z. Gan. Mechanical properties of stapedial tendon in human middle ear. *J. Biomech. Eng.*, 129(6):913–918, 2007.

[82] T. Cheng and R. Z. Gan. Experimental measurement and modeling analysis on mechanical properties of tensor tympani tendon. *J. Biomech. Eng.*, 30:358–366, 2008.

[83] T. Cheng and R. Z. Gan. Mechanical properties of anterior malleolar ligament from experimental measurement and material modeling analysis. *Biomechanics and Modeling in Mechanobiology*, 7(5):387–394, 2008.

[84] P. Parent and J. B. Allen. Time-domain “wave” model of the human tympanic membrane. *Hearing Research*, 263(1-2):152–67, 2010.

[85] D. Chitore, S. Saxena, and P. Mukhopadhyay. Electronic model of the middle ear. *Med. Biol. Eng. Comput.*, 21(2):176–178, 1983.

[86] W. Yao, H. Zhou, B. Hu, X. Huang, and X. Li. Research on ossicular chain mechanics model. *Hindawi Publishing Corporation,Mathematical Problems in Engineering*, 2012:1–14, 2010.

[87] C. Stieger, H. Bernhard, D. Waeckerlin, M. Kompis, J. Burger, and R. Haeusler. Human temporal bones versus mechanical model to evaluate three middle ear transducers. *MJ. Rehabil. Res. Dev.*, 44(3):407–415, 2007.

[88] T. Wright. The linear and nonlinear biomechanics of the middle ear. Master's thesis, University dissertation, Dept. of Otolaryngology, University Hospital, S22185 Lund, Swedem, 2005.

[89] A. Eiber and W. Schiehlen. Reconstruction of hearing by mechatronical devices. *Robot. Auton. Syst.*, 19:199–204, 1996.

[90] W. R. J. Funnell and C.A. Laszlo. Modelling of the cat eardrum as a thin shell using the finite-element method. *J. Acoust. Soc. Am.*, 63(5):1461–1467, 1978.

[91] C. S. Mikhael, W.R.J. Funnell, and M. Bance. Middle-ear finite-element modelling with realistic geometry and a priori material-property estimates. In *Proceedings of Can. Medical and Biological Engineering Society*, pages 126–129, 2004.

[92] R. Z. Gan, C. Dai, X. Wang, D. Nakmali, and M. W. Wood. A totally implantable hearing system-design and function char-

acterization in 3d computational model and temporal bones. *Hearing Res.*, 263(1-2):138–144, 2010.

[93] R. Z. Gan, T. Cheng, C. Dai, F. Yang, and M. W. Wood. Finite element modeling of sound transmission with perforations of tympanic membrane. *J. Acoust. Soc. Am.*, 126.

[94] R. Z. Gan, B. P. Reeves, and X. Wang. Modeling of sound transmission from ear canal to cochlea. *Annals of Biomedical Engineering*, 35(12):2180–2195, 2007.

[95] R. Z. Gan, Q. Sun, B. Feng, and M. W. Wood. Acoustic-structural coupled finite element analysis for sound transmission in human ear. pressure distributions. *Medical Engineering and Physics*, 28(5):395 – 404, 2006.

[96] Gan R.Z. and Sun Q. Finite element modeling of human ear with external ear canal and middle ear cavity. In *Engineering in Medicine and Biology 24th Annual Conference and the Annual Fall Meeting of the Biomedical Engineering Society EMBS BMES Conference*, volume 1, pages 264–265, 2002.

[97] Q. Sun, R.Z. Gan, K. H. Chang, and K. J. Dormer. Computer-integrated finite element modeling of human middle ear. *Biomechan Model Mechanobiol 1, Springer-Verlag*, 1:109–122, 2002.

[98] C. Lee, P. Chen, W. J. Lee, J. H. Chen, and T. C. Liu. Computer aided three-dimensional reconstruction and modeling of

middle ear biomechanics by high-resolution computed tomography and finite element analysis. *Biomed Eng Appl Basis Comm*, 18:214–221, 2006.

[99] C. Lee, L. P. Hsu, P. R. Chen, and C. F. Lee. Computer aided design for three-dimensional visualization and modeling of middle ear biomechanics. *Tzu Chi Med J 2006*, 18(6):416–422, 2006.

[100] Y. Wen, L. P. Hsu, P. R. Chen, and C. F. Lee. Design optimization of cartilage myringoplasty using finite element analysis. *Tzu Chi Med J 2006*, 18(5):370–377, 2006.

[101] T. Koike, H. Wada, and T. Kobayashi. Effect of depth of conical-shaped tympanic membrane on middle-ear sound transmission. *JSME Int Journal. Ser C. Mech Systems, Mach Elem Manuf.*, 44(4):1097–1102, 2001.

[102] T. Koike, M. Shinozaki, S. Murakami, K. Homma, T. Kobayashi, and H. Wada. Effects of individual differences in size and mobility of the middle ear on hearing. *JSME International Journal Series C, Special Issue on Bioengineering*, 48(4):521–528, 2005.

[103] M. Bornitz, H. J. Hardtke, and T. Zahnert. Evaluation of implantable actuators by means of a middle ear simulation model. *Hearing Research*, 263(1-2):145–151, 2010.

[104] X. Zhang and R.Z. Gan. A comprehensive model of human ear for analysis of implantable hearing devices. *IEEE Trans. Biomed. Eng.*, 99, 2011.

[105] Y. Z. Chen and X. Y. Lin. Several numerical solution techniques for nonlinear eardrum-type oscillations. *Journal of Sound and Vibration*, 296:1059–1067, 2006.

[106] E. Alvarado-Anell, M. Sosa, and M. A. Moreles. Numerical simulation of the dynamical properties of the human tympanum. *Revista Mexicana de Fisica*, 54(2):135–140, 2008.

[107] H. M. Ladak and W. R. J. Funnell. On the effect of geometric nonlinearities in a finite element model of the cat eardrum. *IEEE-EMBC and CMBEC Physiological Systems/Modelling and Identification*, 2:1439–1440, 1995.

[108] W. R. J. Funnell. Finite-element modelling of the cat middle ear with elastically suspended malleus and incus. In *Poster presentation at 19th Midwinter Res. Mtg., Assoc. Res. Otolaryngol., St. Petersburg Beach*, 1996.

[109] W. R. J. Funnell, W.F.S. Decraemer, M. von Unge, and J. J. J. Dirckx. Finite-element modelling of the gerbil eardrum and middle ear. *Assoc. Res. Otolaryngol. Abs.*, page 799, 1999.

[110] W. R. J. Funnell. High-frequency time-domain behaviour of a finite-element model of the eardrum. In *24th Midwinter Res. Mtg., Assoc. Res. Otolaryngol., St. Petersburg Beach*, pages –, 2001.

[111] J. P. Fay, S. Puria, and C. R. Steele. The discordant eardrum. In *Proceedings of the National Academy of Sciences (PNAS) of the United States of America*, volume 103, pages 19743–19748, 2006.

[112] H. M. Ladak, W. R. J. Funnell, W. F. Decraemer, and J. J. J. Dirckx. A geometrically nonlinear finite-element model of the cat eardrum. *J. Acoust. Soc. Am.*, 119(5):2859–2868, 2006.

[113] N. Elkhouri, H. Liu, and W. R. J. Funnell. Low-frequency finite-element modeling of the gerbil middle ear. *JARO - Journal of the Association for Research in Otolaryngology*, 7:399–411(13), 2006.

[114] J. P. Tuck-Lee, P. M. Pinsky, C. R. Steele, and S. Puria. Finite element modeling of acousto-mechanical coupling in the cat middle ear. *J. Acoust. Soc. Am.*, 124(1):348–362, 2008.

[115] R. Z. Gan. Three-dimensional finite element modeling of human ear for sound transmission. *US Patent Application Publication*, pages –, 2006.

[116] C. Dai, T.Cheng, M. W. Wood, and R. Z. Gan. Fixation and detachment of superior and anterior malleolar ligaments in human middle ear: Experiment and modeling. *Hearing Research*, 230(1-2):24 – 33, 2007.

[117] X. Wang, T. Cheng, and R.Z. Gan. Finite-element analysis of middle-ear pressure effects on static and dynamic behaviour of human ear. *J.Acoust. Soc Am.*, 122(2):906–917, 2007.

[118] C. Lee, P. Chen, L. Hsu, and C. Lee. Developing an advanced biophysical model for optimal cartilage myringoplasty. *Tzu Chi Med J 2007*, 19(1), 2007.

[119] C. Lee, J. Chen, Y. Chou, L. Hsu, P. Chen, and T. Liu. Optimal graft thickness for different sizes of tympanic membrane perforation in cartilage myringoplasty: A finite element analysis. *Tien-Chen Liu, Laryngoscope*, 117(4):725–30., 2007.

[120] T. H. J. Lesser and K. R. Williams. The tympanic membrane in cross section: a finite element analysis. *The Journal of Laryngology and Otology*, 102:209–214, 1988.

[121] K. R. Williams, A. W. Blayney, and T. H. Lesser. Tympanic membrane damage and repair as analysed by the finite element method. *Transplants and Implants in Otology, Proc. Of the third International Symposium*, III:57–63, 1995.

[122] J.P. Vard, D.J. Kelly, A. W. Blayney, and P. J. Prendergast. The influence of ventilation tube design on the magnitude of stress imposed at the implant/tympanic membrane interface. *Medical Engineering and Physics*, 30(2):154 – 163, 2008.

[123] F. Gentil, R.M. Natal Jorge, A. J. M. Ferreira, M. P. L. Parente, M. Moreira, and E. Almeida. Biomechanical study of middle ear. In *VIII Int. Conf. on Computational Plasticity*, pages 785–788, 2005.

[124] Dillier N. Ferrazzini M, Willi U. Dynamic analysis of the middle ear. In *Abstract and poster, ARO meeting, USA.*, 2002.

[125] J. A. M. Soons, J. Aernouts, and J. J. J. Dirckx. Elasticity modulus of rabbit middle ear ossicles determined by a novel micro-indentation technique. *Hearing Res.*, 263 (2010):33–37, 2010.

[126] R. Z. Gan. Three-dimensional finite element modeling of human ear for sound transmission. *US Patent Application Publication*, 2006.

[127] C. Jones, Q. Sun, and R. Z. Gan. Computer-aided 3-dimensional modelling of human ear. In *Proceedings of the Second Joint EMBS/BMES Conference, Houston*, page 266, 2002.

[128] L.A. Vallejo, V. M. Delgado, A. Hidalgo, E. Gil-Carcedo, L. M. Gil-Carcedo, and F. Montoya. Modelling of the geometry of the external auditory canal by the finite elements method. *Acta Otorrinolaringol Esp*, 57:82–89, 2006.

[129] M. Prasciolu, R. Malureanu, S. Cabrini, D. Cojoc, L. Businaro, A. Carpentiero, R. Kumar, and E. Di Fabrizio. Three-dimensional digital scanner based on micromachined micromirror for the metrological measurement of the human ear canal. *J. Vac. Sci. Technol. B*, 23(6):2990–2994, 2005.

[130] L. Qi, H. Liu, J. Lutfy, W. R. J. Funnell, and S. J. Daniel. A non-linear finite-element model of the newborn ear canal. *J. Acoust. Soc. Am.*, pages 1–27, 2006.

[131] M. Hiipakka. Measurement apparatus and modelling techniques of ear canal acoustics. Master's thesis, Helsinki University of Technology, Department of Signal Processing and Acoustics, 2008.

[132] B. L. Farmer-Fedor and R. D. Rabbitt. Acoustic intensity in the ear canal. incident, reflected and emitted waves. In *Proc. Second Joint EMBS/BMES Conf.*, pages 2151–2152, 2002.

[133] *ANSYS, Inc. Theory Reference.* ANSYS Release 9.0, 2004.

[134] *ANSYS, Fluids Analysis Guide.* ANSYS Release 10.0, 2005.

[135] B. J. Anson and J. A. Donaldson. The surgical anatomy of the temporal bone and ear. *Arch Otolaryngol.*, 87(5):572, 1968.

[136] W. R. Funnell. Low-frequency coupling between eardrum and manubrium in a finite-element model. *J. Acoust. Soc. Am.*, 99(5):3036–43, 1996.

[137] K. R. Williams and T. H. Lesser. A finite element analysis of the natural frequencies of vibration of the human tympanic membrane. part i. *Br. J. Audiol.*, 24(5):319–27, 1990.

[138] P. Ferris. Finite element modeling of the normal and surgically reconstructed human middle-ear. Master's thesis, University of Dublin., 1998.

[139] R.A. M. Celorio, J. J.J.Dirckx, J. A.N. Buytaert, and W. Decraemer L. M. Lopez. Modified temporal-phase-unwrapping method for measuring in real time the out-of-plane displacements of the tympanic membrane of mongolian gerbil. *Optik*, 119:783–787, 2008.

[140] H. Wada, T. Metoki, and T. Kobayashi. Analysis of dynamic behavior of human middle ear using a finite-element method. *J Acoust Soc Am*, 92:3157–66, 1992.

[141] P. J. Prendergast, P. Ferris, H.J. Rice, and A.W. Blayney. Vibro-acoustic modeling of the outer and middle ear using the finite-element method. *Audiol. Neurootol.*, 4:185–91, 1999.

[142] H. J. Beer, M. Bornitz, and J. Drescher. Finite element modeling of the human eardrum and applications. In *In Hüttenbrink K-B, ed. Middle Ear Mechanics in Research and Otosurgery. Proceedings of the International Workshop on Middle Ear Mechanics*, pages 40–7, 1997.

[143] H. Beer, M. Bornitz, H. Hardtke, R. Schmidt, G. Hofmann, and T. Zahnert. Modelling of components of the human middle ear and simulation of their dynamic behaviour. *Audiol. Neuro-Otol.*, 4:158–162, 1999.

[144] T. J. R. Hughes. *The finite element method.* Prentice-Hall, 1987.

[145] K. Homma, Y. Shimizu, N. Kim, Y. Du, and S. Puria. Effects of ear-canal pressurization on middle-ear bone- and air-conduction responses. *Hearing Research*, 263:204–215, 2010.

[146] J. H. Sim and S. Puria. Soft tissue morphometry of the malleus-incus complex from micro-ct imaging. *J. Assoc. Res. Otolaryngol.*, 9:5–21, 2008.

[147] C. F. Chou, J. F. Yu, and C. K. Chen. The natural vibration characteristics of human ossicles. *Chang Gung Med J*, 34(2):160–164, 2011.

[148] F. Gentil, R.N Jorge, A.J.M. Ferreira, P. Parente, M. Martins, and E. Almeida. On the influence of mechanical behavior of the middle ear ligaments: a finite element analysis. *ICCES*, 9(1):45–56, 2009.

[149] W. Yao, J. Ma, and B. Hu. Numerical model on sound-solid coupling in human ear and study on sound pressure of tympanic membrane. *Mathematical Problems in Engineering*, 2011:1–13, 2011.

[150] H. Chen, T. Okumura, S. Emura, and S. Shoumura. Scanning electron microscopic study of the human auditory ossicles. *Ann. Anat.*, 190:53–58, 2008.

[151] C. Weistenhöfer and H. Hudde. Determination of the shape and inertia properties of the human auditory ossicles. *Audiol. Neurootol*, 4:192–196, 1999.

[152] S. Puria and C. Steele. Tympanic-membrane and malleus-incus-complex co-adaptations for high-frequency hearing in mammals. *Hearing Res.*, 263:183–190, 2010.

[153] W.R.J. Funnell, T.H. Siah, M. D. Mckee, S.J. Daniel, and W. F. Decraemer. On the coupling between the incus and the stapes in the cat. *Jaro*, 6:9–18, 2005.

[154] Q. Zhang. Am31 modeling of middle ear ossicles. Master's thesis, Thesis., 2008.

[155] F. Gentil, M. Parente, P. Martins, C. Garbe, R. N. Jorge, A. Ferreira, and J. M. Tavares. The influence of the mechan-

ical behaviour of the middle ear ligaments: a finite element analysis. In *Proc Inst Mech Eng H.*, volume 225(1), pages 68–76, 2011.

[156] R. Z. Gan, X. Zhang, and X. Guan. Modeling analysis of biomechanical changes of middle ear and cochlea in otitis media. In *AIP Conf. Proc.*, volume 1403, pages 539–544, 2011.

[157] B. Feng and R.Z. Gan. A lumped-parameter mechanical model of human ear for sound transmission. In *EMBS/BMES Conference, Proc. Second Joint 1*, pages 267–268, 2002.

[158] R.Z. Gan, F. Yang, X. Zhang, and D. Nakmali. Mechanical properties of stapedial annular ligament. *Med. Eng. Phys.*, 33(3):330–339, 2011.

[159] R. Aibara, J. T. Welsh, S. Puria, and R. L. Goode. Human middle-ear sound transfer function and cochlear input impedance. *Hearing Res.*, 152:100–109, 2001.

[160] S. N. Merchant, M. E. Ravicz, and J. J. Rosowski. Acoustic input impedance of the stapes and cochlea in human temporal bones. *Hearing Res.*, 97:30–45, 1996.

[161] G. Volandri, F. Di Puccio, P. Forte, and C. Carmignani. Biomechanics of the tympanic membrane. *Journal of Biomechanics*, 44(7):1291–36, 2011.

[162] R.L. Goode, M. Killion, K. Nakamura, and S. Nishihara. New knowledge about the function of the human middle ear: Devel-

opment of an improved analog model. *Am. J. Otol.*, 15(2):145–154, 1994.

[163] G. von Bekesy. On the measurement of the amplitude of vibration of the ossicles with a capacitive probe. *Akust. Zeits.*, 6:1–16, 1941.

[164] C. Carmignani, F. Di Puccio, P. Forte, and G. Volandri. Integrazione di metodi fe avanzati per l'analisi fluido-strutturale dell'orecchio. In *Associazione Italiana Analisi Sollecitazioni (AIAS) 2010 National Congress, Maratea*, page 10, 2010.

[165] T. Huttunen, P. Gamallo, and R. J. Astley. Comparison of two wave element methods for the helmholtz problem. *Commun. Numer. Meth. Engng.*, 25:35–52, 2009.

[166] J .F. Doyle. *Wave propagation in Structures*. Springer, 1997.

[167] H. Peng, G. Meng, and F. Li. Modeling of wave propagation in plate structures using three-dimensional spectral element method for damage detection. *Journal of Sound and Vibratio*, 320:942–954, 2009.

[168] P. Gamallo and R. J. Astley. The partition of unity finite element method for short wave acoustic propagation on non-uniform potential flows. *Int. J. Numer. Engng.*, 65:425–444, 2006.

[169] T. Strouboulis, I. Babuska, and K. Copps. The design and analysis of the generalized finite element method. *Comput. Methods Appl. Mech. Engrg*, 181:43–69, 2000.

[170] T. Strouboulis, R. Hidajat, and I. Babuska. The generalized finite element method for helmholtz equation. part ii: Effect of choice of handbook functions, error due to absorbing boundary conditions and its assessment. *Comput. Methods Appl. Mech. Engrg*, 197:364–380, 2008.

[171] O. Laghrouche, P. Bettess, E. Perrey-Debain, and J. Trevelyan. Plane wave basis finite-elements for wave scattering in three dimensions. *Comm. Numer. Methods in Eng.*, 19(9):715–723, 2003.

[172] R. Szilard. *Theories and Applications of Plate Analysis: Classical Numerical and Engineering Methods.* J. Wiley and Sons, Inc., 2004.

[173] G. Volandri, C. Carmignani, F. Di Puccio, and P.Forte. Comparison of fe models for the tympanic membrane. In *poster session, 17th Congress of European Society of Biomechanics, ESB 2010*, 2010.

[174] G. Volandri, F. Di Puccio, P. Forte, and S. Manetti. Model-oriented review and multi-body simulation of the ossicular chain of the human middle ear. *Med Eng Phys (submitted, accepted)*, 2012.

[175] A. Eiber, A.M. Huber, M. Lauxmann, M. Chatzimichalis, D. Sequeira, and J.H. Sim. Contribution of complex stapes motion to cochlea activation. *Hearing Research*, pages 1–11, 2011.

[176] D. E. Finkel. *DIRECT Optimization Algorithm User Guide*, pages 1–14. http://www4.ncsu.edu/∼ctk/Finkel Direct/, 2003.

[177] W. F. Decraemer, O. de La Rochefoucauld, and E. S. Olson. Measurement of the threedimensional vibration motion of the ossicular chain in the living gerbil. In *AIP Conf. Proc. 1403*, pages 528–533, 2011.

[178] A. Huber, T. Koike, H. Wada, V. Nandapalan, and U. Fisch. Fixation of the anterior mallear ligament: diagnosis and consequences for hearing results in stapes surgery. *Ann. Otol. Rhinol. Laryngol.*, 112(4):348–355, 2003.

[179] S. Ihrle, M. Lauxmann, A. Eiber, and P. Eberhard. Nonlinear modelling of the middle ear as an elastic multibody system - applying model order reduction to acousto-structural coupled systems. In *Fifth International Conference on Advanced COmputational Methods in ENgineering (ACOMEN 2011), Liège, Belgium*, page 10, 2011.

[180] Forte P. Manetti S. Volandri G., Di Puccio F. Modellazione multi-body dell'orecchio umano. In *Proceedings of AIMETA 2011*, page 10, 2011.

[181] M. R. Hatch. *Vibration simulation using Matlab and Ansys.* Chapman and Hall/CRC, 2000.

[182] H. Fastl E. Zwicker. *Psychoacoustics: Facts and Models.* Springer, 2007.

[183] E. Zwicker. Procedure for calculating loudness of temporally variable sounds. *J. Acoust. Soc. Am.*, 62(3):675–682, 1977.

[184] A Sirkka A. Nykanen. Specification of component sound quality applied to automobile power windows. *Applied Acoustics*, 70(6):813–820, 2009.

[185] T. C. Lim. Correlations between deficiencies in power window systems influencing sound quality and some psychoacoustic metrics. *Applied Acoustics*, 62(9):1025–1047, 2001.

[186] G. Von Bismarck. Sharpness as an attribute of the timbre of steady state sounds. *Acustica*, 30:159–172, 1974.

[187] W. Aures. Procedure for calculating the sensory euphony of arbitrary sound signals. *Acustica*, 59:130–141, 1988.

[188] W. Aures. Ein berechnungsverfahren der rauhigkeit (a procedure for calculating auditory roughness). *Acustica*, 58:268–281, 1985.

[189] A. Nykänen. Methods for product sound design. Master's thesis, Luleå University of Technology, Department of Human Work Sciences, Division of Sound and Vibration, 2008.

[190] J. N. Penfold. Power window sound quality - a case study. *Noise and Vibration*, SAE Technical Paper Number: 972017, 1997.